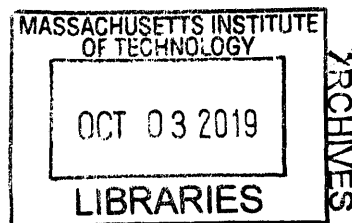# Confinement Effects on Multiexciton Dynamics in Semiconductor Nanocrystals

by

Katherine E. Shulenberger

B. A. Chemistry
Wellesley College, 2014

Submitted to the Department of Chemistry
in partial fulfillment of the requirements for the degree of
Doctor of Philosophy

at the

MASSACHUSETTS INSTITUTE OF TECHNOLOGY

September 2019

Signature redacted

Author ....
Department of Chemistry
August 14, 2019

Signature redacted

Certified by ....
Moungi G. Bawendi
Lester Wolfe Professor of Chemistry
Thesis Supervisor

Signature redacted

Accepted by ....
Robert W. Field
Haslam and Dewey Professor of Chemistry
Chairman, Department Committee on Graduate Students

This doctoral thesis has been examined by a Committee of the

Department of Chemistry as follows:

Signature redacted

Professor Gabriela Schlau-Cohen ....

Chairman, Thesis Committee

Assistant Professor of Chemistry

Signature redacted

Professor Moungi G. Bawendi ....

Thesis Supervisor

Lester Wolfe Professor of Chemistry

Signature redacted

Professor William A. Tisdale ....

Member, Thesis Committee

ARCO Career Development Professor of Chemical Engineering

3

Confinement Effects on Multiexciton Dynamics in Semiconductor Nanocrystals

by

Katherine E. Shulenberger

Submitted to the Department of Chemistry
on August 14, 2019, in partial fulfillment of the
requirements for the degree of
Doctor of Philosophy in Chemistry

Abstract

Colloidal semiconductor nanocrystals are a promising platform for a number of technological developments in a wide variety of lighting applications. They also are an incredibly useful model system to interrogate fundamental carrier interactions in crystalline semiconductor lattices. This thesis investigates the properties of multiexciton states in semiconductor nanocrystals to build an understanding of what drives their emission dynamics and efficiency. A complete understanding of the processes which dominate in a wide variety of nanocrystal systems sheds light on electron-hole and exciton-exciton interactions and provides guidance on how to engineer nanocrystals for particular applications.

In the first two chapters, I will build a foundation of understanding of semiconductor nanocrystal systems, and how to build up an intuitive understanding of the states in question from both fundamental modeling and chemical intuition. I also present a variety of methods which are used to interrogate the luminescent properties of these materials, with a particular focus on those utilized in this thesis. In the second chapter in particular, I focus on how photoluminescence measurements can go astray, how to identify artifacts or background signal which could bias or invalidate data, and how to eliminate these artifacts.

The next chapter details the biexciton and triexciton emission dynamics and efficiency in CdSe nanocrystals. Utilizing a well-established and well-studied semiconductor systems allows nuanced interpretation of the emission dynamics, and the identification of perhaps some unexpected material properties to enhance how we imagine these highly excited states.

Chapter four employs a suite of methods to begin to understand carrier-carrier interactions in cesium lead halide perovskite nanocrystals. This system provides a particularly interesting platform to investigate the effect of confinement and lattice mobility on excitonic properties.

Finally, I present a few experimental directions and ideas which have not yet been explored and would provide an excellent continuation of this work.

Thesis Supervisor: Moungi G. Bawendi
Title: Lester Wolfe Professor of Chemistry

1 Acknowledgements

Looking back, it is truly a monumental task to try to thank all the individuals who have provided the opportunities, encouragement, and support that have brought me to this point in my life. Nonetheless, the following represents my best effort to put into words my gratitude for everyone who has been a part of my journey:

First, I want to thank my advisor Moungi Bawendi. I cannot describe just how much I have learned and grown through being a member of the Bawendi Group. Thank you Moungi for always encouraging me to follow the projects that excited me, teaching me the importance of careful rigorous experimentation, and providing me with the opportunities to improve myself as a scientist, a mentor, a teacher, and a person.

I also would like to thank Will Tisdale. Words are insufficient to express how crucial being a part of the Tisdale group has been for my graduate work. Will, thank you so very much for welcoming me into your group, being a second advisor and mentor to me, and encouraging and fostering some of the most productive and exciting collaborations of my graduate career.

I would like to thank my thesis chair, Gabriela Schlau-Cohen for being an incredible resource both for my personal and career development, as well as always being willing to discuss technical details as I built my microscope, and designed analysis software. I have also been incredibly fortunate to have had a series of truly excellent mentors and advisors throughout my entire academic career who have fostered my love of science and math and always encouraged me to pursue what I love: Chris Arumainayagam, Mala Radhakrishnan, Nolan Flynn, Carla Verschoor, Karen Atkinson, Ms. Eaton, Mr. Edun, Mr. Changaris, and Mrs. Miles. In particular, thank you to Professor A., who saw in a first-semester, first-year college student something and taught that baby academic to be a scientist, ask questions, find ways to answer them, that math really can explain the universe, and that is the most beautiful truth in this universe. We may now disagree what the most beautiful and important equation is, but I still look up to and aspire to be the kind of mentor you are one day. Thank you.

It is important to have not only supervisors and mentors who inspire you, but colleagues and collaborators too. In this, I have also been incredibly lucky. I know that through working with others my own projects have become more than they ever could have been had I been going it along. To Hendrik Utzat, we started this crazy journey as first years with a blank slate, full of ideas and dreams. Through it all you have been an incredible scientific partner, and I appreciate how much you have pushed me to be excellent. To Matt Ashner, I can only say that you inspired me when I was stuck and saw no direction to finding answers. We may never have satisfactorily answered that original question, but along the way we answered questions I didn't even know were there. Having someone to verbally process with was crucial, but I also am so thankful for your friendship day in and day out. To Nathan Klein, I may have adopted you as a mentee, but you quickly became so much more. Between enabling the project I had been dreaming of for literal years, helping me solve complex sets of differential equations over coffee, and just listening and believing me no matter what, your influence rings through the following pages more than you may

ever fully know. To Sophie Coppieters 't Wallant, you are the most driven and brilliant student I could have hoped to work with. I may have thrown the book of solid state physics at you on day one, but you took it all in stride and taught me so much about being a mentor. The triexciton project is as much yours as it is mine. I know you will do big things in this world, and that is the greatest reward I could imagine. To Thomas Bischof, thank you for teaching me everything about optics, photon counting, and multiexcitons. You are truly a fabulous mentor. To Lea Nienhaus, you showed me the kind of scientist I aspire to be. Thank you for your continued support. To Maksym Kovalenko, Franziska Krieg, and all my other collaborators, thank you for helping me find answers. I couldn't have done it without you. To the spectroscopy subgroup, thank you for the thoughtful and productive discussions. To the Tisdale lab, thank you for being the best coworkers. Between coffee hour, crossword puzzles, volleyball, and Jamborees you have made work fun.

I started my doctoral work with a whole cohort of crazy, nerdy hooligans. Everyone said we wouldn't be friends beyond that first semester, and I am so so glad that they were wrong. Sam, Dan, Brian, Nathan, Helena, Alex, and Jay, it's been a wild ride and I am so glad we took it together. I know that the bonds forged in the grad lounge are forever, no matter where we live. Thank you for the adventures and the laughs. Nicole, you may have started as the "favorite first-year," but I am so thankful that you became one of the group and for your friendship every day. Julia, I didn't know I needed a friend like you in my life until you appeared, and now I can't imagine it any other way.

In my time on MIT campus, I have developed strong ties to so many other groups and individuals that I could in no way begin to name them all, so I just want to thank my EAB, GSC, and Thirsty Ear families. You have enriched my life beyond my wildest dreams. I couldn't have done this without you. I also have had the most amazing support from a number of MIT offices which I cannot imagine having made it here without. Thank you to the Chemistry Education office, in particular Jennifer Weisman; the VPR team, in particular Meg Chuhran; the OGE, in particular Suraiya Baluch; and Tessa McClain.

Outside of MIT, I have found the most amazing family at Wolf Creek Stables. I came looking for an athletic outlet for academic stress and you gave me a family. Thank you to Brianna and Brandi for being amazing partners this summer and sharing Merlin. You have brought me so many smiles and laughs. Thank you to Eugene for being my barn partner. It's been a lot of hours (many in a car), and I treasure that time and your friendship. Kellie, you taught me to fly and I will always be grateful for my wings. There are far too many more to mention by name, but I love you all and am proud to be a part of the Wolf Pack.

It takes something very special to be willing to live with someone working towards a PhD. I have been very lucky in my roommates these past five years. Thank you Troy, Patrick, Rachel, Rose, Munchkin, Dan, Brian, and Alex for making my home a home through all the stress and craziness. To Mollie and Emily, we may not have lived at the same address since college, but Roomies are for life. #Triple. Thank you so much for being more like family than I could have imagined and for sticking by me through everything. Alex, you may never have lived with me officially, but thank you to my honorary roommate. Your practicality and sense of humor have lit up some of my darkest days. Brian, you are so much more than a roommate or yearmate. From

Pancake Sunday to adventures atop mountains in Alaska, you have been an incredible source of support. Thank you for being my partner.

To my Mom and Dad, you have been with me every step of the way. From late night childhood science experiments to late night phone calls walking home I have always felt supported and encouraged. Thank you for believing in me and in my dreams and paving the roads for those dreams no matter where they led. Everything I am is because of you.

Finally, to Munchkin, my other half, my "little" sister. I knew the first time I laid eyes on you that you were the most important person in my world. I always knew you would grow into a woman I could look up to (both literally and figuratively), but I am still wowed by you every day. No matter the distance, I always know I can count on you and that has meant more than I can say. I cannot wait for all our adventures to come. Thank you.

Contents

List of Figures

11

List of Tables

13

2 Introduction

This thesis details the photophysical properties of colloidal semiconductor nanocrystals, also known as quantum dots, under device relevant conditions for lighting and lasing applications. Semiconductor nanocrystals (NCs) are technologically interesting fluorophores for these applications due to a number of reasons. First, they are colloidally stable, and therefore solution processable, allowing for integration into devices through spin coating,[1,2] dropcasting,[3,4] or ink-jet printing[5-7] and are therefore compatible with flexible substrates. Next, due to quantum confinement of the exciton – a bound, correlated electron-hole pair – semiconductor NCs have tunable bandgaps simply by changing the NC size.[8,9] Furthermore, in part due to highly optimized syntheses, many semiconductor NCs have narrow emission linewidths with negligible heterogeneous broadening.[10,11] Finally, highly developed semiconductor NC systems, such as CdSe, regularly have unity or nearly unity exciton quantum yield.[10,12-14] That is to say, for every excitation created one photon is emitted. There is a small caveat here, however; while the single exciton state has unity quantum yield, NCs may sustain more than one excitation simultaneously and these multiexciton states have drastically lower emission efficiencies.[15,16] Nonradiative recombination from multiexciton states may currently act as an energy loss mechanism, but the presence of these states also provides an opportunity to overcome lifetime-limited fluorescence saturation, a major drawback to the use of molecular dyes for high-flux emission applications.[17-19] Thus, a thorough understanding of multiexciton states, the driving forces between radiative and nonradiative processes, and how to control them is crucial in the optimization and continued commercialization of semiconductor nanocrystals. The following chapters set forth to establish the current understanding of these multiexcitonic states, the methods that exist to interrogate them,

and my work expanding both our methodology and understanding of multiexcitons in nanocrystalline semiconductor lattices.

2.1 Semiconductors

In order to fully understand the dynamic processes dominating NC systems, I begin by considering the energetic bands which determine the properties of bulk semiconductor materials. While nanocrystals exhibit properties that fall between those of molecular systems and bulk semiconductor materials, it is a cleaner mental exercise to discretize the bulk systems, rather than expand the discrete molecular picture to many thousand atoms.

There are many excellent works which detail how to calculate the band structure of a bulk semiconductor through a myriad of methods, each with specific strengths and drawbacks.[20] For a qualitative understanding of band edge states, simple linear combination of atomic orbitals (LCAO) approximations can be quite illuminating. Perspectives gained from LCAO theory, or in the semiconductor world, tight-binding models, provide an excellent first approximation of semiconductor properties. Determining the atomic orbitals which dominate the behavior of the valence band maximum and conduction band minimum provide key insights into the angular momentum and degeneracy of those states.

In order to calculate full band structures, the results of k·p theory describe the energy states observed in bulk and nanocrystalline semiconductors quite well. k·p theory is a perturbation method where the Hamiltonian can be written in the form shown in equation (2-1).

$$H = \frac{p^2}{2m} + V + \frac{\hbar^2 k^2}{2m} + \frac{\hbar \boldsymbol{k} \cdot \boldsymbol{p}}{m} \tag{2-1}$$

The Hamiltonian can be separated into the first two terms to form the unperturbed Hamiltonian, and the second two terms which are the perturbed Hamiltonian. The method gets its name for the dot product of the reciprocal space and momentum operators present in the fourth term above and is particularly adept at calculating electron and hole effective masses at and around the gamma point. This is because the smaller k, the more accurate the perturbation method is because the contribution from the perturbed Hamiltonian decreases.

As I have alluded to already, these energy states are not discrete states with well-defined energy and momenta but a continuous surface of energy states represented in reciprocal space. That is to say a given state can have a range of energy and momentum properties depending on the position within the lattice.

At room temperature, it is most accurate to discuss the properties of electrons and holes as quasi-independent in most bulk semiconductors. However, there is an attractive Coulomb interaction between the positively-charged hole and negatively-charged electron which results in a binding energy.[21] Generally, this binding energy is sufficiently small compared to thermal energy that entropic driving forces result in the dissociation of electrons and holes. However, at low temperatures or in semiconductors with unusually high binding energies it is possible that the electron and hole remain energetically bound. This bound state is referred to as an exciton.

2.2 Semiconductor Nanocrystals

The picture outlined above changes slightly when moving to nanostructured materials. These nanomaterials can come in many different morphologies such as nanospheres,[8] nanocubes,[9] nanoplatelets,[22] nanorods,[23] and exotic shapes such as tetrapods.[24] Materials can be further modified by combining multiple semiconductors such as core-shell nanocrystals,[25] dot-in-rod heterostructures,[12] Janus particles,[26] as well as core-shell[27] and core-crown[28] nanoplatelets.

Starting with the core-only materials, the band structure changes drastically based on the finite size of the nanocrystal. One way to consider this is that the bands discussed in the bulk case are actually just the infinite possible linear combinations of atomic orbitals that can be formed with the quasi-infinite number of atoms in a bulk crystal. Each of these states is so close in energy to the next, they can be accurately depicted as a continuum of states. When moving to a nanoscopic system, rather than the infinite number of atoms we consider in the bulk phase, there are a finite number (tens to thousands) of atoms. The finite nature of the atomic composition results in a discretization of the band structure, particularly around the band-edge. We may still consider these states using the same atomic orbital compositional arguments which are used in the bulk-case to describe the angular momentum character and degeneracy, but these states now have finite occupancy. Furthermore, due to both the energetic and spatial confinement, the excited state is strongly excitonic, resulting in an increased absorption resonance near the band-edge and correlated electron-hole angular momenta. Since the electron and hole remain spatially correlated, the emission efficiency of semiconductors also increases drastically due to constant and high wavefunction overlap. In order to fully understand multiexciton dynamics within this energy landscape, we first must have a thorough understanding of the exciton state to use as a basis for comparison.

2.2.1 Exciton Dynamics

In a perfect world, a nanocrystal will emit at a constant intensity that is determined by the radiative rate of the emissive state and absorption probability at a given excitation fluence.[29] In the real world, even individual emissive processes are limited by shot noise, or uncorrelated random events. Thus, emission from a single radiative state does not have a single intensity over time, but rather a distribution of intensities. These intensities fit to a Poisson distribution centered around a given average, which can be determined from the absorption cross section and excitation fluence.

17

The dynamics of a single radiative state will be a purely monoexponential decay with a rate equivalent to the intrinsic radiative rate of the given state.[30] Intensity trajectories are rarely comprised of emission from a single shot noise limited state though, and a number of competing processes must be taken into account.

Almost all nanocrystal systems demonstrate fluorescence intermittency, or blinking, behavior on millisecond to minute time scales, depending on the exact nanocrystal sample.[31–34] This intermittency is due to changes in nanocrystal structure, ligand coverage, and charge state which leads to transient trap states as well as fluctuating trion (either a positively or negatively charged state) formation.[31,33] Trion states are generally emissive, with a lower quantum yield than the neutral exciton due to the availability of nonradiative Auger recombination.[35–37] An Auger process is the recombination of an electron with a single hole and rather than emitting the affiliated energy as a photon, promoting a third carrier (either an electron or hole) into a state deep in the conduction or valence band. That carrier then rapidly cools through phonon emission back to the band edge, resulting in the relaxation of an exciton without emitting a photon. It is highly likely that the positive and negative trion states will have different quantum yields due to differential Auger rates for each.[36] Trion states are generally identifiable by their intermediate emission intensity which corresponds to a drastically quenched fluorescence lifetime.[31] If the pure trion state can be isolated, it should still emit with monoexponential decay kinetics with a faster lifetime.[36]

Trap states often exhibit two distinct types of behavior dependent on their energy level and accessibility: those accessible from the band-edge, and those only accessible during hot carrier cooling.[33] Trap states that are thermally accessible from the band edge will manifest as a changing emission intensity and lifetime. Depending on the energy and density of trap states, the effect on the lifetime will be variable. Traps that are only accessible during hot carrier cooling will result in

a decreased emission intensity, but no change to the emission dynamics. There are a number of thorough reviews of nanocrystal blinking behavior which detail the differences in these processes. In particular, Yuan, *et al.*,[31] describes single nanocrystal blinking quite well, highlighting the difference between individual nanocrystals in a fairly homogeneous ensemble.

Almost all deviations from monoexponential behavior in ensemble fluorescence lifetimes can be attributed to either nanocrystal heterogeneity, transient charging, or trapping.[29,31] Ensemble heterogeneity will manifest as multiexponential or stretched exponential behavior with many radiative rates which are all similar in time constant, and usually in some form of continuous distribution.[38,39] Pure charging will manifest as a biexponential decay with one exponential component corresponding to excitonic recombination, and one component corresponding to the radiative and nonradiative rate for the trion state.[36] Trapping is more likely to have strong multiexponential character, but unlike with ensemble heterogeneity, it will usually manifest as a rapid early time component characteristic of the trapping rate, and then longer time dominated by the intrinsic exciton lifetime.[31] It is of course also possible to have contributions from any of these in combination.

It can be a challenge to isolate exciton behavior from that of trapping and charging processes even in a single NC measurement which eliminates heterogeneity. The most basic method to do so involves examining a histogram of fluorescence intermittency and selecting a cut-off intensity which separates the high-intensity, excitonic state from other lower efficiency states.[29] This method is commonly referred to as thresholding and has the advantage of being straightforward. However, it has been demonstrated that the selection of an 'on' state threshold imposes a significant amount of user bias, particularly in rapidly fluctuating or complex intensity

trajectories. Change point algorithms are one of the main alternative methods to analyze this intermittency.[40] These methods are discussed in detail in Chapter 3.

The next crucial component in understanding exciton dynamics, once charging and trapping contributions have been identified, is a thorough picture of the exciton fine structure. Fine structure is discussed in detail in Chapter 4. When considering exciton dynamics the major contributions from nanocrystal fine structure are the total angular momentum of each state, which determines whether a state is emissive (bright) or non-emissive (dark), and the energy splitting between these states.

2.2.2 Biexciton Dynamics

Once a complete understanding of exciton dynamics has been established, multicarrier processes must then be considered. When studying a biexciton or higher excited state, not only are charge and trap states influencing the quantum yield and dynamics of the material, but multicarrier non-radiative processes are as well.[15,41–45] Auger recombination is believed to be the dominant mechanism which results in multiexciton quantum yields which are less than the exciton quantum yield of a system, in addition being the mechanism for the reduced quantum yield of trion states discussed earlier.[36] The Auger rate is determined by the electron hole wavefunction overlap and the density of final states available to the promoted carrier.[46] The Auger rate in CdSe and CdSe/CdS nanocrystals have been extensively studied and for core-only materials almost universally scales with the volume of the NC.[47] There have been a few more recent exceptions to this universal volume scaling of Auger rates, such as in 2-D nanoplatelets.[48]

If Auger rates dominate the nonradiative processes for multiexciton states, then the next crucial quantity to determine is the radiative rate. For any given state, the two most important factors in determining the radiative rate are the energy of the transition and wavefunction overlap. For the energy of the transition, from a first glance it should be the same as the energy of the

exciton. At minimum the band-edge of all semiconductor NCs have a degeneracy of two. Therefore, the biexciton occupies the same state and ignoring exciton-exciton interaction, will have the same energy. The difference between the energy of two isolated excitons and a biexciton is termed the biexciton binding energy.[16] The first order consideration of the biexciton binding energy would be the Coulomb interaction between the four carriers. The electron-hole interactions should directly cancel with the electron-electron and hole-hole interactions and thus there should be no expected binding energy. Taking higher-order Coulomb and Exchange interactions into account results in a small biexciton binding energy.[49,50] In most core-only materials studied thus far, binding energies are on the order of a few meV and attractive in sign.[51] Extensive heterostructure engineering has succeeded in creating CdSe/CdS NCs with large repulsive biexciton interactions through carrier separation, demonstrating there is no guarantee that a biexciton interaction must be attractive.[52]

The next consideration is the wavefunction overlap, but since the exciton and biexciton must occupy the same states, there is unlikely to be much difference in the overlap, and therefore the radiative biexciton rate should not be appreciably different from the exciton, ignoring fine-structure considerations. The fine-structure of a given state will determine the multiplicity of recombination pathways, and thus the scaling of the biexciton rate as compared to the exciton. This scaling is discussed extensively in Chapters 4 and 5.

Due to the complex nature of multiexciton emission processes, it is crucial to have nuanced methods to interrogate these dynamic processes. The following sections describe the methods utilized in this thesis.

2.3 Methods

This section details all the spectroscopic methods used throughout this work. The majority of data are collected through a variety of fluorescence techniques, but some absorption methods are also utilized. Fluorescence techniques include single nanocrystal confocal methods, ensemble-averaged single molecule methods, and wavelength dependent ensemble methods. The combination of these allows the nuanced interrogation of exciton and multiexciton dynamics towards the goal of understanding the dominant states and processes relevant for high-flux nanocrystal applications.

2.3.1   Ensemble Methods

2.3.1.1   Ensemble Photoluminescence Lifetime

The lifetime of any fluorescent sample is the decay curve of the emission process. When a sample is excited using a pulsed laser source, the entire fluorescent population is created simultaneously. By monitoring the delay between the laser excitation pulse and the detection of an emitted photon, then taking a histogram of the delay times, a fluorescence decay curve can be constructed. This method is generally referred to as Time-Correlated Single Photon Counting (TCSPC).

2.3.1.2   Spectrally Resolved Photoluminescence Lifetime

There are two methods used in this thesis to spectrally resolve the photoluminescence lifetime. The first utilizes the same photon counting detector as a traditional PL lifetime measurement, but the detector is placed at the output of a monochromator. By sweeping the center wavelength across the fluorescence spectrum the lifetime can be measured at each spectral position. In a truly homogeneous sample that is emitting exclusively from a single state the lifetime at each spectral position will be identical. However, if a photoluminescence decay contains emission from multiple states or sample subpopulations, the dynamics will vary as a function of wavelength.

The other method used in this thesis to measure wavelength-dependent dynamics is a streak camera. In this case, rather than scanning a monochromator and only selecting one wavelength at a time, the spectrum is dispersed by a spectrograph. Then the collected light is converted to electrons by a photocathode and passes through a streak unit, which sweeps an increasing voltage as a function of time after laser excitation. The stronger the voltage, the more distance the detected signal is translated at any given time. Thus a streak camera spatially separates emission based on the time after excitation. The two-dimensional data (time and wavelength) is then imaged using a traditional CCD camera, producing a wavelength-dependent lifetime. One major advantage of a streak camera is that the time resolution is limited by the rate at which the voltage can be swept, and thus much higher temporal resolution can be achieved, unlike single-photon detectors. On the other hand, the lower sensitivity of CCD cameras results in this method only being applicable for fairly concentrated and highly emissive samples, whereas the single photon sensitivity of APDs allows for the detection of signal from an individual NC.

2.3.1.3   Transient Absorption Spectroscopy

In addition to the photoluminescence methods described above, this thesis also contains results from transient absorption (TA) spectroscopy. In brief, transient absorption is an ultrafast absorption method which can be used to interrogate the dynamics of occupied states after excitation, providing complementary information to photoluminescence results. PL can only interrogate states which couple to the rate of photon emission within a kinetic model. TA is an ultrafast pump-probe technique. First, a femtosecond pulse of monochromatic light is focused onto the sample. Usually this pump source is chosen to be well above the band edge. In this thesis a 400 nm pump source was used to excite the NC samples. After some delay, a broad-band probe pulse is also focused onto the sample. The absorption of the probe pulse is measured with and without the pump pulse through the use of a mechanical chopper, and the transmitted probe light is imaged

through a monochromator onto a CCD camera. The time delay between the pump and probe pulse is then varied through a stage delay which can scan up to ~3 ns for the instrument used in this work.

2.3.2 Single Particle Methods

This thesis utilizes a large distribution of methods to analyze the dynamics and properties of light emitted from a single nanocrystal. All these methods are predicated on the same experimental setup, and also provide the dominant body of work for this thesis.

The microscope is a home-built single particle fluorescence instrument. There are a number of available excitation sources, all of which are fiber coupled into the microscope. Most data are collected using either a 405 nm or 532 nm pulsed diode laser as an excitation source. The excitation beam is directed through a series of neutral density filters which are used to control the incident laser power, then directed off a dichroic mirror into a microscope objective. For single-particle experiments an oil immersion objective is used, and for solution phase correlation measurements a water immersion objective is used. The microscope objective is mounted to a motorized unidirectional stage which can be used to bring the sample into focus. The sample is mounted to a three-axis piezo stage with sub-nanometer precision in x, y, and z. The z dimension is used to optimize the microscope focus, and the x and y directions are used to perform raster scans across the sample. Emission from a nanocrystal in the focal volume is collected by the same objective and separated from the excitation source using a dichroic mirror (either 425 nm long pass or 535 nm long pass). Emission is further filtered using a 1:1 telescoping pinhole (10 cm focal length
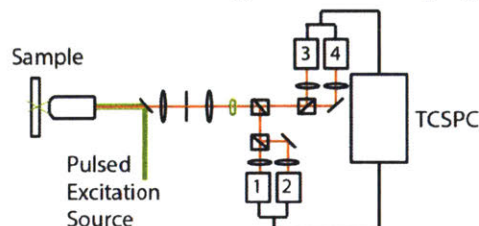
Figure 2-1 Illustration of the home-built fluorescence microscope used for single molecule studies in this thesis.
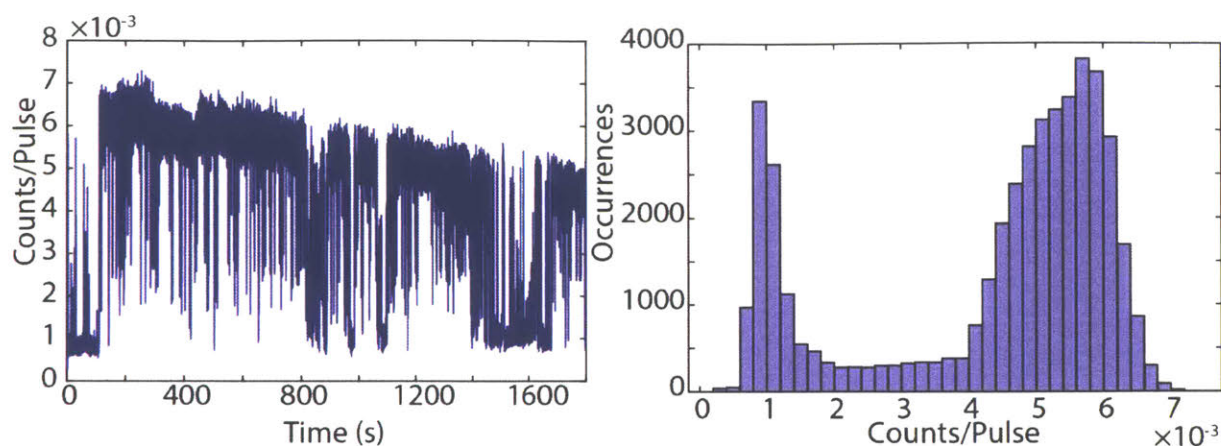
Figure 2-2 A fluorescence intensity trace with 40 ms time bins and the histogram of the intensity states. The low intensity state is shot noise limited. The high intensity state is not, predominantly due to microscope drift throughout the experiment.

achromat lenses, 50 µm pinhole) and additional emission filters (425 nm long pass or 532 nm notch). After filtering, the emission is split into four equivalent beams using three 50:50 beam splitters in the geometry shown in Figure 2-1. Each of the four beams is then focused onto a single photon counting detector using a 10 cm focal length lens. The turning mirrors in the detection component of the microscope are all cold mirrors (reflect ≤ 700 nm and transmit ≥700 nm) to suppress detector crosstalk (discussed further in Chapter 3). Detection events are recorded using a HydraHarp 400 in t3 mode. These records note the pulse number after which a photon arrived, the time after the laser pulse, and the detector number at which it arrived for each photon. This record of photon arrival times will henceforth be referred to as the photon stream, and is the basis for the following single molecule analyses. In total the fluorescence setup described here is optimized for high detection efficiency, collecting roughly 15% of emitted photons in the green, with efficiencies peaking in the 600-700 nm range based on the efficiency of the detectors in that wavelength range. No photon detection can occur above 700 nm without further modifications due to the cold mirrors utilized in the detection component of the microscope. In order to reduce background counts, the entire microscope is enclosed in a homebuilt blackout box, and detectors are fitted with lens tubes

which eliminate almost all stray light. The following describe different analysis methods that can be applied to the photon stream after data collection.

2.3.2.1 Intensity Trace

An intensity trace may be generated from the photon stream by selecting a time window (say 5 ms), counting how many photons arrive in each 5 ms bin, and plotting these as a function of time. If a sample is constantly in a single emissive state, the spread of intensity values will be shot noise-limited and follow a Poisson distribution. There may be multiple discrete states which are shot noise-limited, or many many quasi-continuous states which do not fit any one distribution well. These distributions may be examined by taking a histogram of the intensity states as demonstrated in Figure 2-2.

2.3.2.2 Lifetime

The fluorescence lifetime of a sample is the histogram of delay times between an impulsive excitation event, and the detection of an emitted photon. The method is identical in theory to the ensemble lifetime described above, but instead of measuring the average behavior across many different nanocrystals, it measures the emission from an individual NC.

2.3.2.3 Biexciton Quantum Yield

This second order correlation method which can be used to extract the quantum yield of the biexciton state was derived in great detail by Nair et al.[53] Rather than walking through the detailed mathematical justification for the method, which can be found in the supplemental information of Nair et al.,[53] Figure 2-3 presents a qualitative understanding of why the center to side peak ratio measures the biexciton to exciton quantum yield ratio. The side peak represents events where a single photon was absorbed and emitted on two successive pulses. The center peak represents when two photons are absorbed and emitted after a single laser pulse. Due to the Poissonian absorption statistics of nanocrystals, the two absorption events described for the center

and side peak have equivalent probabilities. Thus, the ratio between the two peak areas is the ratio of quantum yields.

There are a few key conditions that must be met for the following explanation to hold though. First, the nanocrystal must be absorbing in the low flux regime. That is to say, it must be statistically likely that when one photon is detected, it originated as a single exciton. Similarly, when two photons are detected, they likely originated as a biexciton, etc. A good benchmark for the low flux criteria is <0.01 excitations per pulse. Next, the second photon of a biexciton must be exactly the same as an independently excited, single exciton. If the second photon of a biexciton does not have the same quantum yield as a single exciton, then some of the terms in the derivation do not appropriately cancel. Finally, the Poissonian absorption statistics that have been described for NC systems must hold, otherwise the absorption probabilities for the center and side peak scenarios will vary.

Assuming all these conditions are met, the center to side peak ratio then reduces to

$$\frac{A_{center}}{A_{side}} = \frac{QY_{BX}QY_X}{QY_XQY_X} \qquad (2\text{-}2)$$
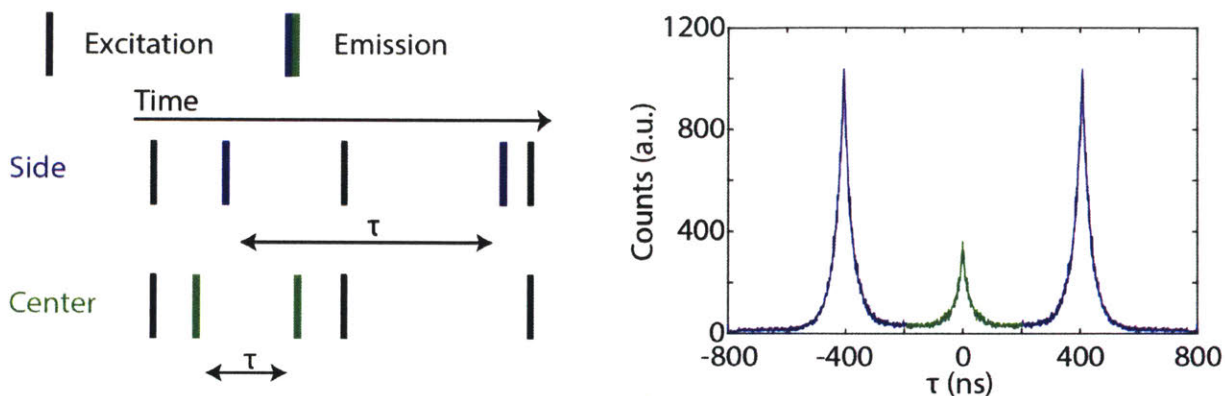
Figure 2-3 Schematic of the second-order correlation measurement where the center peak (green) corresponds to two photons detected after the same laser pulse, and the side peak (blue) corresponds to two photons detected on subsequent laser pulses.

Where A_{center} and A_{side} are the center and side peak areas respectively and QY_{BX} and QY_X are the biexciton and exciton quantum yields respectively. The numerator then corresponds to the quantum yield of the first and second photon of a biexciton, and the denominator corresponds to the quantum yield of two single excitons. Thus, the expression reduces to simply the biexciton to exciton quantum yield ratio. In the case where the exciton has 100% quantum yield, the center to side peak ratio is exactly the biexciton quantum yield.

2.3.2.4   Biexciton Lifetime

The biexciton lifetime can be extracted through low-flux, single-particle photon number counting methods as described by Shulenberger *et al.* By selecting only for pulses where two photons were detected after a single excitation pulse, the first detected photon then corresponds to
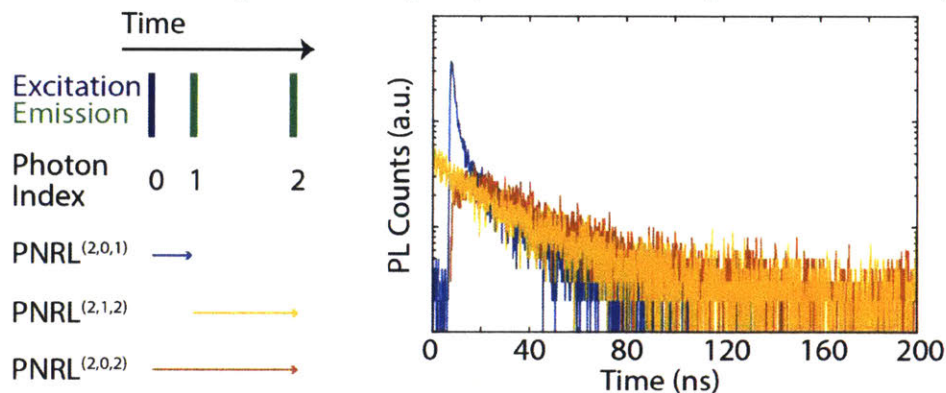
Figure 2-4 Illustration of the various lifetimes extracted from two photons events and the notation used to describe these time delays.

28

emission from the biexciton state, and the second detected photon corresponds to emission from the residual exciton left behind after biexciton recombination. The biexciton lifetime is the histogram of time delays between the excitation pulse and the arrival of the first photon. The lifetime of the residual exciton is the histogram of time delays between the arrival of the first photon and second photon. Shulenberger et al.[54] describe these photon number resolved lifetimes (PNRLs) using the notation $\text{PNRL}^{(2,0,1)}$ and $\text{PNRL}^{(2,1,2)}$ respectively, where the superscript notation corresponds to the number of photons detected, the start index, and the stop index, as illustrated in Figure 2-4. There is a third lifetime which can be calculated from two photon detection events, $\text{PNRL}^{(2,0,2)}$, or the delay between the excitation pulse and the detection of the second photon. These data contain information about both the biexciton and residual exciton lifetime together and are therefore generally not used.

2.3.2.5 Triexciton Quantum Yield

The triexciton quantum yield of a single particle is derived in the supplemental information of Shulenberger et al.[54] Following in the methodology established by Nair et al.,[53] the emission probability of three photons detected after a single excitation pulse is the product of the triexciton, biexciton, and exciton quantum yields. The equivalent to the two-photon side peak in the three photon experiment is two photons detected after a single laser pulse, with an emission efficiency that is the product of the biexciton and exciton quantum yields, and a single photon on the subsequent pulse with an emission efficiency of the single exciton quantum yield. Thus the ratio of the area of these two peaks is described by the relationship below.

$$\frac{QY_{TX} QY_{BX} QY_X}{QY_{BX} QY_X QY_X} \tag{2-3}$$

Where QY_{TX}, QY_{BX}, and QY_X correspond to the triexciton, biexciton and exciton quantum yields respectively. Assuming each successive exciton in the multiexciton cascade is independent, then

29

the ratio of the center and side peaks is the triexciton to exciton quantum yield ratio. It is crucial to note the analogous condition to the biexciton side peak is not three photons after three successive pulses, because it is necessary to cancel the biexciton quantum yield term from the center peak.

2.3.2.6 Triexciton Lifetime

The triexciton lifetime follows the same logic as the biexciton lifetime. First, the photon stream is sorted for all three photon detection events. Since experiments are run under low-flux conditions, these events correspond to almost exclusively triexciton emission. The lifetime of the triexciton is the histogram of delays between the laser pulse and first photon (PNRL$^{(3,0,1)}$), the residual biexciton lifetime is the histogram of delays between the first photon and second photon (PNRL$^{(3,1,2)}$), and the lifetime of the residual exciton is the delay between the second photon and third photon (PNRL$^{(3,2,3)}$). Extracting a lifetime from a fluorescence decay curve requires more total emission counts the longer the lifetime. Due to low total count rates, it is rare that the lifetime of the third photon of a triexciton has sufficient signal to noise to separate NC signal from the uncorrelated background baseline.

2.3.3 Solution Correlation Methods

2.3.3.1 Solution Biexciton Quantum Yield

Similar to the single particle biexciton quantum yield method, Beyler et al.[55] describe how to extract the ensemble-averaged, single-particle biexciton to exciton quantum yield ratio from a solution of freely diffusing emitters. Since there is more than one emitter in the focal volume at any given time, there are two dominant sources of two photon events after a single excitation pulse: emission from a biexciton state on a single nanocrystal and emission of a single exciton from two different NCs. The first case is the signal of interest while the second corresponds to the uncorrelated background of the measurement. By ensuring proper normalization of the signal as described by Beyler et al.,[55] then the biexciton to exciton quantum yield ratio is described by the equation below.

$$\frac{QY_{BX}}{QY_X} = \frac{g_0^{(2)} - 1}{g_\tau^{(2)} - 1} \qquad (2\text{-}4)$$

Where QY_{BX} and QY_X are the biexciton and exciton quantum yields respectively, $g_0^{(2)}$ is the normalized center peak area and $g_\tau^{(2)}$ is the normalized side peak area. The average number of particles in the focal volume is also contained within the correlation trace in the form of the plateau value at early times.

$$\langle n \rangle = \frac{1}{g_\tau^{(2)} - 1} \qquad (2\text{-}5)$$

Note that the average number of particles in the focal volume does not alter the validity of the biexciton to exciton quantum yield method, and in theory concentrations can increase until particle diffusion becomes correlated due to NC-NC interactions.

2.3.3.2 Solution Biexciton Lifetime

Combining the ideas between the solution biexciton quantum yield and single particle biexciton lifetime measurements, the average single particle biexciton lifetime can be extracted from a solution of freely diffusing emitters as described by Bischof et al.[56] This is done by taking the lifetime of the first photon of two photon events, and subtracting out the signal from two photon events corresponding to two excitons on two different nanocrystals. The subtraction of exciton signal is discussed in detail in Chapter 3.

3 Chapter

Experimental Considerations for Photoluminescence Measurements

Measuring the photoluminescence lifetime of fluorescent materials is a key method towards understanding the mechanism of emission and the dominant processes that determine the observable properties of a material. Time-correlated single-photon counting (TCSPC) has been used to measure the dynamics of bulk semiconductors,[57] complex heterostructures,[58] nanomaterials,[29] organic compounds,[59] fluorescent proteins,[60] and many others. For semiconductor materials specifically, the photoluminescence lifetime can contain information on the fundamental electron-hole interactions in the lattice, non-radiative processes,[36] energetic fine-structure,[61] carrier movements,[62] as well as trap state density and depth.[63] Thus, having a robust understanding of how to accurately measure a photoluminescence lifetime for a broad range of samples is crucial. In this section, I present some details on photon-counting detectors, artifacts that are common when utilizing single-photon avalanche photodiodes and how to avoid them, and sources of background in photoluminescence experiments. I will pay particular attention to how to account for and remove background signal in higher-order (≥ 2) correlation measurements commonly used to measure multiexciton behavior in semiconductor nanocrystals. Finally, I will discuss a few particular issues that need to be accounted for in solution-phase correlation measurements.

3.1 Photon Counting Detectors
3.1.1 SPAD
Currently, the most commonly utilized photon counting detector is the avalanche photodiode (APD), also called a single-photon avalanche diode (SPAD). These are the detectors
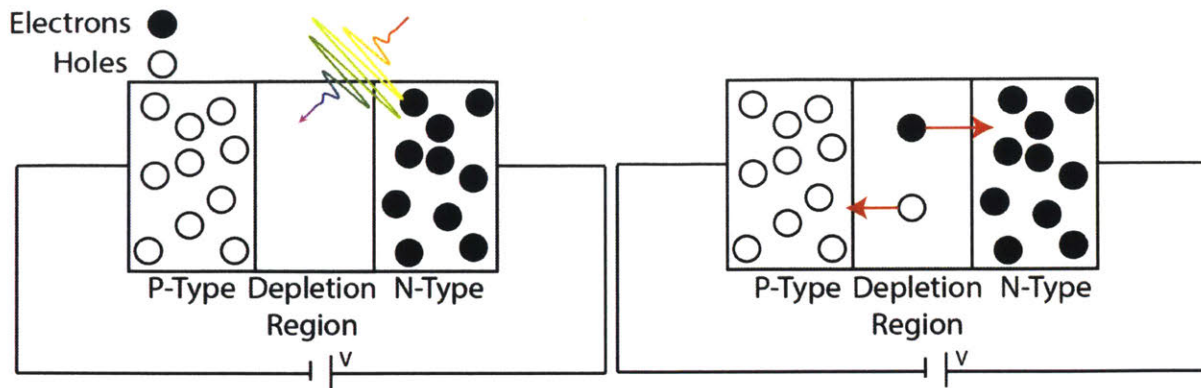
Figure 3-1 Schematic of the active area of an APD illustrating the movement of carriers resulting in a detected current.

used for single-photon counting measurements throughout this thesis, and thus will be discussed most extensively here. The greatest advantage of these devices is the incredibly high sensitivity, and therefore high efficiency at detecting single photons. For silicon-based modules, which are the most common, the detection efficiency in the 550-650 nm range can be as high as 70%. The basic device structure is shown in Figure 3-1. The active area is a silicon p-n junction that is held at a constant, high (100-200V) reverse bias. The bias is large enough such that when a single-photon is absorbed by the detector within the depletion region, the electron and hole that are generated are rapidly accelerated towards opposite electrodes. These accelerated carriers then collide with other electrons or holes in the device with sufficient kinetic energy to cause impact ionization. Successive ionization events increase rapidly causing a so-called avalanche of carriers which are detected as a short burst of current through the circuit and can be recorded with high temporal precision. Disadvantages to this technology include long detector dead times, detector afterpulsing, and poor material systems for infrared photon detection. These properties are discussed in Section 3.2.

3.1.2 PMT

While much less common, photomultiplier tubes (PMT) can also have single-photon detection capabilities. This utilization is quite rare, and PMTs are generally used instead to detect

33

a) Photomultiplier Tube (PMT)   b)   Superconducting Nanowire
                                             Single Photon Detector (SNSPD)

Dynodes   Anode

Photocathode
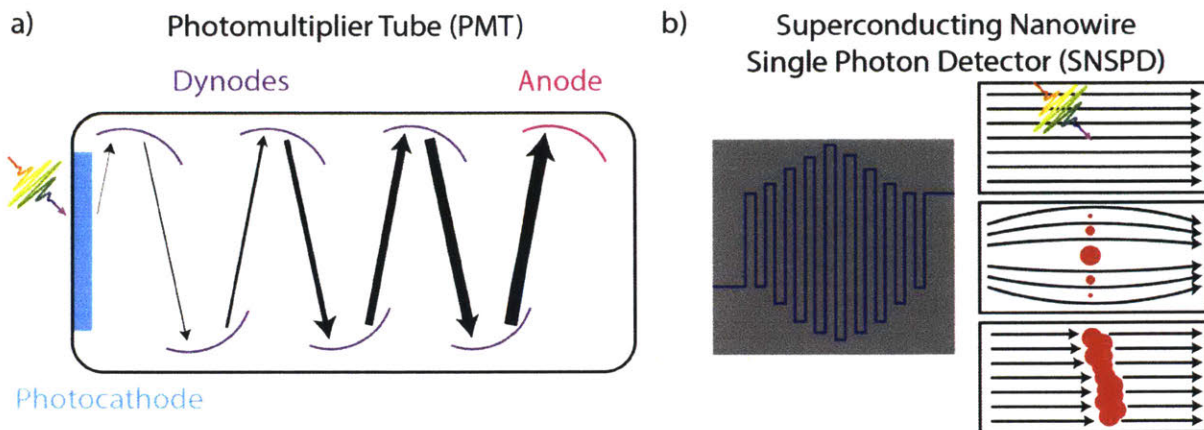
Figure 3-2 a) Illustration of the detection mechanism for incident photons of a PMT. b) Illustration of the active area and detection mechanism for an SNSPD.

a total amount of signal rather than individual photons. Briefly, a PMT operates by converting an incident photon into an electron at a photocathode. This electron is then accelerated through a series of dynodes, which create a cascade of secondary electrons that are eventually detected at an anode (Figure 3-2a). PMTs can generate amplifications of on the order of 10^8; are generally very low noise; and, unlike SPADs, can operate on a beam which is not spatially focused. The largest drawback to using PMTs for single-photon counting (also known as Geiger mode) is a long dead time needed to reset the high voltages necessary for multiplying a single photo-electron.

3.1.3 SNSPD

A newer technology that has recently emerged in photon counting experiments are superconducting nanowire single-photon detectors (SNSPDs). Rather than relying on a burst of current to mark the arrival of a photon, these detectors are kept chilled to ~2K and are made of interleaved superconducting nanowires. The absorption of a photon by the nanowire causes sufficient local heating to result in a burst of resistivity, drastically decreasing the current, which can be recorded as a photon arrival (Figure 3-2b). These detectors show a number of advantages over traditional SPADs. First, SPADs are almost universally silicon-based devices, which limits the detectable range of photons to the bandgap of silicon, inhibiting photon counting experiments

34

in the infrared spectral range. While InGaAs SPADs are available to alleviate this issue, they generally suffer from drastically higher dark count rates, and thus have limited applicability, particularly for single-particle measurements. Based on the broader range of materials which can be utilized to make SNSPDs, they do not suffer this drop-off in the infrared, and in fact, some of the first uses of this technology were for infrared single-photon counting experiments. Furthermore, since these devices are predicated on a jump in resistivity from a single excitation, rather than an avalanche of carriers to generate a current, the reset time and dark count rate are significantly lower. Recently SNSPDs have been used to measure lifetimes and biexciton quantum yields of single infrared-emitting nanocrystals, and to measure the solution-phase single nanocrystal linewidth utilizing solution photon correlation Fourier spectroscopy (S-PCFS) in the Bawendi Group. [64,65]

3.2 SPAD Artifacts

3.2.1 Instrument Response

Most avalanche photodiodes are limited to ~200 ps as the fastest detectable signal. Some thin wafer technologies can achieve detection speeds as fast as a few tens of picoseconds at a trade-off for detection efficiency. This limit is due to the finite and varied time that carriers take to diffuse through the silicon wafer to either electrode. Carrier scattering, or diffusion perpendicular to the direction of bias will broaden the time distribution for each detection event (Figure 3-3). Generally speaking, this time distribution will be the convolution of a Gaussian function with an exponential. Measurement of lifetimes that are shorter than this instrument response function (IRF) limit is not possible, as all fast dynamics will be broadened by the instrument. It is also crucial to recall that the detection limit of the detector itself is not the only thing that broadens fast dynamics - pulsed laser sources with pulse widths on the same temporal scales will also broaden the observed dynamics of a fast emitter.
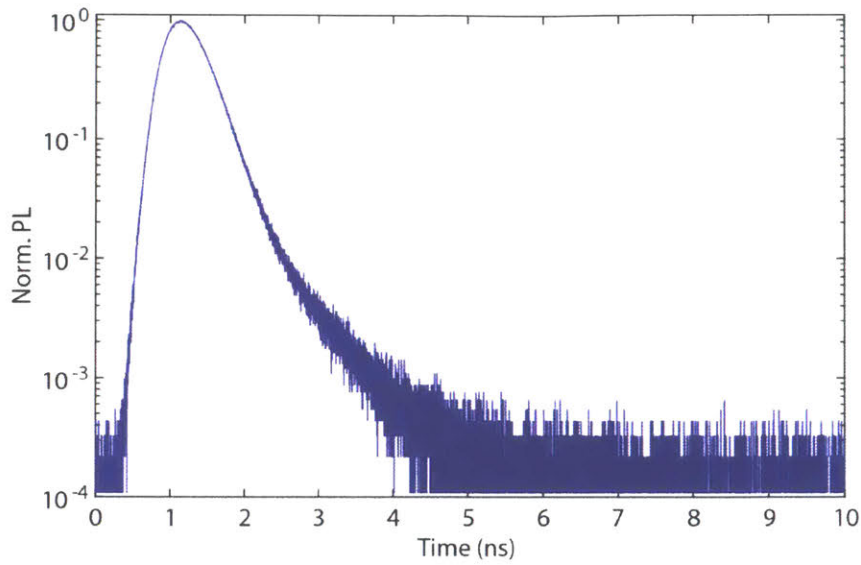
Figure 3-3. Typical instrument response function of Perkin Elmer SPCM-AQR13 single photon detector collected through reflecting the 532 nm excitation source off a silver mirror.

3.2.2 Dead Time

Since the detection of a photon relies on an avalanche of generated carriers in the silicon chip, which can only occur with the detector resting at a reverse bias, SPADs have a significant reset time. Before a detector can record a subsequent photon arrival, all the generated carriers must be swept away and the reverse bias reapplied. This manifests in a many tens of nanoseconds "dead time" when the detector is inactive. Artifacts due to detector dead time are common in photoluminescence measurements, particularly with heterogeneous or defect riddled ensembles or films. Generally, dead time artifacts manifest as a second rise or bump ~80 ns after the original signal rise (Figure 3-4). Most instruments quote a percent maximum count rate of 5% the repetition rate at which there is a high risk of dead time artifacts, but this guideline is not sufficient to avoid artifacts. These numbers assume a fairly constant exponential-like decay which takes most of the laser repetition time to complete. That is to say, the photons are fairly well distributed in time throughout one repetition cycle of the laser. If a sample has a very rapid decay component followed by a long-lived tail, or the repetition rate of the laser is set to be much longer than that of the sample
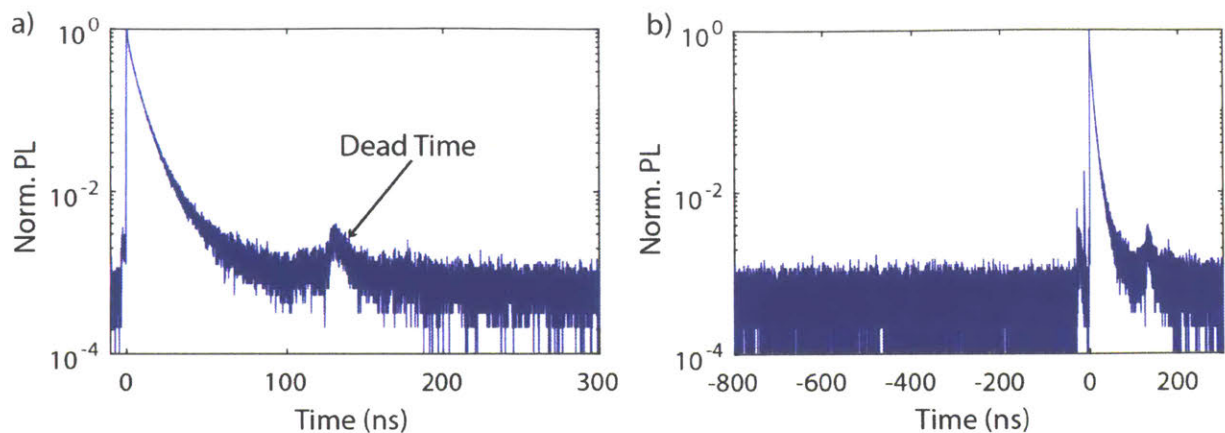
Figure 3-4 a) PL lifetime data of a solution phase ensemble of emitters with a dead-time artifact in the decay curve. b) The whole time trace for the data shown in a) showing a large portion of the repetition window without any NC decay.

emission dynamics, the 5% rule of thumb begins to break down. The data shown in Figure 3-4a was collected well below the quoted threshold for dead time artifacts, but due to the long, fixed laser repetition rate, and relatively short sample lifetime, dead time artifacts are present (Figure 3-4b). For newer generation detector technologies such as SNSPDs, the fact that timing hardware has a dead time too becomes relevant. While a detector may have a dead time on the order of a nanosecond or two, hardware can have dead times of tens of nanoseconds, resulting in the same artifact in the data.

It may be tempting to attempt to mathematically recover the original decay dynamics from a dataset which contains dead time artifacts, but there is no rigorous way to do so. When these issues arise, the dataset in question must be retaken. The multiexponential decay has many different time scales represented, and no fitting of the data after the dead time artifact can recreate the initial trace without *a priori* knowledge of the sample kinetics. The reason this trace cannot be recreated is due to the information loss that occurs when photons arrive in the intermediate time window after the first photon has been detected but before the detector has reset is completely lost. Trying to estimate the arrival time of these photons applies a user bias to the data and is in no way representative of the true PL decay.

37

3.2.3 Afterpulsing

While the detector is in the process of sweeping away excess charges, the detector has an increased probability of producing a second current pulse which does not correlate to the arrival of an additional photon. This process is called afterpulsing and results from the residual carrier avalanche triggering enough electron movement to register as sufficient current and be logged as a detection event. The probability of afterpulsing decreases roughly exponentially with time as shown by the detector autocorrelation signal in Figure 3-5. Due to the detector dead time, we cannot observe afterpulsing occurring before ~80 ns, but only catch the tail of the decay. This artifact is particularly relevant in second- and third-order correlation measurements. To mitigate the effects of afterpulsing, it is crucial to only consider the first photon that arrives at each channel in a single laser pulse. If an experiment is run at a faster repetition rate, it is also crucial to consider afterpulsing events that may be displayed on successive pulses. In order to guarantee no afterpulsing artifacts are present in a dataset, only cross-correlations between detectors should be considered. This is true for both single-molecule measurements and solution-phase measurements. It is also possible for afterpulsing artifacts to be present in lifetime measurements run at relatively low average count rates. Considering only the first photon arrival per 100 nanoseconds or per
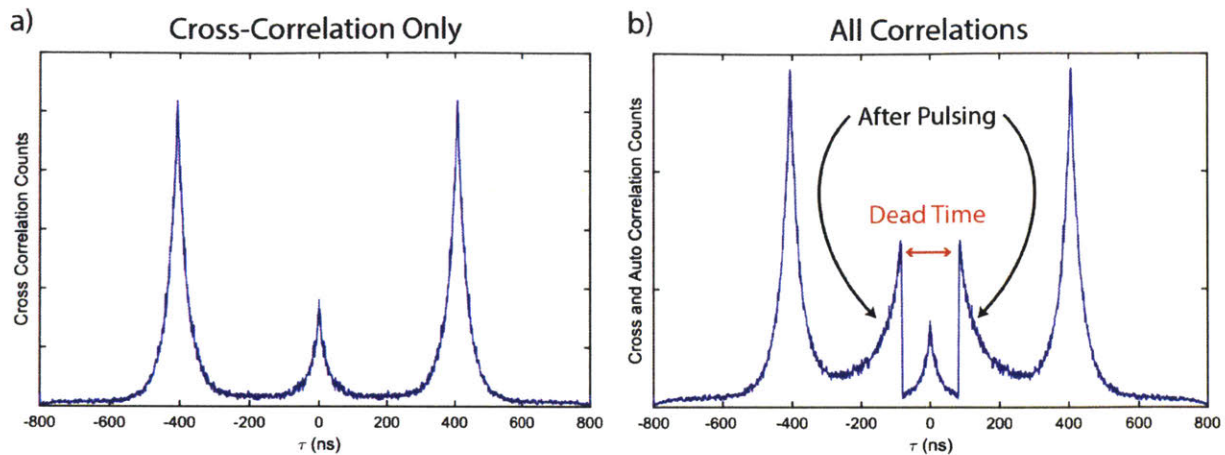
Figure 3-5 a) Second order cross-correlation showing anti bunching. b) Second order cross-correlation and auto-correlation data summed together showing a central anti bunching peak, ~80 ns dead time and a rise in exclusively auto-correlation signal corresponding to detector after-pulsing.

pulse, whichever is longer, per detector eliminates afterpulsing as a source of measurement background.

3.2.4 *Photon Emission*

During a carrier avalanche, almost all generated carriers are converted to detected current and subsequently removed from the silicon wafer. However, it is important to remember that silicon has a small but non-zero quantum yield, and in the presence of so many carriers there is a distinct probability of photon emission from the detector. This emission will correspond to roughly the bandgap of silicon (Figure 3-6a). When doing correlation measurements, it is thus possible for one detector to emit a photon and for that photon to travel through the beam path in the reverse direction to arrive at a different detector some time later (Figure 3-6b). For visible-emitting samples, photon emission can be eliminated simply by the use of short pass filters (Figure 3-6a). For the measurements included in this thesis, cold mirrors are employed in the detection component of the microscope to suppress detector cross-talk. If measurements are in the near-infrared spectral window, it is crucial to measure and subsequently subtract detector cross-talk from any dataset since spectral filtering would interfere with the signal of interest.
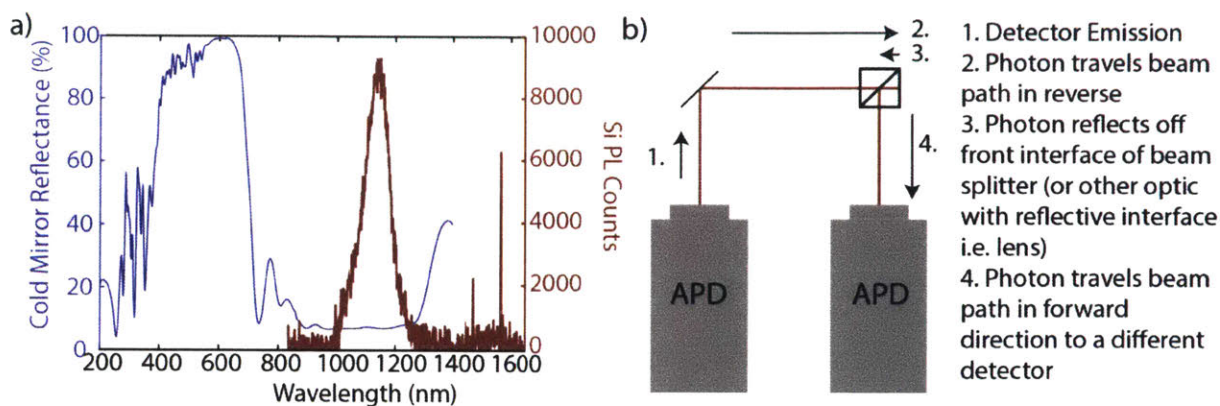
Figure 3-6 a) Spectra of Si photoluminescence (maroon) and percent reflectance of the cold mirrors used to suppress detector cross-talk (blue). b) Beam which causes detector cross-talk.

3.2.5 Chromatic Aberration

Finally, each photon that arrives at the detector is not necessarily equivalent. APDs have differential detection efficiency based upon the wavelength of the photon, with most detectors having optimal efficiency ~600-650 nm, and steep drop offs below 500 nm as well as above 700 nm. When comparing signal between states that emit in different spectral windows, it is crucial to take this efficiency difference into account. If there is enough spectral separation, the area under a given curve is not necessarily representative of the relative emission efficiency of the states in question.

Furthermore, for samples which emit sufficiently fast to be on the same order as the instrument response, it may be tempting to perform a deconvolution of the instrument response from the sample lifetime to measure these dynamics. There are very few situations in which this will give an accurate reporting of the sample dynamics since the instrument response is wavelength dependent. As discussed above, the instrument response is mostly limited by carrier diffusion through the silicon chip. When a blue photon arrives at the detector, it excites carriers much higher into the band structure than carriers created by a red photon. This extra kinetic energy results in

carriers which can diffuse further within the detector, and thus have a wider spread in the average time to generate sufficient carriers and result in a detection event. Therefore, the IRF of most APDs is much broader in the blue than in the red. If an instrument response is measured using a laser which is spectrally shifted from the sample emission, the measured IRF will not be the exact IRF that should be deconvoluted from the sample. Small changes in the IRF can drastically alter the extracted emission lifetime of a sample. Almost universally, for samples which emit faster than the IRF of a given detector, the correct solution is to find a faster detector rather than trying to interpret data that is dominated by the instrument response rather than sample emission.

3.3 Background Signal

3.3.1 Dark Counts

Dark counts are one source of background emission which cannot be systematically removed from an experiment through hardware modifications. Since APDs are operated so close to the threshold voltage for initiating carrier cascades, random thermal fluctuations can initiate this process and result in detection events that do not correspond to the absorption of a photon. Every detector will have a set number of dark counts per second which is the baseline minimum. The models used in this thesis range from 50-400 counts per second. Since these dark counts are not in any way correlated to the sync source, they have no temporal structure and show up as a flat, Poissonian background. If an instrument does not fully suppress outside sources of light, such as room lights or computer screens, these will show up as an increase in that background. The instrument used in this thesis is enclosed in blackout boxes to isolate the optical setup. Also, lens tubes are attached to the detectors to eliminate stray light and ensure operation at a minimum number of dark counts for each detector.

3.3.2 Laser Leakage

Removing all of the signal from the excitation source is also crucial to ensure the measured dynamics correspond only to the particle of interest. Generally speaking, in order to reduce laser light sufficiently below dark count levels, at least seven orders of magnitude of optical density at the excitation wavelength are needed. In the microscope used for these studies, this is achieved using a dichroic filter to separate excitation and emission, as well as a 532 nm notch filter or 425 nm long pass filter, depending on the excitation wavelength. Laser leakage is a fairly simple source of background to correct for once identified, simply by adding additional filters for the appropriate wavelength region.

In experiments where the excitation source is polarized and close in wavelength to the primary source of signal, it is possible to separate based on the polarization of the light rather than the wavelength. Since NCs absorb well into the continuum above the band edge, achieving spectral separation between excitation and emission for photoluminescence measurements is not usually a challenge, and thus polarization is not necessary to filter out excitation sources.

3.3.3 Substrate and Solvent Emission

The most subtle source of background, and the hardest to account for, comes in the form of substrate emission. It is important to realize that many materials are fluorescent, even if only weakly. Amorphous glass has many color centers that emit with a non-exponential lifetime on the order of a few nanoseconds. Beyond glass emission, many organic compounds - especially any with an aromatic group - are fluorescent. Therefore, any residual organic material either on a substrate or in a solution can also fluoresce.

As an example, toluene - an incredibly common solvent for nanocrystal solutions - has a quantum yield of ~17%.[66] This rarely becomes relevant since toluene does not absorb strongly in

the visible spectral region. However, when doing power dependent studies, it is important to remember that not only is the excitation wavelength important, but that two-photon absorption becomes viable at higher powers. Thus, signal from organic fluorescence may be changing with excitation power and should be characterized at all laser powers, not just the lowest experimental fluence.

As for glass emission, this can be resolved usually by using quartz, or sapphire substrates. For applications where amorphous glass is the best substrate option for other reasons, characterization of the background signal becomes crucial.[67] There are two primary methods that can be utilized to measure the background from a substrate. The first is to place a blank substrate in the microscope and measure the dynamics. While this is roughly accurate, many substrates show significant spatial heterogeneity in emission dynamics and intensity, and thus the true background signal for each NC is the exact spot where the NC is located on the substrate. Fortunately, fluorescence intermittency of nanocrystals (discussed extensively in Chapter 2) allows us to characterize the dynamics of the 'off' state, resulting in an accurate measure of the background counts. It is important to exercise caution when employing this technique as not all dark states are truly off. Some are low quantum yield trap or charged states, which are not an accurate measure of background signal.

3.3.3.1 Intensity

Using intensity histograms to identify background states can be quite useful. Individual states will be entirely shot noise-limited, so in the absence of microscope drift, a peak in an intensity histogram which can be fit well by a Poisson distribution is likely a single state. Employing methods such as this to separate emissive states and background states is called thresholding. While thresholding is a fairly straightforward method to separate intensity states, it

comes with a high risk of mixing dynamics between states based on the user selected cut-off. It is best used in systems with very distinct binary blinking patterns with extended on- and off-durations to avoid mixing the dynamics between multiple states.

If thresholding is ineffective or insufficient to separate intensity states and background emission, more advanced mathematical algorithms can be used. The most commonly utilized method is a change-point algorithm, in which the intensity trace is scanned for bins which represent a change in slope of the cumulative sum, then within a bin identifying the specific photon arrival which dictates a distinct change in the behavior. The intensity between each of these identified changes is then averaged to the intensity of the state. The histogram of these states can then be analyzed and fit to a number of models to identify how many true states there are in the total trace, and what the intensity of these states are.[40] Photons can then be separated based on the fitted intensity state, rather than relying on intensity thresholds biased by user-selection. It is crucial to note that while more mathematically rigorous, change-point algorithms are not without user bias, the user inputs are just drastically reduced as compared to simple thresholding techniques.

If background emission cannot be adequately separated from nanocrystal emission using either thresholding or change-point analysis, it is better to just use a blank spot on the microscope slide near to the studied nanocrystal as a measure of the background emission, noting that this will likely produce a less exact background subtraction for the analyses discussed below.

3.3.3.2 Lifetime

The dynamics measured from background sources and from nanocrystal emission are simply additive. Each nanocrystal emissive state should have equivalent amounts of background emission since it has minimal pulse-to-pulse variation over extended periods. Thus, characterizing the exact dynamics from the glass coverslip at the laser excitation wavelength and power used for

measurements (either through intensity trajectory analysis or from a blank spot on the slide, as discussed in the previous section), results in a counts per pulse normalized background lifetime (Figure 3-7). Directly subtracting these background dynamics from the dynamics of nanocrystal emission (also normalized to counts per pulse) leaves only the signal of interest (Figure 3-7a, black). We demonstrate this background subtraction for a binary blinking trajectory and one with many different emissive states, showing that the fast early component can almost entirely be attributed to background emission for all intensity states that were examined.
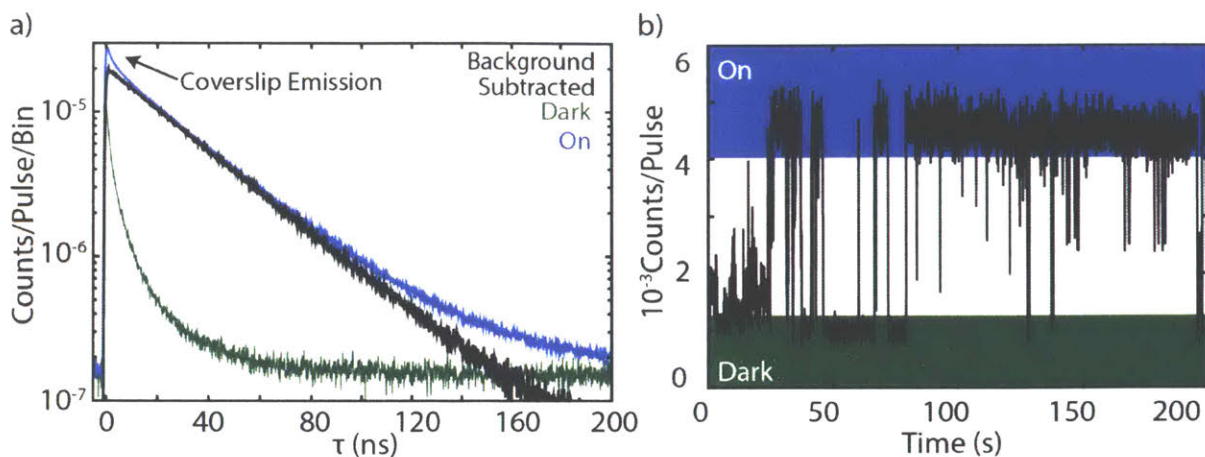
Figure 3-7 a) Background subtracted lifetime utilizing the fluorescence intermittency states illustrated in the intensity trace shown in b).

3.3.3.3 Biexciton

Background emission contributes strongly to any correlation measurement, and is generally ignored or underestimated. There are four possible ways in which a two-photon event (second-order correlation) could occur in a single-particle experiment. These possibilities are: the nanocrystal emits twice, the nanocrystal emits once then the background emits once, the background emits once then the nanocrystal emits once, or the background emits twice. The first case is what results in the signal of interest, but to extract quantum yield or dynamic information
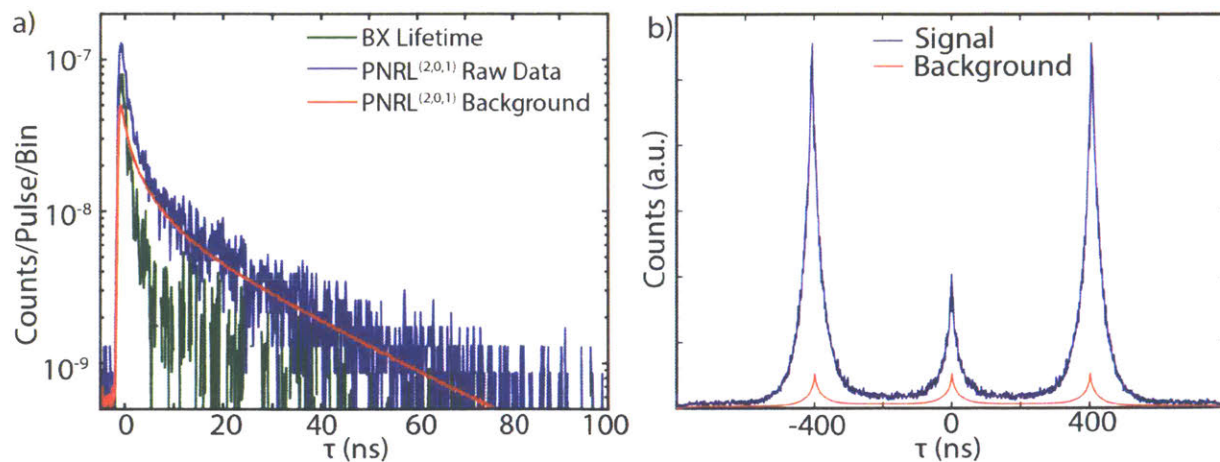
Figure 3-8 a) Raw PNRL$^{(2,0,1)}$ data (blue), calculated PNRL$^{(2,0,1)}$ background signal (red), and background subtracted true biexciton lifetime (green). b) Raw second order correlation counts (blue) and calculated background signal (red).

46

we must subtract out the three other sources of two-photon emission. We can mathematically account for this background signal by taking the marginal probability of the nanocrystal lifetime with the background lifetime, or the background lifetime with itself from the raw lifetime traces collected during the same experiment.

$$PNRL_{NC,Bkg}^{(2,1,0)}(\tau) = g_{NC}^{(1)}(\tau) \int_{\tau}^{\infty} g_{Bkg}^{(1)}(t)dt$$

$$PNRL_{Bkg,NC}^{(2,1,0)}(\tau) = g_{Bkg}^{(1)}(\tau) \int_{\tau}^{\infty} g_{NC}^{(1)}(t)dt \tag{3-1}$$

$$PNRL_{Bkg,Bkg}^{(2,1,0)}(\tau) = g_{Bkg}^{(1)}(\tau) \int_{\tau}^{\infty} g_{Bkg}^{(1)}(t)dt$$

Where $PNRL^{(2,0,1)}$ is the lifetime of the first photon of a two-photon event, $g^{(1)}$ is the one-photon correlation function, or just the lifetime of one-photon events, and the subscripts NC and Bkg correspond to nanocrystal emission and background emission respectively. For quantum yield measurements, the background signal calculated above contributes equivalently to the center peak as well as the side peak since nanocrystal emission and background emission are uncorrelated. Thus the true biexciton to exciton quantum yield ratio can be calculated using equation (3-2).

$$\frac{QY_{BX}}{QY_X} = \frac{A_{center} - A_{Bkg}}{A_{side} - A_{Bkg}} \tag{3-2}$$

Where QY_{BX} and QY_X are the biexciton and exciton quantum yields respectively, A_{center}, A_{side} and A_{Bkg} are the center peak area, side peak area, and background signal respectively. Failure to account for substrate emission when calculating a multiexciton quantum yield will result in an artificially inflated quantum yield value.

3.3.3.4   Triexciton

Similar to the biexciton case, the primary source of background in triexciton measurements arises from a combination of nanocrystal and background emission; either a biexciton and one

background photon, or two background photons and an exciton. The dynamics of this background signal can be calculated analogously to the biexciton background. Background must also be accounted for when calculating a triexciton quantum yield value by subtracting the relevant signals from the "center" and "side" peaks. Since only peak integrated values are utilized for a three-photon correlation, average count rates can be utilized to calculate background signal rather than the dynamics equations shown for the biexciton (equation (3-2)).

$$g_{Bkg}^{(3)} = I_{Bkg}I_{BX} + I_{Bkg}^2 I_X + I_{Bkg}^3 \qquad (3\text{-}3)$$

Where $g^{(3)}{}_{Bkg}$ is the pulse-normalized background signal for a three-photon correlation measurement, I_{Bkg} is the pulse-normalized background intensity, I_{BX} is the pulse-normalized, background-subtracted center peak area of a two-photon correlation, and I_X is the pulse-normalized, background-subtracted exciton emission intensity. Just as with the biexciton, this signal contributes equivalently to both the center and side peak and must be subtracted from both values to extract the true triexciton quantum yield.

3.3.3.5 Solution and Film Ensemble Lifetime

While much less drastically affected by sources of background, there are some sources of background emission in ensemble lifetimes as well. Ensemble lifetimes measured in a film or polymer matrix have the same potential to incorporate glass or organic emission as single-particle measurements. Taking a lifetime of a blank substrate or polymer film at the same excitation power as the measurements provides the necessary signal to subtract. For ensemble measurements, using the same domain is neither as possible nor as crucial since nanocrystal blinking averages out to result in a fairly constant signal with no off time to measure, but averaging of larger substrate domains results in an accurate measure of the background signal with little spot-to-spot variation.

For solution-phase lifetimes, background signal is generally less significant. Laser scatter remains important, but can simply be eliminated by appropriate spectral filtering as described above. Background signal is particularly important for measurements with high excitation fluxes, and should be carefully characterized under all excitation conditions. In particular, organic emission could readily mimic multiexciton emission in a power dependent lifetime series. Careful background characterization can mitigate this problem and allows for accurate measurement of multiexciton dynamics.

3.3.3.6 s-g$^{(2)}$

Solution-averaged biexciton quantum yield measurements have been extensively discussed both by Beyler et al.[55] in their published work as well as in the doctoral thesis of A. P. Beyler.[68] These works contain rigorous derivations of the method as well as a number of practical guidelines to completing the measurement. Here, I highlight and discuss two important considerations for the measurement: sample aggregation and intensity drift.

In order to achieve sufficient signal-to-noise, a solution biexciton quantum yield measurement must be run for one to two hours typically. While samples are generally much more stable in their native organic solution environments, the small sample container and any exposure to air or even just the excitation source can cause changes in the sample. Some examples include changes in ligand coverage and thus quantum yield, sample aggregation allowing for energy transfer between particles, or nanocrystal sintering resulting in particle size changes. All of these types of sample evolution throughout a measurement will invalidate the final result because it is not interrogating a fundamental material property, but rather a distribution among various material states. Samples must be systematically optimized to avoid any of these effects to extract accurate quantum yield values. Some strategies include preparation and encapsulation in the glovebox,

filtering with a syringe filter during sample preparation, dilution in different solvents and solvent mixtures (toluene, hexanes, octane, etc.), and the addition of excess ligand upon dilution. Each nanocrystal sample requires slightly different conditions for optimal preparation, and trial of a few different strategies is usually necessary to obtain stable NC solutions.

There are a few sample changes which do not invalidate experimental results however, and can be mitigated through more nuanced post-processing. These are changes which effectively alter the sample concentration without changing any material properties. The most common case is the adsorption of nanocrystals to the walls of the glass capillary. Samples adhering to the surface will not contribute to the detected fluorescence since the focal volume is well within the capillary, and a pinhole spatial filter is utilized to eliminate out of focus emission. Thus these nanocrystals have simply been removed from the sample, reducing the number of nanocrystals actively diffusing in solution, but not changing their nature. Such changes can be identified through a change in emission intensity but constant fluorescence lifetime over the duration of the measurement.

Unfortunately, changes in concentration do introduce artifacts in correlation results since they lead to intensity correlations on the second to minute time scale. This results in the flat background which must be subtracted not actually being uncorrelated and thus normalized to one, artificially inflating the extracted quantum yield value. To eliminate this bias in the data, the photon stream can be parsed into smaller subsections which have minimal intensity drift. Correlation calculations can then be run on these subsections independently and averaged to achieve the same statistical robustness in biexciton quantum yield without any intensity drift bias (Figure 3-9).
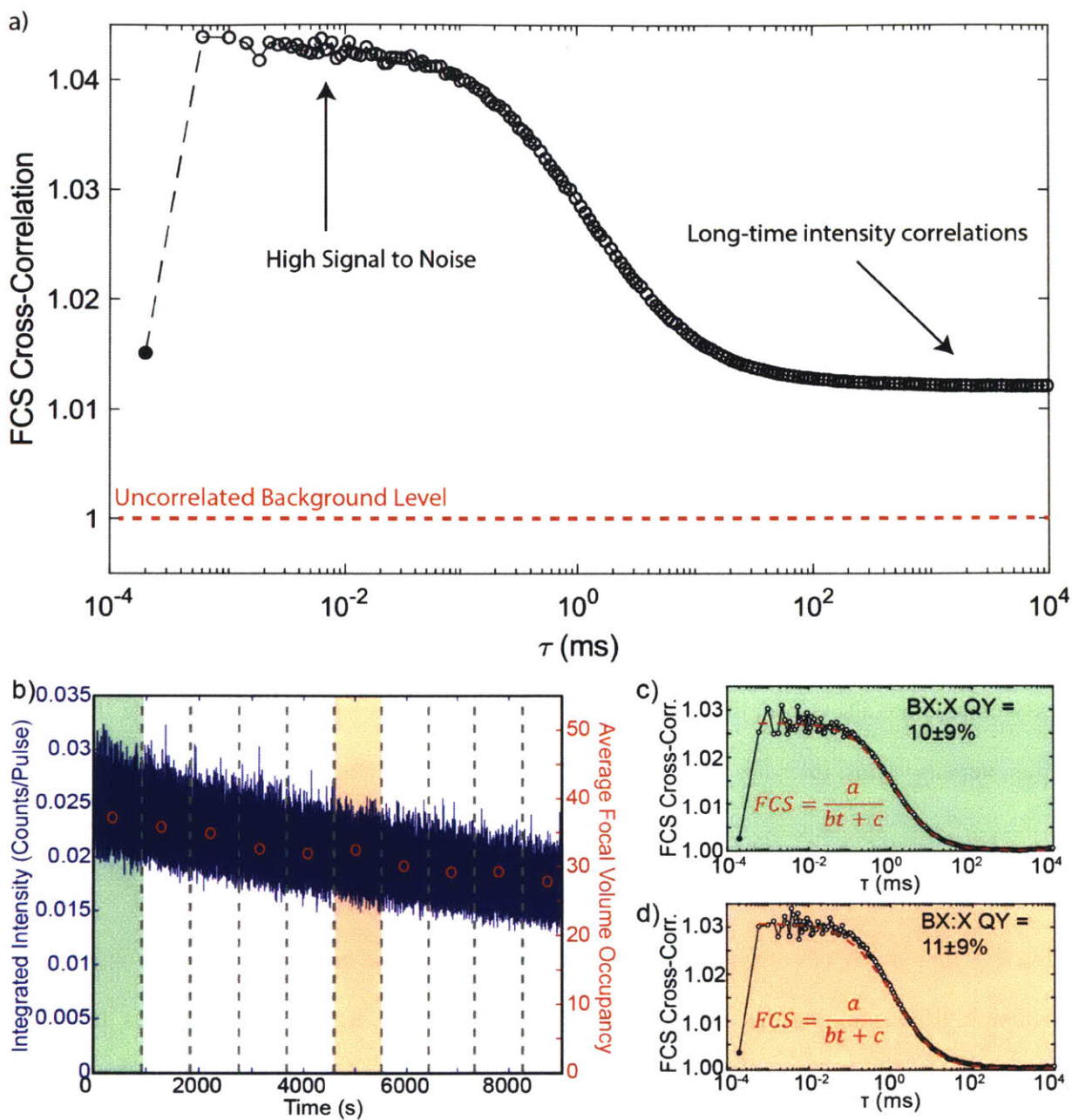
Figure 3-9 a) Normalized second-order cross-correlation for whole experimental window. b) Intensity trace (blue) for the whole experimental window with vertical lines denoting subsections with minimal intensity drift. The red circles correspond to the average occupancy extracted from the FCS fit for each subsection as described by equation (2-5). The green and orange sections correspond to the similarly colored correlation data shown in c) and d).

3.3.3.7 Solution Biexciton Lifetime

Bischof *et al.*[56] detail in their work how to extract the biexciton lifetime from a solution of

freely diffusing emitters as an extension to the solution biexciton quantum yield measurement.

51

Extracting the biexciton lifetime is actually quite similar to the method for which background is subtracted from a single-particle biexciton lifetime. The difference in this case is that the background we are attempting to remove is predominantly from nanocrystal emission. Since we have more than one emitter in the focal volume at any given time, the detection of two photons does not necessarily mean that a biexciton was created. In fact, it usually just corresponds to a single exciton on two different nanocrystals. Thus the background two-photon signal is just the marginal probability of two different nanocrystals emitting a single exciton (equation (3-4)).

$$PNRL_{Soln\,Bkg}^{(2,1,0)}(\tau) = g_{NC}^{(1)}(\tau) \int_{\tau}^{\infty} g_{NC}^{(1)}(t)dt \qquad (3\text{-}4)$$

Where $PNRL_{Soln\,Bkg}^{(2,1,0)}(\tau)$ is the background signal of a solution biexciton quantum yield measurement and $g^{(1)}{}_{NC}$ is the nanocrystal exciton lifetime. Solution biexciton lifetime measurements are also susceptible to intensity drift since equation (3-4) does not scale the same as the intensity. Thus, intensity drift generally results in the oversubtraction of background. This can be partially alleviated by the same method as the quantum yield measurement, slicing the photon stream into smaller sections and individually background subtracting those. Even when doing this though, there is usually a small degree of oversubtraction since the lifetime is more sensitive to drift, and lifetimes are plotted on a log scale, enhancing any small changes. It is also important to take into account unbalanced count rates on different detectors when doing a background subtraction. Most of these calculations assume perfectly balanced detectors. For the four detector case (which is the geometry utilized in this thesis), the correction factor is

$$\sum_{n=i} \left[I_{n=i} \sum_{n \neq i} I \right]$$

Where n is the detector number and I is the average fluorescence intensity at a given detector. This correction factor is calculated by taking the mean value of the intensity trace for each detector, and then determining the probability of detecting a second photon depending on which detector the first photon arrived.

In summary, there is rich information content in the photon stream for both single-particle and solution-phase measurements. Analysis of these photon streams can be riddled with artifacts and errors however, and it is important to recognize where these sources of artifacts or bias may be coming from and how to appropriately account for them through control measurements and background characterization as detailed here.

4 Chapter

Multiexcitons in CdSe Nanocrystals

This chapter is reproduced in part with permission from

Katherine E Shulenberger, Thomas S Bischof, Justin R Caram, Hendrik Utzat, Igor Coropceanu,
Lea Nienhaus, and Moungi G Bawendi

"Multiexciton Lifetimes Reveal Triexciton Emission Pathway in CdSe Nanocrystals"

Nano Letters (2018), 18, 8, 5153-5158.

© 2018 American Chemical Society (ACS)

Contributions: The nanocrystal samples studied in this chapter were either provided by QD Vision, or synthesized by I. Coropceanu according to REF. Data was collected and analyzed by K. E. Shulenberger, S. Coppieters 't Wallant, N. D. Klein, and T. S. Bischof. Analysis was performed utilizing software developed by T. S. Bischof, K. E. Shulenberger, and H. Utzat. Simulations were conducted by A. R. McIsaac, T. Goldzak, and N. D. Klein. The results presented here are reproduced in part from Shulenberger and Bischof et al. and Shulenberger and Coppieters 't Wallant et al. (In Preparation).

Colloidally synthesized cadmium selenide nanocrystals have been an active area of research for many decades.[8] They were first synthesized around three decades ago, and have since become the gold standard nanocrystal for many lighting applications, even if toxicity concerns have inhibited a true explosion into the lighting market.[69-71] CdSe NCs have, nonetheless, provided an excellent platform for fundamental physical interrogation of a material that shares physical properties with both molecular and bulk semiconductor systems, employing insights from both fields to understand their unique nature. This chapter details how exciton-exciton interactions

result in observed multiexciton quantum yields and emission dynamics based on our established understanding of the energetic states in CdSe.

4.1 Background

The band-structure of semiconductors was broadly discussed in the introduction of this thesis, but here I will go into a bit more detail of how a few different theories and levels of approximation relate to established understandings of CdSe NCs. Calculations from k·p theory of the CdSe band-structure, and more specifically the fine-structure of the band-edge state, provide an excellent first understanding of the observed dynamics in CdSe NCs.[72]

The band-edge state of CdSe is comprised of five fine structure states.[73] These states are defined by the total angular momentum of the electron and hole. It may be tempting to consider the spin states of the electron or the hole when approaching from a molecular perspective, but spin is not a "good" quantum number in NCs and our molecular understanding must be modified. As discussed in Chapter 2, these states can be understood by breaking down the wavefunction into two components, a Bloch wavefunction which defines the distribution of carrier density within a unit cell and an envelope function which modulates the intensity of these Bloch states across the nanocrystal. Recombination is dominated by the overlap of carriers at the unit cell level, and thus it is helpful to begin by describing the Bloch states of a pure CdSe nanocrystal. The band-edge is comprised of an electron mostly contained in 5s cadmium atomic orbitals. Thus, we may consider the electron state to be angular momentum 0 and spin $\pm 1/2$, with a total angular momentum of 1/2. The hole is mostly comprised mostly of 4p selenium atomic orbitals. Thus, the angular momentum is ± 1 and the spin is again $\pm 1/2$ to combine to a total angular momentum state of 3/2. Table 4-1 illustrates the different combinations of electron and hole angular momentum states which result in the five exciton fine-structure states observed in CdSe.

Table 4-1 Possible electron (left) and hole (top) angular momentum states for band-edge carriers and the resulting total angular momentum of the exciton state.

Electron \ Hole	-3/2	-1/2	1/2	3/2
-1/2	-2	-1	0	1
1/2	-1	0	1	2

These states are well described in detail by Norris et al.[73] Importantly, the lowest energy state for all nanocrystal sizes is the ± 2 state. Since a photon may only carry an angular momentum of ± 1 and the NC ground state has angular momentum 0, the lowest energy fine-structure state in CdSe is dark. The next fine-structure state is the $\pm 1^L$ state, which is bright. The energy splitting between the lowest energy dark state and the bright state is predominantly determined by the exchange interaction, but is at most ~10 meV.[73] Therefore, conversion between these states is readily thermally accessible and has been shown to happen on picosecond timescales, much faster than radiative emission.[74,75] Throughout this thesis, the interchange between the bright and dark state is depicted graphically as a spin flip. While this is a useful mental picture, it is not rigorously accurate. Due to the high density of states for the hole and the lower degree of atomic orbital purity, transfer between the bright and dark fine-structure states involves an angular momentum change for the hole rather than just an electron spin flip. Due to the smaller energy separation and rapid exchange, an ensemble can be accurately considered as having equal populations in the bright and dark states, as follows from a Boltzmann distribution. For a single excitation this means spending roughly an equal amount of time in both the bright and dark states throughout its lifetime. It is important to remember that this approximation is only true at room temperature, where thermal energy is large compared to the fine-structure splitting. The fine-structure of CdSe has been confirmed through a number of studies utilizing methods such as steady-state absorption of highly

monodisperse ensembles and theoretical calculations.[72,76] Furthermore, the existence of a dark ground state is confirmed by the low temperature fluorescence lifetime which extends from nanoseconds to microseconds between room temperature and 4 K.[77]

When expanding to consider multiexciton states, first, the energetic states which are occupied must be identified. Due to the band-edge state occupancy of two (which results from the double-degenerate electron state), the biexciton occupies two electron and hole angular momentum states within the fine-structure manifold discussed above.[74] This state is modulated by a spherically symmetric S-like envelope function. The next energy state is comprised of the same Bloch wavefunctions, but is instead modulated by a P-like envelope function across the nanocrystal. This state is where the third exciton resides when considering a triexciton. It is important to note that the state ordering for a single exciton, as observed in a steady-state absorbance spectrum, is not the same as the state ordering for occupation of multiexcitons. Level-level repulsion of states with high degrees of overlap, such as the $1S_{3/2}$ and $1S_{1/2}$ hole states, alter the energies. This results in the triexciton occupying the $1P_e 1P_{3/2}$ state for all nanocrystal core sizes.[78]

While these states have been well studied both through experimental and theoretical works, there are still a number of open questions surrounding recombination dynamics and quantum yield from multiexciton states in CdSe NCs. The quantum yield of multiexciton states as compared to the exciton state is dominated by direct competition between radiative emission and non-radiative Auger recombination. As described in Chapter 2, Auger recombination is the process where an exciton recombines and rather than emitting the energy as light, transfers energy to a third carrier (either an electron or a hole), which subsequently rapidly thermalizes back to the band edge. The end result is exciton recombination without radiative emission. The Auger rate in nanocrystals is dominated by the electron-hole overlap, and the density of final states accessible to the third

carrier, which must be promoted deep into either the valence or conduction band. Numerous theoretical studies have attempted to model the Auger rate in both core-only and core-shell heterostructures.[46,79,80] Recently, it has been reported that a smooth potential boundary between the core and the shell through material alloying results in more delocalized carriers and smoother carrier density profiles, leading to drastically reduced Auger rates.[81,82] This theory was beautifully demonstrated by Nasilowski et al.[83] where they synthesized gradient CdSe/CdS nanocrystals with unity biexciton quantum yield.

The radiative rate for any state is dominated by the energy of the transition and the electron-hole wavefunction overlap. Klimov et al.[84] thoroughly interrogated a number of scaling models for multiexciton lifetimes and concluded that statistical scaling best describes these lifetimes. However, these methods are based on a number of assumptions and do not directly interrogate exclusively the biexciton state. The main basis of the statistical scaling model is that the primary change in radiative lifetime between multiexciton states is due to the multiplicity of recombination pathways, and that the underlying mechanism remains constant. Pictures such as those shown in Figure 4-1 are frequently drawn to illustrate the point for the biexciton state.
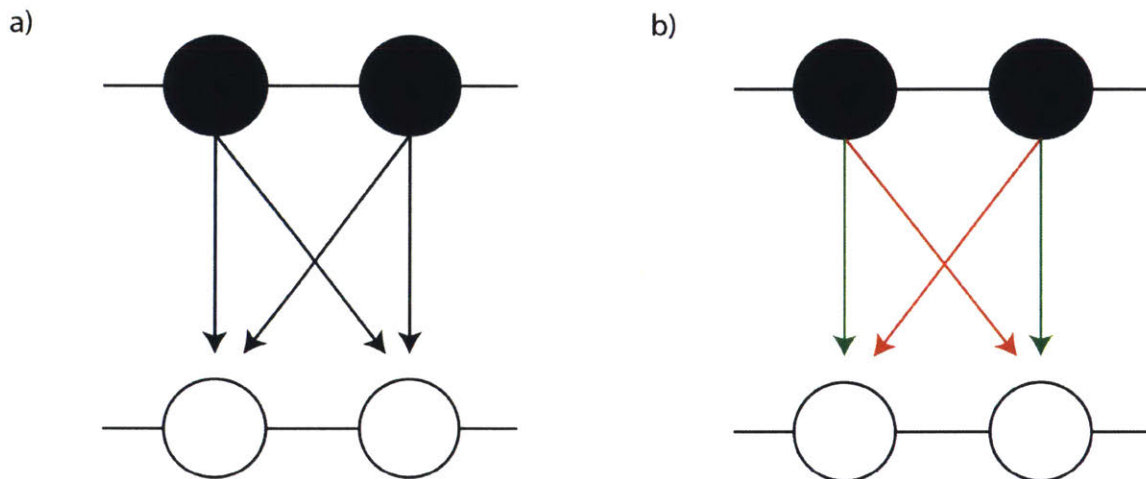
Figure 4-1 a) Frequently drawn illustration explaining the statistical scaling factor of four. b) Illustration of the emissive (green) and non-emissive (red) transitions within this illustration scheme.

Polarization-dependent two-dimensional photon echo spectroscopy among others have been utilized to investigate the fine structure of the biexciton.[85] The biexciton can be simplified to linear combinations of the possible electron and hole angular momentum states in the same manner as was done for the exciton. For example one biexciton state is depicted in Table 4-2 with the possible electron and hole recombination pathways highlighted in color.

Table 4-2 Depicts one possible biexciton state and the relative angular momenta of the four carriers which comprise the state. There are two pairwise radiative excitons in this state, and two pairings which would result in an angular momentum change not equal to ±1 which are therefore not emissive. These pairing are depicted in blue and green.

Exciton	Electron	Hole
2	1/2	3/2
-2	-1/2	-3/2

Note that only two electron-hole pairs are bright, unlike the four recombination possibilities usually demonstrated, bringing into question the statistical scaling model. For further details, Wong et al.[85] have a thorough description of the biexciton states. Crucially, the lowest energy biexciton states are all bright since there are a number of fine structure states in the exciton manifold which can allow for a transition of ±1. By combining an understanding of the exciton and biexciton states, in which the exciton spends roughly half its time in a dark state and the biexciton has exactly two bright recombination pathways, the statistical scaling factor of four between the radiative exciton and biexciton lifetimes is recovered.

To test the statistical scaling model, and extend these ideas to triexciton recombination, I utilized the fluorescence microscope and analysis algorithm described in Chapter 2, optimized for multiexciton dynamics detection. Number-resolved, time-correlated single photon counting spectroscopy of individual NCs provides a clean platform for these experiments due to the lack of heterogeneity in observed rates, and the ability to identify behavior of a specific state through

photon counting. The samples studied here consist of core-shell spherical CdSe NCs. Unless otherwise specified, samples are core/shell CdSe NCs obtained from QD Vision. Shell thickness studies were performed on a series of CdSe/CdS NCs with 1 to ~8 monolayers of CdS synthesized according to Coropceanu *et al.* [25]

4.2 Biexciton Statistical Scaling

When operating at low-flux ($<N> \leq 0.01$), NC emission is only ~5 times as intense as background emission. Therefore, background dynamics must be thoroughly characterized to isolate NC signal. This is described in detail in Chapter 3. Briefly, we exploit the binary blinking of NCs (Figure 4-2 inset). In Figure 4-2 the PL lifetime of both the 'on' (blue) and 'dark' (green) states are plotted based on thresholds derived from the fluorescence intensity trace (Figure 4-2, inset). The dynamics of the dark state, plotted in Figure 4-2, are dominated by emission from the substrate, verifying that the origin of the dark emission is predominantly unrelated to the NC. To
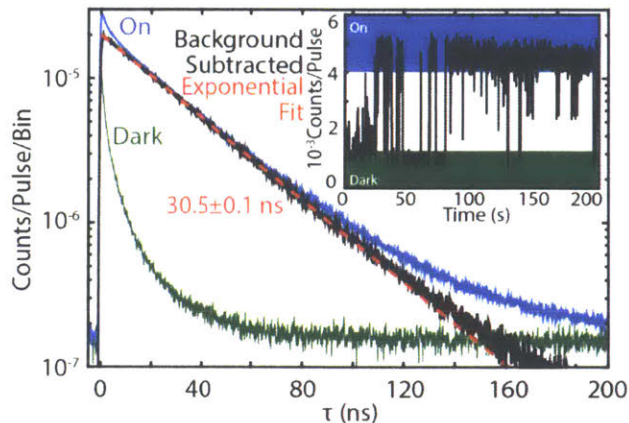
Figure 4-2 Fluorescence lifetimes of intensity states as defined in the inset. The red dotted line is an exponential fit to the background subtracted fluorescence lifetime.
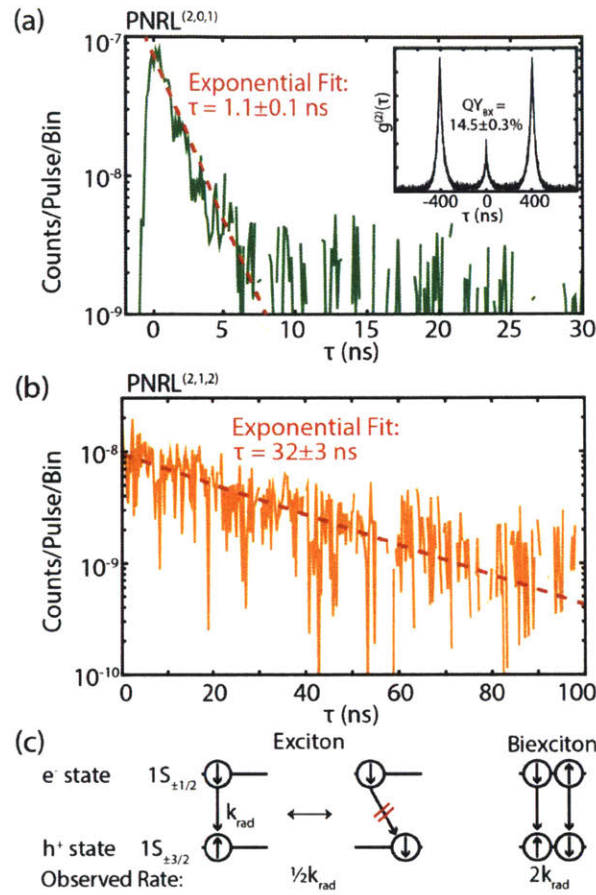
Figure 4-3 . (a) Background subtracted biexciton lifetime (green). Data is fit to a single exponential (red). Inset is the second order correlation ($g^{(2)}$) for the same experiment. (b) Lifetime of the second photon emitted from a biexciton. Fit (red) is a single exponential. (c) Illustration of the origin of the difference in radiative rates for an exciton and bound biexciton in CdSe NCs.

obtain the intrinsic NC lifetime the 'dark' emission dynamics are subtracted from the on-state dynamics, effectively isolating NC emission. This leads to a mono-exponential decay for exciton emission (Figure 4-2, black). The PL decay is fit to a single exponential to extract a radiative lifetime of 30.5±0.1 ns, which is consistent with previously reported values for similar NCs.[30,86]

To establish the effect of multiexciton interactions on the radiative recombination rate, the PNRL algorithm is utilized to measure the lifetime of the biexciton and compare that to the exciton dynamics.

$$r_{BX/X} = \frac{k_{rad,BX}}{k_{rad,X}} = \frac{\tau_X/QY_X}{\tau_{BX}/QY_{BX}} \qquad (4\text{-}1)$$

Where $r_{BX/X}$ is the scaling factor between the exciton and biexciton radiative rates, $k_{rad,BX}$ is the biexciton radiative rate, $k_{rad,X}$ is the exciton radiative rate, τ_X is the exciton lifetime (Figure 4-2, black), QY_{BX}/QY_X is the biexciton to exciton quantum yield ratio (Figure 4-3, inset), and τ_{BX} is the biexciton lifetime. All of these values can be determined through low-flux photon counting techniques.

Due to the low fraction of biexciton emission events, the biexciton lifetime is particularly sensitive to systematic error due to two-photon events with one photon originating from a background source as described in Chapter 3. Taking the marginal probability of the lifetime of the exciton and the background produces the background signal for two-photon dynamics.

$$PNRL_{bkg}^{(2,0,1)}(\tau) = PNRL_{off}^{(1,0,1)}(\tau) \int_{\tau}^{t_{rep}} PNRL_{NC}^{(1,0,1)}(t)dt$$

$$+ PNRL_{NC}^{(1,0,1)}(\tau) \int_{\tau}^{t_{rep}} PNRL_{off}^{(1,0,1)}(t)dt \qquad (4\text{-}2)$$

Where $PNRL_{bkg}^{(2,0,1)}$ is the two-photon event lifetime background signal, t_{rep} is the laser repetition rate, $PNRL_{off}^{(1,0,1)}$ is the lifetime of the dark state (Figure 4-2, green), and $PNRL_{NC}^{(1,0,1)}$ is the NC exciton lifetime (Figure 4-2, black). Subtracting the dynamics calculated using equation (4-2) from the total $PNRL^{(2,0,1)}$ signal isolates the true biexciton dynamics (Figure 4-3). A thorough description of background characterization methodologies can be found in Chapter 3. Additionally, since NC and coverslip emission are uncorrelated, the background emission described by equation (4-2) contributes equally to the center and side peaks in a $g^{(2)}$ correlation measurement as well and must be subtracted to extract the biexciton quantum yield (Chapter 3). Failure to do so artificially

increases the calculated biexciton yield. The NC presented in Figure 4-3 has a value of 14.5±0.3% for the background subtracted biexciton to exciton quantum yield ratio (QY_{BX}/QY_X) as compared to 20.3 % for the uncorrected ratio.

The $r_{BX/X}$ extracted using equation (4-1) for this NC is 4.0±0.1 based on the measured biexciton to exciton quantum yield ratio (14.5%), the exciton lifetime (30.5 ns), and the measured biexciton lifetime of 1.1 ± 0.1 ns (Figure 4-3). This result is consistent with statistical scaling of the state as illustrated in Figure 4-3c,[84] which predicts a factor of 4 increase in rate for the biexciton relative to the exciton. To reiterate, the origin of this factor of four is as follows. At room temperature, only half of the exciton's are available to radiatively recombine due to angular momentum selection rules. This is due to two factors: 1) the hole can rapidly spin mix (<10 ps), much faster than the radiative recombination time,[74,87,88] and 2) the spin-allowed and spin-forbidden states are only split by ~1-5 meV, well within k_BT at room temperature. This leads to equal populations of the two states (±2 (dark), ±1^L (bright)), with fast phonon-mediated exchange between them.[74,75] For the bound biexciton manifold, there are two spin-paired exciton's which can recombine independently, giving rise to a radiative speed up by a factor of two compared to a single spin-paired exciton. The combination of the factors of ½ (for the exciton) and 2 (for the biexciton) results in a biexciton radiative rate four times faster than that for the exciton.[41,56,84,89]

Next, I address the lifetime of the subsequent photon after biexciton recombination. Figure 4-3b plots the delay between the first and second photon of a biexciton ($PNRL^{(2,1,2)}$). For this NC, the $PNRL^{(2,1,2)}$ lifetime is 32±3 ns which is consistent with the exciton lifetime of 30.5±0.1 ns. The agreement between these lifetimes indicates the exciton has no memory of the multiexciton state from which it originated. The lack of memory confirms that in the absence of NC charging, all losses in device efficiency under high-flux excitation originate from low multiexciton QY rather

than any change to the exciton emission pathway, and therefore, the best way to improve device performance is the reduction of Auger rates.
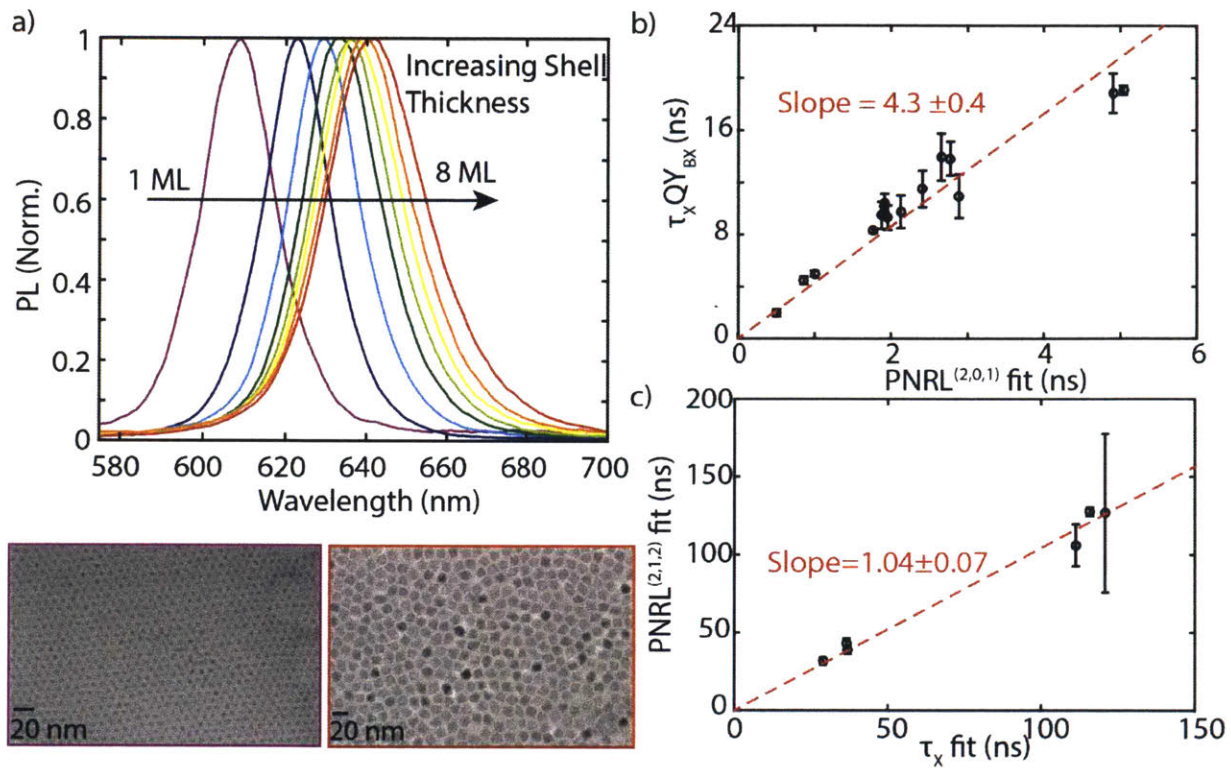
Figure 4-4 a) PL spectra of the shell series used for panels b and c. The two TEM images are of the smallest and largest shell size. b) Comparison of the biexciton lifetime and the product of the exciton lifetime and biexciton quantum yield. The data is fit to an error weighted first order polynomial (red). c) Comparison of the exciton lifetime and PNRL[(2,1,2)] with an error-weighted linear fit (red).

Since biexciton emission in a core-shell CdSe NC is consistent with the bound biexciton model illustrated in Figure 4-3, and the residual exciton has no memory of the higher excited state, it is only natural to explore a shell-series. CdSe/CdS is a quasi-type II heterostructure where the electron delocalizes into the shell and the hole remains confined to the core, decreasing the electron-hole wavefunction overlap and increasing the exciton lifetime.[55] Increasing shell thickness also reduces the exchange energy, therefore decreasing the fine-structure splitting.[90] Figure 4-4b plots the measured biexciton lifetime against the product of τ_X and QY_{BX}. The data in Figure 4-4b is fit to a linear function to extract $r_{BX/X}$ from the slope (equation (4-1)).

The extracted slope is 4.3±0.4 from an error-weighted fit to a first-order polynomial with the intercept set to the origin. This result indicates universal agreement between biexciton emission and the bound biexciton model for shell thicknesses studied here. Figure 4-4c plots the exciton lifetime against the lifetime of the second photon of a biexciton. Error-weighted fitting to a first-order polynomial with the intercept set to the origin gives a slope of 1.04±0.07. The equivalence between the two lifetimes across all shell thicknesses confirms that previously reported rapid spin mixing is sufficient to ensure subsequent exciton emission has no memory of its previous state in these NCs.[74,87]

4.3 Triexciton Scaling

$$QY_{TX} = \frac{C}{S} = 12.3 \pm 0.6\%$$
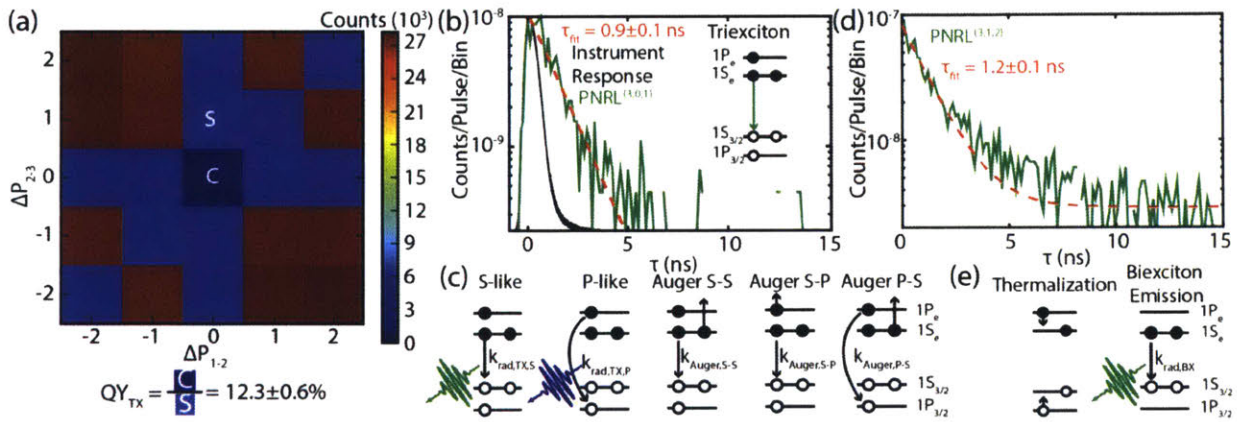
Figure 4-5 . a) Pulse resolved $g^{(3)}$ experiment. ΔP_{1-2} indicates the pulse difference between photons 1 and 2, ΔP_{2-3} indicates the pulse difference between photons 2 and 3. The ratio of the counts of the "center" (C) to "side" (S) peak is used to calculate the triexciton quantum yield. b) Triexciton lifetime (green) fit to a single exponential (red). The instrument response is plotted in black for comparison. c) Possible pathways for triexciton recombination in CdSe/CdS NC, as described in this study. This includes both radiative pathways as well as three Auger pathways. d) Plot of PNRL$^{(3,1,2)}$ (green) with a fit to an exponential plus a constant (red). e) Recombination pathway of second photon emission immediately after S-like triexciton emission.

Moving on from the biexciton state, state-specific quantum yields and dynamics can also elucidate the dominant processes which control triexciton recombination. Figure 4-5 shows the extension of the number resolution measurements to triexciton emission. Figure 4-5a is a plot of the pulse-integrated third-order correlation. ΔP_{1-2} is the pulse difference between the first and second photon and ΔP_{2-3} is the pulse difference between the second and third photon. The

analogous positions to the center ('C') and side ('S') peaks in a second order correlation experiment are marked on the plot. The triexciton quantum yield can be calculated from an extension of the methods described by Nair *et. al.* and Beyler *et. al.* (Chapter 2).[53,55]

$$g_0^{(3)} = \frac{G_3}{G_2 G_1} = \frac{QY_{TX}}{QY_X} \tag{4-3}$$

Where $g_0^{(3)}$ is the third-order correlation, G_3 is the area of the center peak (three photons detected after the same laser pulse, Figure 4-5a 'C'), the product of G_2 and G_1 is the area of the side peak (two photons are detected after a single laser pulse and one photon on the subsequent pulse, Figure 4-5a 'S'), and QY_{TX}/QY_X is the triexciton to exciton quantum yield ratio. The triexciton to exciton quantum yield ratio for this NC is 12.3±0.6%.

The relative increase of the triexciton radiative lifetime as compared to the exciton lifetime can be extracted in a manner similar to the biexciton scaling rate as presented in equation (4-1).

$$r_{TX/X} = \frac{k_{rad,TX}}{k_{rad,X}} = \frac{\tau_X/QY_X}{\tau_{TX}/QY_{TX}} \tag{4-4}$$

Where $r_{TX/X}$ is the relative speed up of the triexciton radiative rate compared to the exciton, $k_{rad,TX}$ is the triexciton radiative rate, $k_{rad,X}$ is the exciton radiative rate, τ_X is the exciton lifetime, QY_{TX}/QY_X is the triexciton to exciton quantum yield ratio, and τ_{TX} is the triexciton lifetime. The value of $r_{TX/X}$ can be predicted for either S-like or P-like emission. Fermi's Golden Rule can be used as a basis to predict the rate of P-like emission.[91]

$$k_j \propto \omega_j |\langle i|\boldsymbol{p}|j\rangle|^2 \tag{4-5}$$

Where k_j is the rate of emission from state j, ω_j is the energy of the state j, and $|\langle i|\boldsymbol{p}|j\rangle|^2$ is the momentum overlap between states i and j. Since both the S-like and P-like states originate from the same Bloch wavefunction, the momentum overlap should not differ appreciably.[92] The energy

difference between the states in spherical NCs (<250 meV) only causes a 10% difference in the radiative rate, at most.[93] Additionally, the P-like state has similar fine-structure to the S-like state, resulting in the same factor of 1/2 decrease in the emission rate as compared to a purely emissive state[78]. Therefore, the radiative lifetime of the P-like state ought to be within 10% of the lifetime of the exciton. For triexciton emission originating from the S-like state, the radiative lifetime ought to be equivalent to the biexciton radiative lifetime. Thus, $r_{TX/X}$ will be ≈1 for pure P-like emission, $r_{TX/X}$ will be 4 for pure S-like emission, and $r_{TX/X}$ will be ≈5 if both S-like and P-like pathways are active in triexciton recombination. If both pathways are active, emission will be dominated by the faster S-like emission.

The ratio of $r_{TX/X}$ is 4.2±0.6 for the triexciton, based on equation (4-4) as well as a triexciton lifetime (Figure 4-5b) of 0.9±0.1 ns, a triexciton to exciton quantum yield ratio of 12.3%, and an exciton lifetime of 30.5 ns. Since 4.2 falls between the predicted value for pure S-like emission and for both S-like and P-like emission simultaneously we conclude that triexciton emission dynamics are dominated by S-like recombination.

Previous studies have demonstrated emission from the P-like state via a spectral shift under high-flux excitation, but unlike here these works have not exclusively isolated triexciton emission from that of higher-order multiexcitons.[93–95] The analysis above indicates that in order to observe significant P-like emission from a NC, multiexcitons higher than third order are necessary to overcome S-like emission. Indeed, these previous studies had an average of more than two excitons per NC, consistent with this hypothesis.

The next contributions to address are the non-radiative processes that control the triexciton quantum yield. First, using the statistical scaling results calculated above allows the determination of the Auger rate for both the biexciton and triexciton. Assuming that the emission rate extracted

from the exciton lifetime is the radiative rate, which implies the QY_X is 100%, the values measured above can be used with an alternate definition of the biexciton quantum yield to extract Auger rates. The biexciton Auger rate can be calculated from the biexciton quantum yield and the bound biexciton radiative rate of four times the exciton radiative rate, or 0.131 ± 0.002 ns^{-1}.

$$QY_{BX} = \frac{k_{rad,BX}}{k_{rad,BX} + k_{nr,BX}} \tag{4-6}$$

Where QY_{BX} is the biexciton quantum yield, $k_{rad,BX}$ is the biexciton radiative rate, and $k_{nr,BX}$ is the biexciton Auger rate. We find the biexciton Auger rate is 0.77 ± 0.06 ns^{-1} for this NC. Similarly, an Auger rate can be extracted for the triexciton.

$$QY_{TX} = \frac{k_{rad,TX}}{k_{rad,TX} + k_{nr,TX}} \tag{4-7}$$

Where QY_{TX} is the triexciton quantum yield, $k_{rad,TX}$ is the triexciton radiative rate, and $k_{nr,TX}$ is the triexciton Auger rate. The triexciton Auger rate for this particle is 1.0 ± 0.2 ns^{-1}. Even with multiple new Auger processes between S-like and P-like carriers due to the addition of a third exciton to the system, the total Auger rate is similar for the biexciton and triexciton. Thus, the newly added pathways are likely much slower than Auger processes between carriers residing in the band edge S-like state, and the addition of a third exciton does not greatly alter the rate of S-like Auger processes. The similarity in both radiative and Auger rates of the biexciton and triexciton account for the similar quantum yields measured for the states.

Measurement of PNRL[3,1,2] (Figure 4-5d) indicates that the lifetime of the second photon from a triexciton (1.2 ± 0.1 ns) is equivalent to the biexciton lifetime (1.1 ± 0.1 ns) measured by PNRL[2,1,2], showing a continued lack of system memory. With the triexciton emission arising primarily from the S-like state, thermalization must be sufficiently rapid that P-like emission from
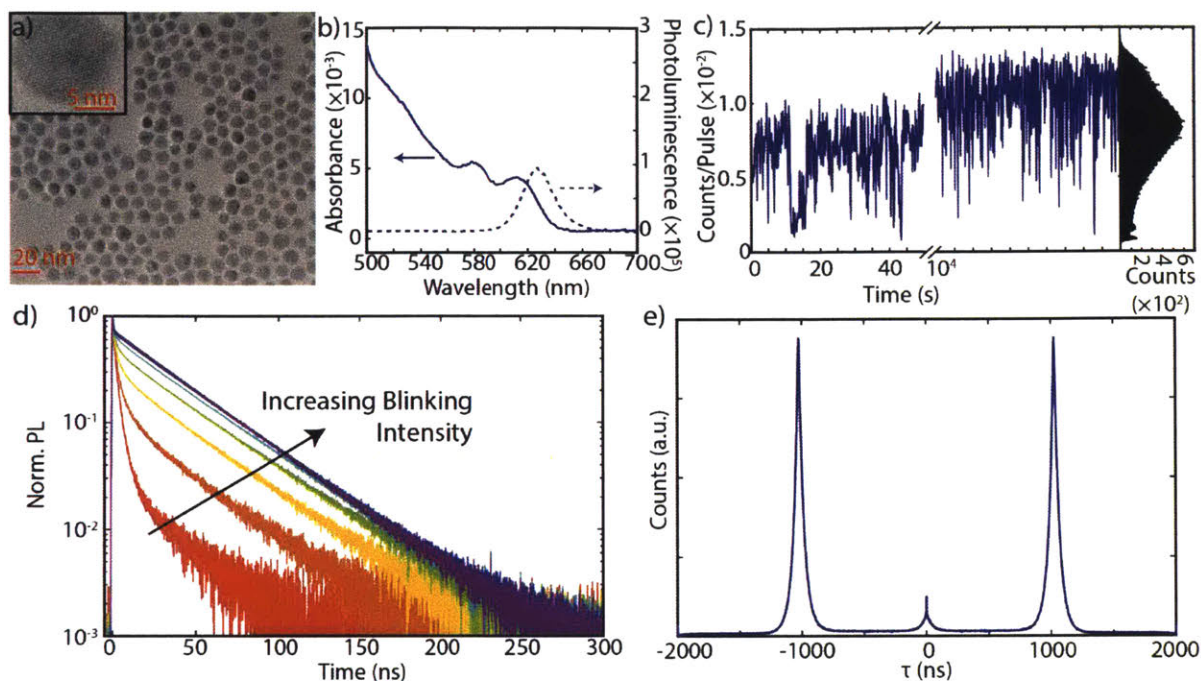
Figure 4-6 a) TEM image of core-shell CdSe/CdS NC sample. b) Steady-state absorbance and photoluminescence spectra of the NC sample. c) Fluorescence intensity trace from a single NC early and late in the ten hour integration and a histogram of the intensity states for the whole measurement. The oscillations in maximum intensity are due to thermal fluctuations in the environment. d) Fluorescence lifetimes of the different intensity states shown in c). e) second-order correlation data of the highest intensity state from panel c).

the newly created hot biexciton does not occur (Figure 4-5e). This is consistent with previous experiments studying the thermalization rate in CdSe NCs and with spectrally resolved $g^{(2)}$ measurements showing that P-like emission always precedes S-like if P-like emission occurs.[96–99]

Having shown that the emission dynamics of the triexciton state are consistent with dominant behavior from the S-like state, the next step is to directly measure the branching ratio between S-like and P-like emission.

For this measurement, studies were restricted to the core/shell CdSe/CdS sample obtained from QD Vision due to the excellent optical stability of the nanocrystal sample. Transmission electron microscopy images of the sample are shown in Figure 4-6a. While a considerable degree of nanocrystal heterogeneity is observed in the sample, the full width half maximum (FWHM) of

69
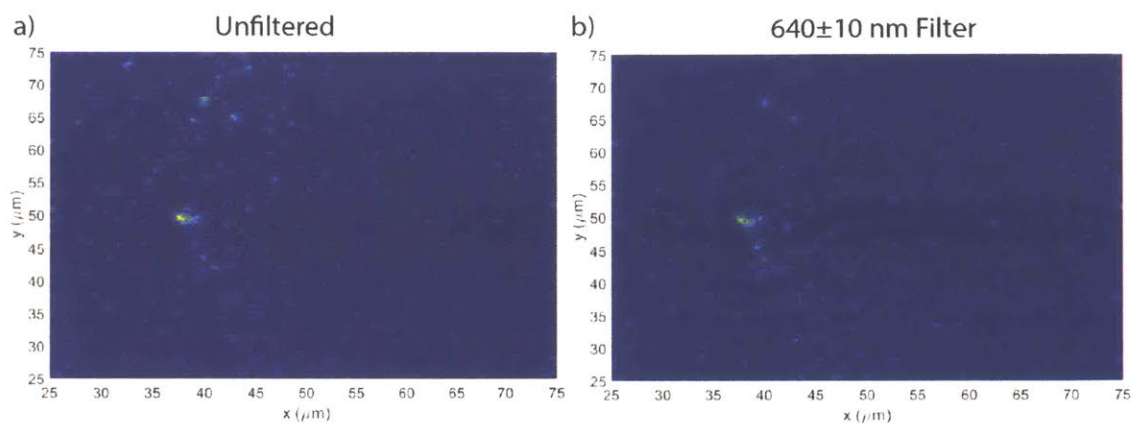
Figure 4-7 a) Fifty square micrometer raster scan with 400 pixels in each direction with no spectral filter. b) Fifty square micrometer raster scan with 400 pixels in each direction with 640±10nm band-pass emission filter.

the photoluminescence linewidth (Figure 4-6b) is sufficiently narrow to assume there is minimal heterogeneity in the photoluminescence properties of the nanocrystals. The measured FWHM of 78 meV is well within the range of single NC linewidths reported by an extensive study by Cui *et al.*[100] Furthermore, ensemble nanocrystal heterogeneity is likely not a concern in these measurements, as demonstrated by the raster scans taken of the sample both with and without a bandpass filter (Figure 4-7). The similarity in the scans confirms that the spectral filters act equivalently on each nanocrystal studied. If there were extensive heterogeneity in the single nanocrystal PL spectrum, the bandpass filter would dramatically alter the observed fluorescence intensity from each NC. Basic sample characterization is done through steady-state absorption and photoluminescence (Figure 4-6b), and a solution-averaged biexciton quantum yield measurement which demonstrate that our sample has a strong excitonic absorption feature characteristic of CdSe NCs and a relatively high ensemble-averaged biexciton quantum yield of 37%.

Single NC properties were also extensively characterized. Figure 4-6c depicts a representative snapshot of a nanocrystal blinking trace at both early and late times in a many hour fluorescence experiment, with a histogram of the whole trajectory (black) showing a number of distinct states, and a sharp, shot noise-limited 'off' state at the lowest intensity. Since the

intermediate states have different lifetimes than that of the highest intensity state (Figure 4-6d), either charging, trapping, or both are resulting in our observed blinking dynamics. Therefore, this study is confined only to the highest intensity emission state, which decays with a monoexponential lifetime and is likely a purely radiative state. Due to the complex core-shell heterostructure, it was necessary to experimentally determine an absorption cross section for the sample utilizing the photoluminescence lifetime (Figure 4-8). The single nanocrystal biexciton quantum yield is generally well within the expected bounds based on the solution-averaged biexciton quantum yield for all NCs studied. Figure 4-6e depicts a typical single-particle $g^{(2)}$ trace which has a biexciton to exciton quantum yield of 23%. Characterization of the scaling rate of the
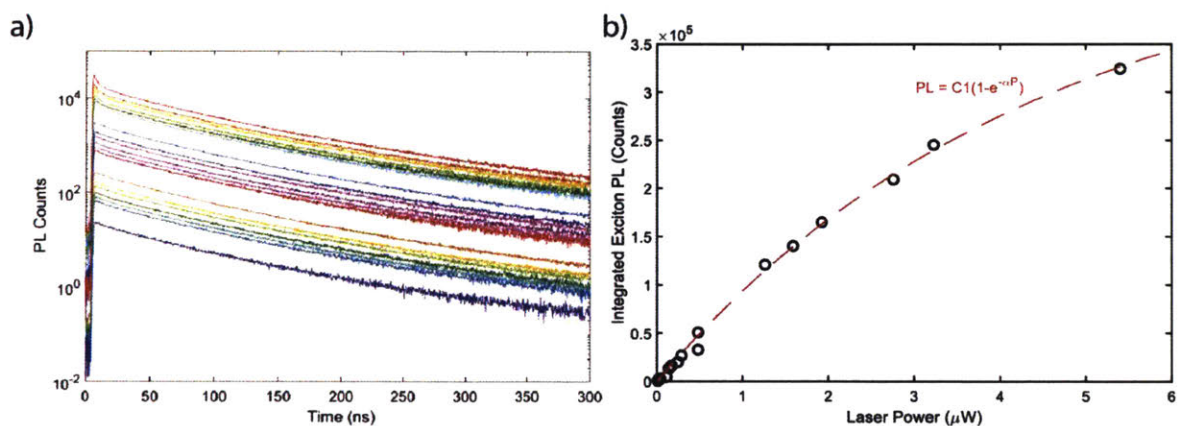
Figure 4-8 a) Power dependent ensemble PL lifetimes taken using calibrated discrete ND filters. b) Integrated area from 150 to 200 ns plotted against the incident laser power and fit to the equation in red to extract the absorption cross-section parameter (α).

a)

Triexciton   Triexciton

Biexciton   Hot Biexciton

b)

c)
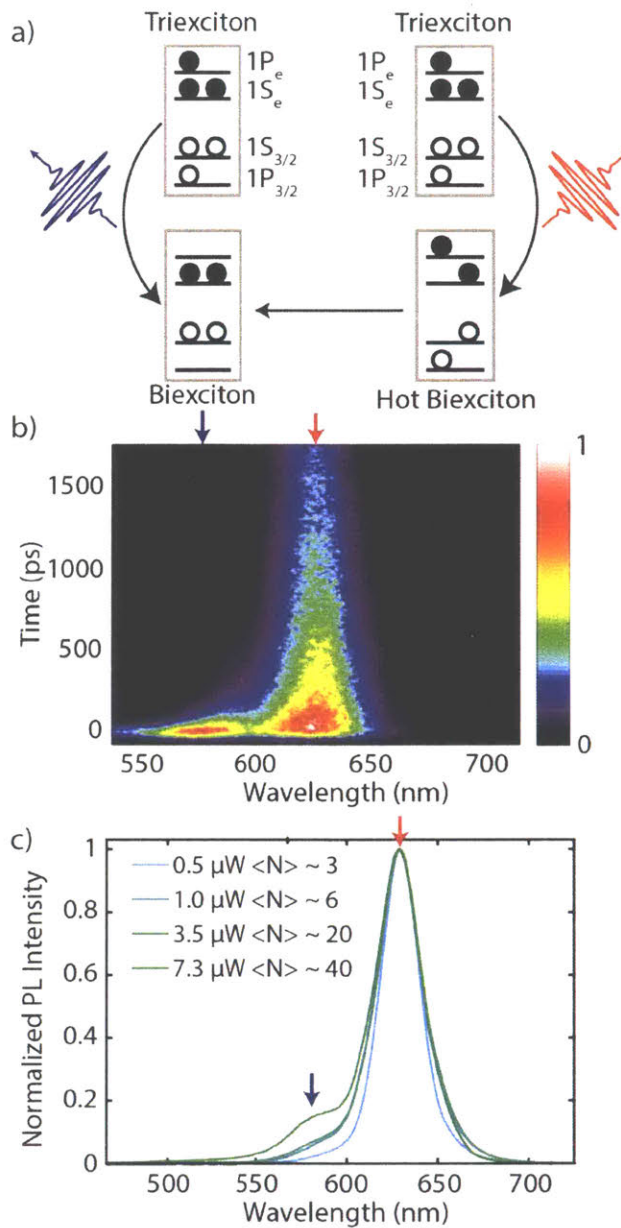
Figure 4-9 a) Schematic of the two possible triexciton emission pathways. b) Time- and spectrally resolved PL data excited at high-flux ($<n>$ = 40). c) PL spectrum at early time after excitation for a series of excitation fluxes.

biexciton emission as compared to the radiative exciton lifetime demonstrates that, in all cases, it

is consistent with the universal statistical scaling factor of four as described by our earlier study.

To accurately sort for emission which originates from the band-edge S-like state as

compared to the higher-lying P-like state, power-dependent streak camera measurements were

performed. Separating emission both spectrally and temporally was necessary to observe emission

from both states, even with high-flux excitation. The higher-lying P-like state is occupied by multiexciton states higher than the biexciton. Figure 4-9a illustrates schematically the states and pathways of interest. At high excitation fluences two emission peaks are observed which decay with different dynamics (Figure 4-9b). The blue shifted peak at 584 nm emits rapidly, on the order of the instrument response. It is important to note that emission in this case does not correspond to the triexciton states exclusively, but rather a Poissonian distribution of multiexciton states centered around an average excitation rate of ~40 excitons per nanocrystal. Thus, based on a broad distribution of states, these decay dynamics consist of many different multiexciton states and varied Auger rates. Furthermore, the percent of total emission contained within the P-state is quite small, which is why it is not detectable above the tail of band edge emission in a steady state measurement. Figure 4-9c shows the development of P-state emission at increasing excitation fluences.

Expanding upon the correlation measurement demonstrated by Fisher *et al.*, the branching ratio between S-state and P-state emission for the triexciton is measured through a spectrally-resolved third order correlation measurement.[94] The detector geometry is shown in Figure 4-10a. Four single photon counting detectors are used, each of which receives a quarter of the emission from a single nanocrystal. Three of the detectors have bandpass 640±10 nm filters which pass only
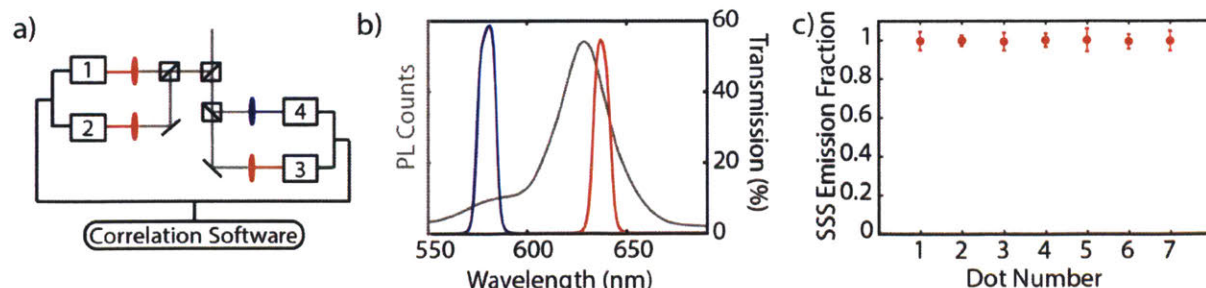
Figure 4-10 a) Schematic of the spectrally filtered thrid-order correlation measurement detector geometry. b) Early-time, high-flux photoluminescence spectrum showing S-state and P-state emission as well as the percent transmission for the two types of bandpass filter used. c) Fraction of triexciton events which emit through the SSS pathway for a number of different NCs.

73

S-state emission, and one detector has a bandpass 580±10 nm filter which passes predominantly P-state emission (Figure 4-10b). The absolute number of triexciton detection events is defined as detecting three photons after a single laser pulse. Triexciton detection events can occur either with all three photons arriving on the S-state detectors or with the first photon arriving on the P-state detector and the subsequent two photons arriving on S-state detectors. The second and third photons should always emit from the S-state as shown in the previous work by Fisher *et al.* and through lifetime measurements presented earlier in this section.[54,94] The relative detected counts are normalized based on the differential transmission probabilities of the S-state and P-state filters through fitting the PL trace in Figure 4-10b to two Gaussians and comparing the area when multiplied by the filter transmission spectrum with the full Gaussian. The extracted correction factors are 17.9% and 10.4% for the S-state and P-state filters respectively. The largest source of background for the measurement is the detection of two photons emitted from the biexciton state and one photon from the substrate as a three photon event. These counts are also subtracted from the raw measured three-photon correlation events to isolate true triexciton emission.

Figure 4-10c depicts the percent of total triexciton emission events which originate from the S-state and P-state for a number of nanocrystals. For every nanocrystal studied that had sufficient signal-to-noise, emission occurred almost exclusively from the S-state. Lifetime measurements presented above had indicated that as much as 20% of triexciton emission could be expected to arise from the P-state. This discrepancy suggests that simple predictions based on Fermi's Golden Rule likely underestimate the true P-state lifetime, and thus overestimate the P-state contribution to triexciton emission.
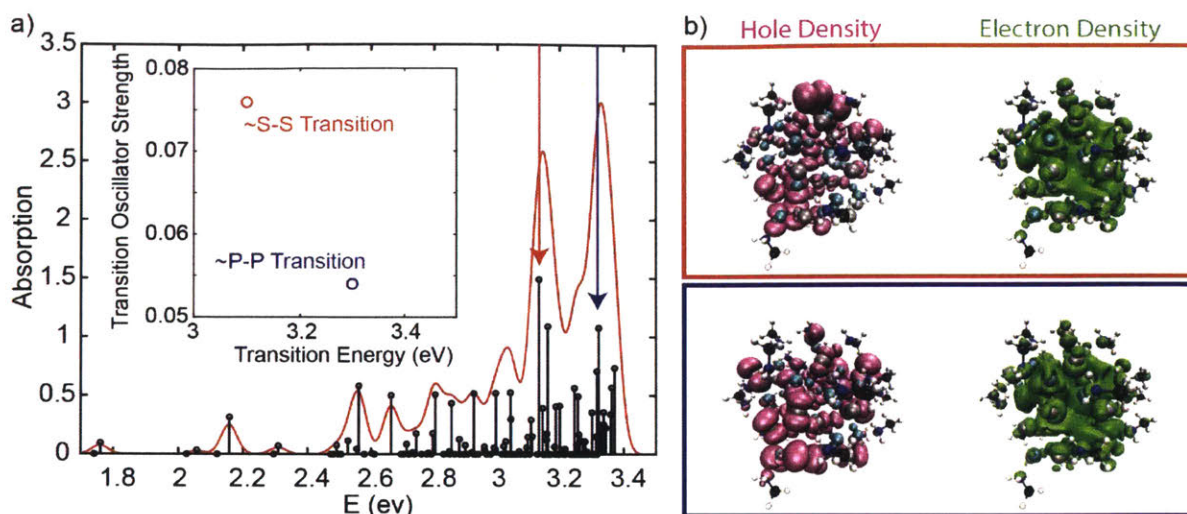
Figure 4-11 a) The black markers represent identified transitions with the height corresponding to the oscillator strength of the transition. The red trace is the sum of the oscillator strength-weighted transitions each with a fixed Gaussian linewidth to approximate an absorption cross section. The inset depicts the relative energy and oscillator strength of the two lowest energy bulk transitions. b) The attach and detach densities for the electron and hole states of the two transitions identified in the inset of a).

To confirm these experimental predictions, a computational study of a 1.4 nm diameter Cd38Se38 quantum dot was performed. All calculations were performed using DFT with a PBE0 functional and LANL2DZ basis set and effective core potentials using the QChem software package. The PBE0 functional was chosen because it is a hybrid functional, and incorporates some exact exchange, allowing for better treatment of the electron-hole interaction. The initial geometry was carved from bulk CdSe with the wurtzite structure, and methylamine ligands were attached to all 24 surface cadmium atoms. The geometry was then optimized at the PBE0/LANL2DZ level of theory.

After structural optimization, a time dependent density functional theory (TDDFT) calculation was performed. Figure 4-11a plots the relative energy and oscillator strength of each identified transition (black). Most of the states identified correspond to highly localized surface states, which is not unexpected due to the small NC size and relative high number of surface atoms. Adding together oscillator strength-weighted transitions with a fixed Gaussian linewidth

approximates an absorption spectrum of the 1.4 nm nanocrystal (Figure 4-11a, red). The two brightest excitations are bulk excitations at 3.13 eV and 3.32 eV, corresponding to a splitting of 190 meV. These excitations have oscillator strengths of 0.0757 and 0.0540, respectively (Figure 4-11a, inset). The 3.13 eV excitation is attributed to the $1S_e$-$1S_{3/2}$ transition, and the 3.32 eV state to the $1P_e$-$1P_{3/2}$ transition, noting that these are single exciton calculations, and thus do not account for exciton-exciton interactions or level repulsion as described by Franceschetti et al.[78] Figure 4-11b shows the attach/detach densities of the two brightest states. The attach density can be interpreted as an excited electron density, and the detach density can be interpreted as an excited hole density. The plotted densities show that both excitations are on the bulk of the quantum dot. Qualitatively, the detach density is located primarily on the selenium atoms in P-like atomic orbitals, consistent with LCAO arguments outlined in the introduction to this chapter. The attach density, however, is delocalized over both cadmium and selenium atoms in a spherically symmetric manner. The bulk-like nature of the excitations calculated, and the consistency in carrier density distribution with established theories give confidence to the calculated oscillator strengths, which suggest that the P-state emits more slowly than the S-state in a core-only material with a single exciton in either state.
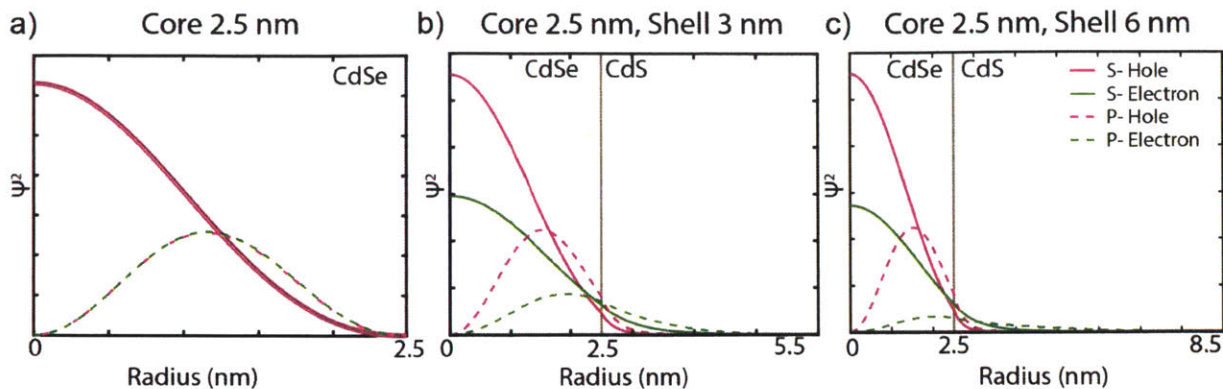
Figure 4-12 S-state (solid) and P-state (dashed) electron (green) and hole (magenta) wavefunctions for three different NC structures calculated using an extended particle in a sphere model.

Since TDDFT studies could only be conducted on relatively small core-only samples, relative lifetime predictions for larger core-shell particles are calculated using an extended particle in a sphere model presented by Haus *et al.* and utilized by Klimov *et al.*[101,102] These calculations are used to estimate the carrier wavefunctions of each state then calculate the electron and hole wavefunction overlap for the S-state and P-state. The radial distribution of the wavefunctions for a core-only (2.5 nm) and two core-shell (2.5 nm core, 3 and 6 nm shell) particles are presented in Figure 4-12. Qualitatively, increased delocalization into the shell is observed for the electron from both the S- and P-state into as shell thickness increases, decreasing electron-hole overlap. The degree of delocalization is much more significant for the P-state than the S-state. To obtain a quantitative measure of expected emission rate, we calculate electron-hole overlap integrals which are presented in Table 4-3.

Table 4-3 Calculated overlap integrals for the S-state and P-state wavefunctions presented in Figure 4-12.

	S-S Overlap	P-P Overlap
Core 2.5 nm	1	1
Core 2.5 nm Shell 3 nm	0.86	0.67
Core 2.5 nm Shell 6 nm	0.81	0.29

For the thickest shell size calculated (6 nm), the electron-hole overlap of the P-state decreases to less than 30%, while the S-state overlap remains above 80%. Based on the significant difference in electron-hole overlap for P-state excitons when changing CdS shell thickness, it is likely that shell thickness plays a significant role in the amount of triexciton emission that occurs from the P-state.

Similar to the TDDFT studies, these calculations are based on a single exciton occupying the state. It is likely that the presence of three excitons in the nanocrystal will result in increased delocalization of the P-electron into the shell due to Pauli repulsion. Thus, the radiative lifetime of the P-state is, if anything, underestimated by these methodologies, resulting in reduced emission from the state when in direct competition to the relatively fast S-state. The streak camera spectra are qualitatively consistent with this observation as well, requiring many excitons per nanocrystal on average to observe P-state emission.

4.4 Conclusion

This chapter details single NC analyses which unambiguously identify the dominant processes that control emission dynamics and efficiency from the biexciton and triexciton states in CdSe NCs. Biexciton emission is consistent with statistical scaling models and is unaffected by CdS shell thickness. Furthermore, there is no state memory, and successive photon emission events are entirely independent. The triexciton emits with dynamics consistent with band-edge recombination as the dominant emissive process. Through directly measuring the branching ratio between the S-state and P-state emission by single NC spectrally-resolved third-order correlation calculations, it is clear that triexciton emission in CdSe/CdS core-shell nanocrystals is dominated by band-edge emission. Both TDDFT modeling and extended particle in a sphere calculations qualitatively confirm the trend in P-state lifetime which explains the dominance of the band-edge

dynamics. The dominance of S-state emission justifies the similarity in the triexciton lifetime and quantum yield to the biexciton state as was previously reported, and provide an insight into the dominant mechanisms for higher order multiexciton emission.

4.5 Methods

Single NC measurements were all completed using the home-built confocal fluorescence microscope described in Chapter 2. The sample is excited by a picosecond pulsed excitation source (532 nm, Picoquant, LDH-P-F-A-530-B) and mounted to a three axis piezo stage (Physik Instrumente, P-517.3CL). Emission is collected using a 100x oil immersion objective (Nikon, NA 1.25). Excitation and emission are separated using a 535 nm long pass filter (Chroma Technology Corp, ZT532rdc-3). Emission is spatially (1:1 telescoping 50 μm pinhole) and spectrally (532 nm notch, Chroma Technology Corp, ZET532NF) filtered before being directed through three 50:50 beamsplitters (Thor Labs) in the manner described in Chapter 2, creating four separate beams with equivalent intensity. These are individually focused onto one of four single photon counting detectors (SPCM-AQR-13, Perkin Elmer) with a 10 cm achromatic lens (Thor Labs). All mirrors in the detection arm of the microscope are cold mirrors (Thor Labs, M254C45, transmits >700 nm, reflects 400-700 nm) to suppress detector cross talk originating from emission of a NIR photon from the silicon detector. Spectral filtering for correlation measurements is done using 580±10 nm and 640±10 nm bandpass filters (Thorlabs). Photon records are created using a HydraHarp (Picoquant, HydraHarp 400). All post-processing is done using home-built software (https://github.com/tsbischof/picoquant, https://github.com/tsbischof/photon_correlation, and https://github.com/hutzat/photons).

For streak camera measurements, the sample was excited by the 404nm frequency-doubled output of a Ti:Sapph oscillator (Coherent, Mira 900-F) and the emission was collected and directed

into a spectrometer (Bruker Chromex, 250is) to resolve the spectra, which was measured on a streak camera (Hamamatsu, C5860).

5 Chapter

Multiexcitons in Perovskite Nanocrystals

Contributions: The nanocrystal samples studied in this section were synthesized by M. Nasilowski, O. B. Achorn, F. Krieg, and A. Swarnkar from the Bawendi and Kovalenko research groups. Bulk films were synthesized by S. Ha from the Tisdale research group. The data was collected and analyzed by K. E. Shulenberger, M. N. Ashner, N. D. Klein, and H. Utzat. Analysis was performed utilizing software developed by T. S. Bischof, K. E. Shulenberger, and H. Utzat. The results presented here are adapted from Shulenberger and Ashner et al (Submitted)., Ashner and Shulenberger et al. (In Preparation), and Shulenberger et al. (In Preparation).

Lead halide perovskites are one of the most promising emerging materials systems for a number of optoelectronic applications. Of particular note, lead halide perovskite solar cells have shown one of the steepest improvements of any novel photovoltaic material monitored by the National Renewable Energy Laboratory (NREL), with a recently reported certified 23.7% power conversion efficiency.[103] The outstanding performance of these devices can be attributed to a number of intrinsic materials properties, including high defect tolerance,[104–106] and long carrier diffusion lengths.[107–109]

The development of $CsPbX_3$ (X= Cl, Br, or I) perovskite nanocrystals (NCs) has expanded the range of applications available to lead halide perovskites.[9] Due to spatial and quantum confinement, perovskite nanomaterials are strongly fluorescent with photoluminescence (PL) quantum yields close to unity.[9,110] Of particular technological interest is the potential use of $CsPbX_3$ nanocrystals as the emissive medium in lighting[111–116] and lasing[117,118] applications.

5.1 Background

Recent studies have begun to investigate the biexciton binding energy and other multiexciton properties in perovskite NCs and in particular in $CsPbBr_3$ perovskite nanocrystals utilizing a broad range of methods.[119–122] Time-resolved, spectrally-resolved photoluminescence studies of $CsPbBr_3$ and $CsPbI_3$ report exceptionally high biexciton binding energies of up to 100 meV due to the appearance of a red-shifted emission feature during high-flux excitation.[120] Transient absorption studies ascribe an induced absorption feature on the red edge of the primary ground state bleach to biexciton absorption, and extract values ranging from 30-70 meV in $CsPbI_3$.[119] However, the presence of a strongly bound biexciton implies properties that conflict with indirect measurements and observations of charge carrier interactions in these materials. One such characteristic is the exciton binding energy, which is estimated to be ~40 meV in $CsPbBr_3$ nanocrystals based on effective mass approximations [123] – slightly larger than the value of ≤ 12 meV in bulk lead halide perovskites.[124,125] It is unintuitive that confinement effects would result in a neutral-neutral interaction (exciton-exciton) that is a factor of two to three more attractive than the positive-negative interaction of an electron and hole. Similarly, examination of the optical gain threshold using transient absorption spectroscopy shows a constant carrier density gain threshold rather than a constant number of excitons per nanocrystal as is observed in traditional II-VI nanocrystal materials.[126] A constant carrier density threshold is indicative of weakly bound carriers, rather than strongly bound correlated exciton states. If multiexciton states determine the lasing transition, the density of carriers needed to observe gain should scale with the volume of the nanocrystal.

The single nanocrystal properties of cesium lead halide perovskite NCs have also generated extensive interest.[127–132] Like other semiconductor NCs, perovskites exhibit fluorescence

intermittency.[128,133] Studies have identified multiple mechanisms for blinking, and it seems to vary depending on the exact sample preparation which mechanism dominates. Single molecule biexciton quantum yield measurements have indicated that most perovskite NC systems have low biexciton quantum yields at room temperature.[133] However, these measurements have generally been low signal-to-noise due to the fluorescence intermittency of the NC. Solution phase biexciton quantum yield measurements indicated a composition and size dependent trend in biexciton quantum yield, suggesting some materials may have exceptionally high biexciton quantum yield values, particularly for a core only material.[11] As was discussed in the previous chapter, extensive material engineering was necessary before CdSe NCs achieved such high biexciton quantum yields.[83] Thus there remains a few open questions: Why are the single molecule and solution phase quantum yield values so different and what material property enables high biexciton quantum yields for a core-only material? The following sections set out to investigate these disparate reports in the literature to uncover a cohesive and self-consistent understanding of biexciton properties in $CsPbBr_3$ perovskite NCs.

5.2 Ensemble Photoluminescence

To reconcile conflicting reports of biexciton binding energy, this study investigates the origin of the red-shifted photoluminescence feature that is observed under high-flux excitation in cesium
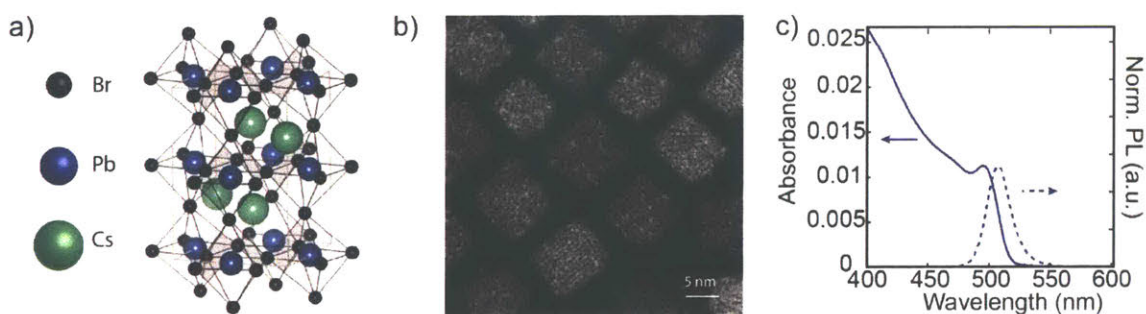
Figure 5-1 a) $CsPbBr_3$ orthorhombic perovskite crystal structure model b) Representative HAADF-STEM image of 7.5 nm NCs c) Steady-state absorption and photoluminescence spectra of 7.5 nm NCs

lead halide perovskite NCs and which has been reported in recent works as biexciton emission.[120] In order to look at this, $CsPbBr_3$ nanocrystals were used with 7.5±1 nm edge lengths and zwitterionic capping ligands, as synthesized according to Krieg, *et al.*[110] The perovskite crystal lattice is shown in Figure 5-1a and a representative high-angle annular dark field scanning transmission electron microscopy (HAADF-STEM) image is shown in Figure 5-1b. Nanocrystal size was calculated by measuring the edge length of 71 nanocrystals from TEM images and is consistent with previous reports correlating emission wavelength with nanocrystal size.[9] Steady-state absorption and photoluminescence spectra are shown in Figure 5-1c. The biexciton to exciton quantum yield ratio measured by a solution-$g^{(2)}$ technique is 11±3%.[55] As discussed in Chapter 3, the solution biexciton quantum yield measurement was separated into small portions to avoid intensity drift effects due to nanocrystal deposition on the walls of the microcapillary over the course of the experiment..

To look at the change in spectra and dynamics with varying excitation flux, time- and spectrally-resolved photoluminescence measurements were used to measure the decay kinetics. Samples were stored and prepared under nitrogen and fully encapsulated throughout the duration of the measurements. Under low-flux excitation a single peak is observed with similar decay kinetics across all spectral positions (Figure 5-2a).
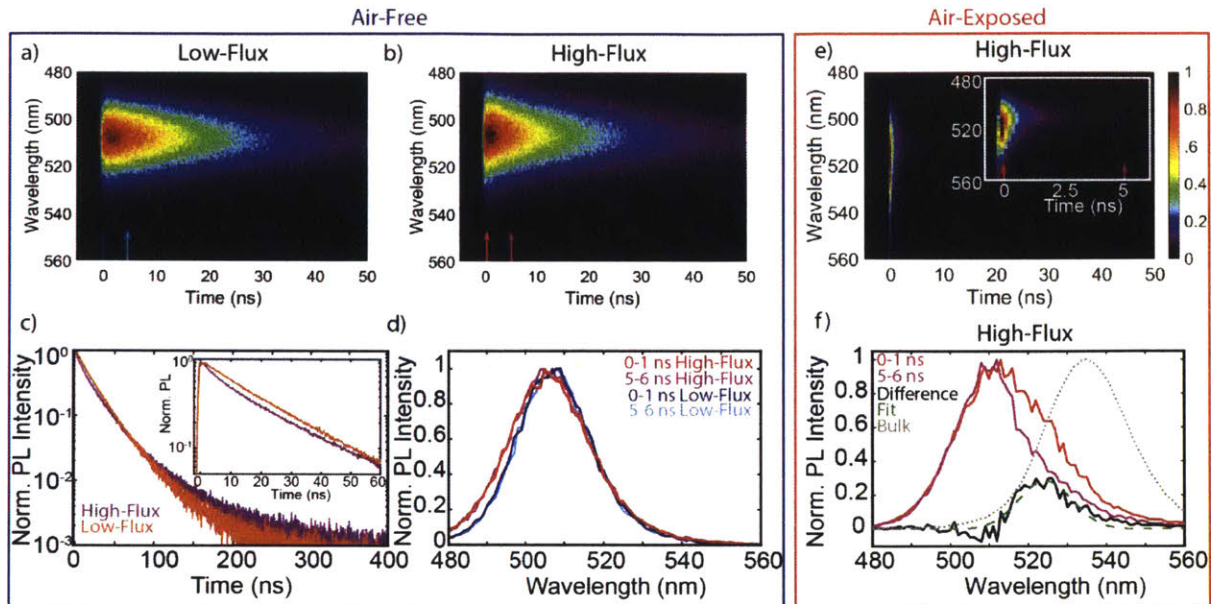
Figure 5-2 a) Low-flux (5 µJcm^{-2}) time-resolved emission spectrum of 7.5 nm NCs excited at 400 nm. b) High-flux (5 mJcm^{-2}) time-resolved emission spectrum of 7.5 nm NCs excited at 400 nm. c) Spectrally integrated high (purple)- and low (orange)-flux PL dynamics showing lifetime quenching at early times corresponding to multiexciton emission. The inset shows the early time dynamics emphasizing the accelerated emission rate at early time. d) Comparison of spectral slices corresponding to high-flux early (0-1 ns) time (blue), high-flux late (5-6 ns) time (cyan), low-flux early (0-1 ns) time (red), and low-flux late (5-6 ns) time (magenta). The spectral positions are labeled with arrows in a and b. e) High-flux time-resolved spectrum of 7.5 nm NCs exposed to air with the inset showing early time spectra. f) Spectral slices of an air-exposed, high-flux sample corresponding to 0-1 ns (red) and 5-6 ns (magenta) as labeled in the inset of e. The difference between the red and magenta traces is in black. The green dashed trace is a single Gaussian fit to the difference spectrum. A bulk CsPbBr$_3$ perovskite emission spectrum is plotted in dotted grey for reference.

Next, the NC emission spectrum under low-flux excitation (20 µJcm^{-2}) is compared to the emission spectrum under high-flux excitation (20 mJcm^{-2}). At low-flux, emission is almost exclusively from the exciton state, while multiexciton emission contributes more to the high-flux spectrum. Due to the non-Gaussian beam profile, the ratio of excitons to higher order multiexcitons over the whole laser spot is a more representative criterion for the low-flux and high-flux regimes, instead of just average power. Assuming Poissonian absorption statistics and previously determined absorption cross sections[134] for the NCs with no absorption saturation, the average exciton to multiexciton ratio is ~5:1 for the low-flux measurement and predominantly multiexcitons for the high-flux measurement. Given the measured biexciton quantum yield of 10%, the average biexciton lifetime of ≤500 ps, the >10 ns low-flux exciton lifetime, and an
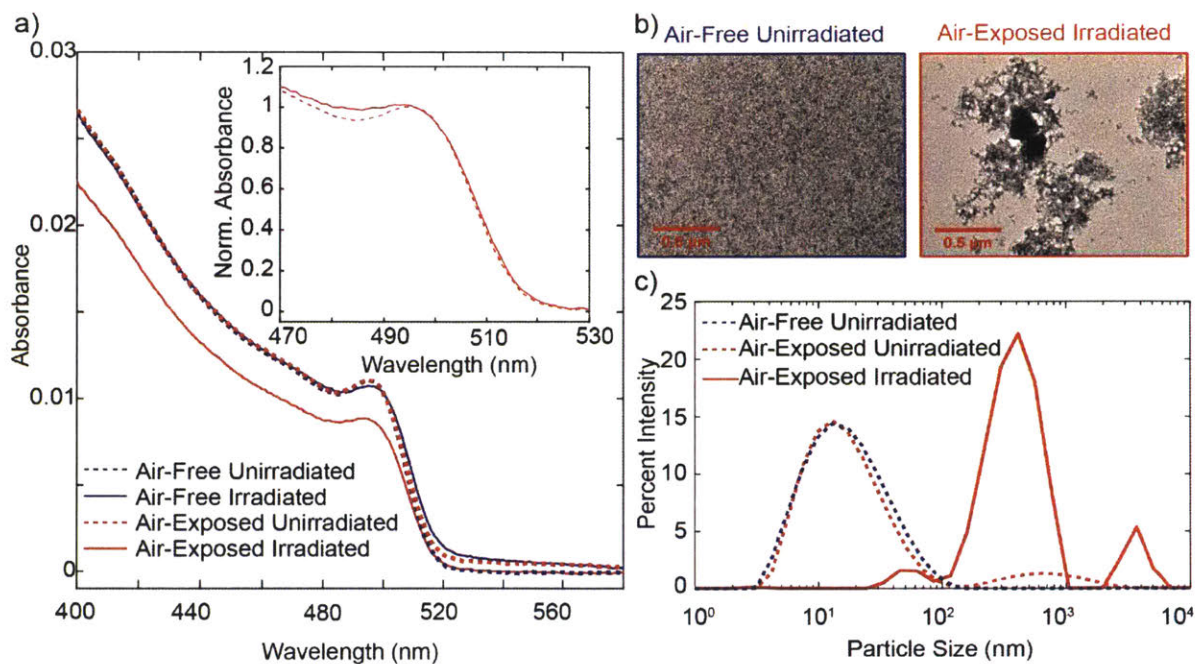
Figure 5-3 a) Steady-state absorption spectra of 7.5 nm NC samples before (dotted) and after (solid) irradiation for both an air-free (blue) and air-exposed (red) sample. The inset shows the normalized change in the excitonic peak for the air exposed sample. b) Representative TEM images for air-free, unirradiated (blue) and air-exposed, irradiated (red) samples. c) Dynamic light scattering data size distribution fits for air-free, unirradiated (blue dotted), air-exposed, unirradiated (red dotted), and air-exposed, irradiated (red solid) samples.

average excitation rate of one exciton per NC, biexciton emission ought to contribute ~50% to the emission collected during the first nanosecond after excitation. However, no signature of red-shifted emission is observed under high-flux excitation (Figure 5-2b and d). At 5 nanoseconds following excitation, the only observable difference between the low-flux and high-flux spectra is a slight broadening on the blue edge. This broadening is constant in time though, and thus not due to multiexciton emission. The apparent broadening on the blue edge for high-flux measurements is likely a reduction in re-absorption from the band-edge due to excitons occupying the state from the high-flux excitation. Looking at the PL lifetime however, reveals an additional rapid decay component consistent with multiexciton emission (Figure 5-2c). Therefore, the intrinsic biexciton emission spectrum is largely overlapped with the exciton emission spectrum. Red-shifted spectral

features that were previously observed must be due to extrinsic factors, rather than resulting from multiexciton emission from the nanocrystal sample.

When the samples are exposed samples to air and then excited under the same high-flux conditions, a red-shifted emission feature emerges (Figure 5-2e). A large decrease in the PL intensity also corresponds to the appearance of this feature. Furthermore, the spectrally integrated PL dynamics of the air-exposed sample under high-flux irradiation are drastically different from those of the air-free sample, with a rapid early component that is dominated by emission from the red edge of the spectrum. Figure 5-2f compares spectral slices at early times (0-1 ns) and late times (5-6 ns) for an air-exposed sample under high-flux excitation. This red-shifted feature can be isolated by directly subtracting the normalized late time spectrum (magenta) from the normalized early time spectrum (red) and fitting the difference (black) to a single Gaussian (green). The fitted
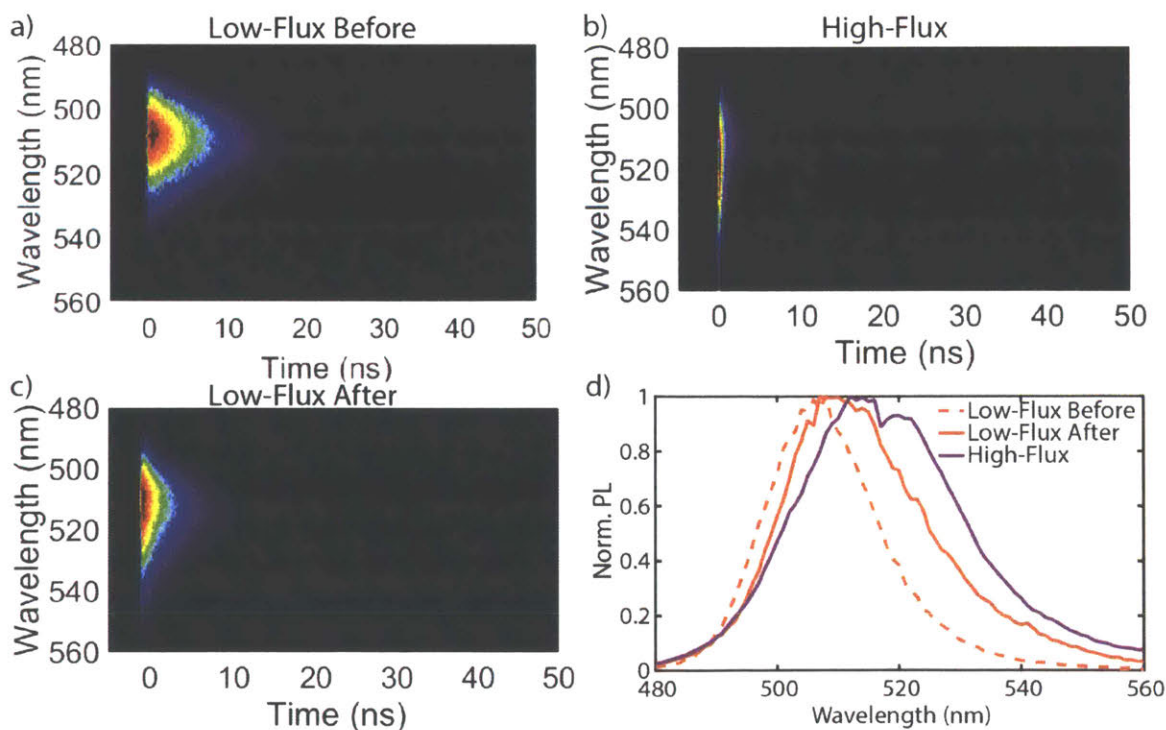
Figure 5-4 . a) Low-flux time-resolved PL spectrum of air-exposed 7.5 nm NC. b) High-flux time-resolved PL spectrum of the same air-exposed sample. c) Low-flux time-resolved PL spectrum taken immediately following the measurement in part b. d) 0-1 nanosecond spectral slices of the measurements shown in a (orange dashed), b (purple solid), and c (orange solid).

red-shifted feature is centered at 523 nm. A film of polycrystalline bulk $CsPbBr_3$ was synthesized

via reprecipitation and the emission spectrum of this sample is plotted for reference (grey). Due to

the film thickness, the measured PL spectrum of the bulk sample is likely red-shifted from the true

PL spectrum due to reabsorption effects. There is also a substantial difference in the low-flux

emission spectrum before and after high-flux irradiation of an air-exposed sample (Figure 5-4).

Because the observed shift in the emission spectrum is permanent and is similar to bulk-like

emission, high-flux ensemble PL changes are likely due to photoluminescence from large bulk-

like particles which form from sample aggregation due to exposure to air as well as subsequent

optically-induced sintering. Perovskite nanocrystal sintering has been previously observed in both

cubic nanocrystals and 2-D nanoplatelets.[135–137]

To test this hypothesis, post-irradiation analyses were conducted including steady state

absorption, TEM, and particle sizing by dynamic light scattering (DLS). Absorption measurements

before and after high-flux irradiation for an air-free and air-exposed sample are shown in Figure

5-3a. A slight red shift of the main absorption feature, a significant broadening of that peak, as

well as reduced overall absorption are observed. These changes are consistent with the growth of

a population of larger nanocrystals, which increases the heterogeneous broadening and red-shifts
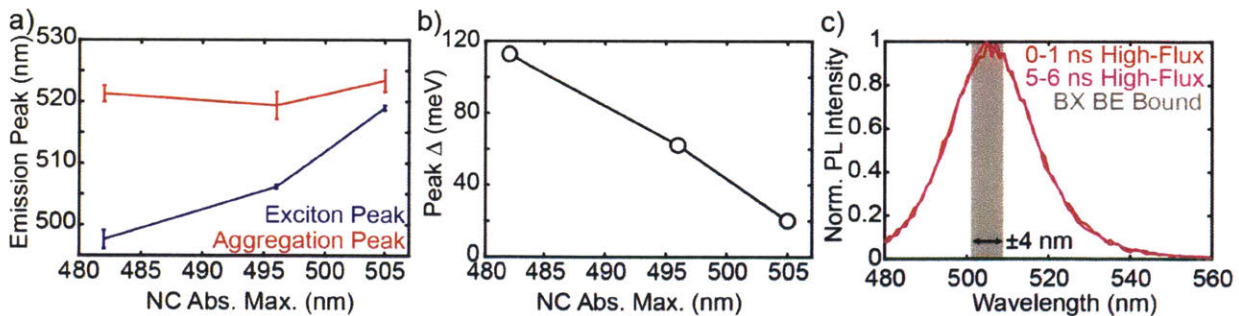
Figure 5-5 a) Exciton emission maxima extracted from air-free low-flux emission spectra and aggregation emission maxima extracted from air-exposed high-flux early-time spectra (demonstrated in Figure 2f) for three nanocrystal sizes. b) Size dependent difference between the exciton and aggregate emission features shown in a. c) Early- and late-time air-free high-flux emission spectra showing no time-dependent emission shift corresponding to multiexciton emission. The grey shaded region corresponds to our certainty in the emission maximum based on the instrument spectral resolution, corresponding to the biexciton binding energy range.

the absorption maximum. The precipitation of larger aggregates reduces the total optical density of the solution.
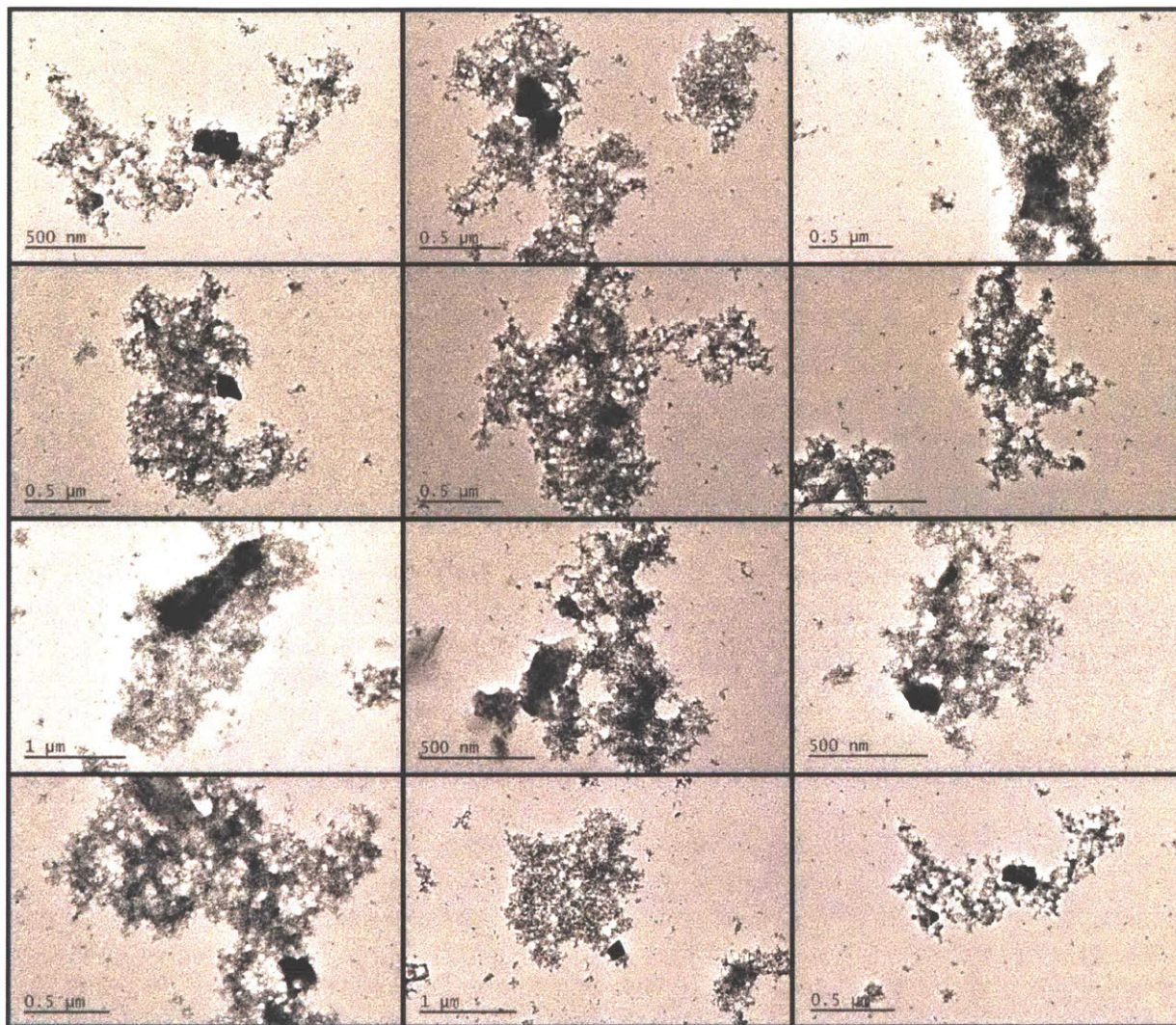
Figure 5-6 Additional TEM images of the air-exposed, irradiated NC sample.
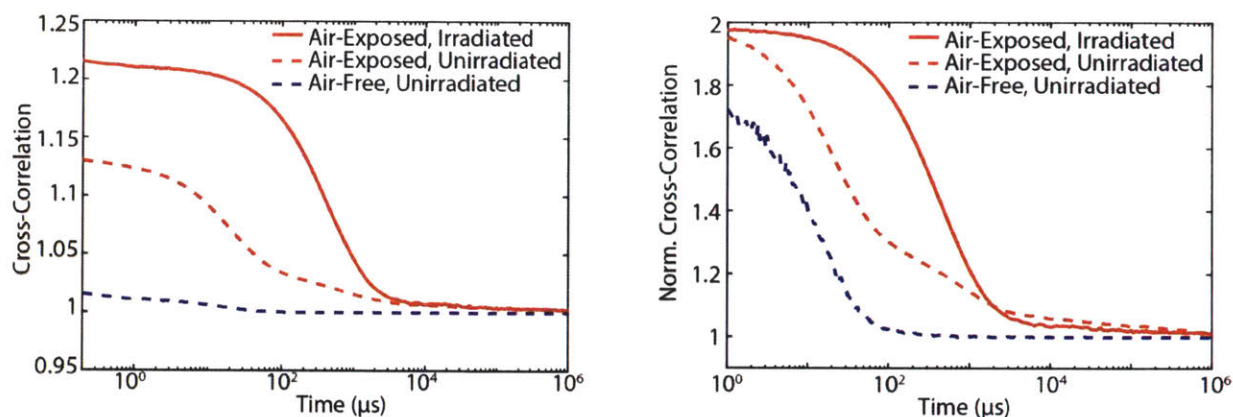
Figure 5-7 Raw DLS curves which were used to generate the size distributions shown in Figure 5-3.

TEM images of the samples with and without air before and after irradiation show the appearance of large bulk-like aggregates which are hundreds of nanometers in size, and do not appear in pre-irradiation or air-free samples (Figure 5-3b). Figure 5-6 presents more images to further support that this behavior is occurring in the irradiated samples measured. Finally, DLS measurements of pre- and post-irradiation samples with and without air show a significant change in the size distribution of the particles within the sample (Figure 5-3c). For air-free, unirradiated samples, the majority of the sample has a solvodynamic radius which is centered around 15-20 nm, consistent with an un-aggregated nanocrystal population. Irradiation of an air-free sample results in the emergence of a small feature corresponding to large aggregates, but the predominant species is still a nanocrystal population. Upon exposure to air and high-flux irradiation, almost the entirety of the nanocrystal signal disappears, and heterogeneous particles larger than one micron in size are observed in solution. Thus, the red-shifted emission observed in PL experiments can be accounted for by the appearance of large, bulk-like structures, and not by multiexciton emission.

Returning to consideration of the biexciton binding energy, emission from a bulk-like population reproduces the previously reported red emission that had been attributed to the biexciton. Figure 5-5a demonstrates how comparing the size-dependent excitonic emission peak

90

with the static bulk-like peak imitates a large, size-dependent biexciton binding energy. Figure 5-5b demonstrates the difference between the nanocrystal and aggregate feature as a function of nanocrystal size, with values ranging from a few tens of meV to nearly 120 meV for highly confined NC samples. Maintaining truly air-free samples is thus crucial to accurately characterize multiexciton behavior when using high-flux ensemble techniques. As for the true biexciton spectrum, no appreciable change in the total photoluminescence spectrum at early times is observed under high-flux irradiation of an air-free sample. Therefore, the biexciton spectrum must be within the spectral envelope of exciton emission. Calculations described above predict that the emission spectrum over the first nanosecond will contain ~50% biexciton emission for the sample studied here. Thus, the biexciton binding energy cannot be more than ± 20 meV in 7.5 nm $CsPbBr_3$ nanocrystals based on the spectral resolution of our instrument. A weakly bound biexciton state is consistent with the low exciton binding energy observed in bulk perovskite materials, and the constant carrier density gain threshold reported by Geiregat, et al.[126] Since there is a high degree of exciton-phonon coupling and significant dielectric screening in the perovskite lattice,[138–140] shielding of charges is likely to result in even smaller multiexciton binding energies than in traditional, more rigid nanocrystal materials such as CdSe.[51,93,141]

5.3 Transient Absorption Measurement of the Biexciton Spectrum

To experimentally probe biexciton states in perovskite NCs, fluence-dependent TA spectroscopy in combination with a data-driven method for retrieval of the exciton and biexciton component spectra was employed. By applying this method and comparing the separate exciton and biexciton spectra as a function of NC size, more thorough characterization of exciton-exciton interactions in perovskite materials is possible. The ensemble TA spectrum is a linear combination of component spectra associated with ground-state, singly-excited, and doubly-excited nanocrystals whose relative weights depend on the incident laser fluence in accordance with the Poisson statistics of

91

photon absorption. The full, multi-dimensional fluence-dependent data set is fit to a simple first-order kinetic model in which biexcitons decay into excitons while simultaneously solving for the underlying component spectra associated with each of these states. This approach is combined with a Markov chain Monte Carlo sampler to carefully examine the statistical certainty of the fits and verify the model assumptions.

The same colloidal $CsPbBr_3$ NCs with zwitterionic capping ligands synthesized by a hot-injection method as described by Krieg et al.[142] were used for TA measurements as for the previous section. Each sample contained cubic nanocrystals with an average size of 6 ± 1, 7.5 ± 1, and 10 ± 1 nm measured using electron microscopy. Figure 5-8a shows the size-dependent linear absorption and photoluminescence spectra of all three samples, and Figure 5-8b shows a representative high angle annular dark field scanning electron microscopy (HAADF-STEM) image of the 10 nm NCs. This size range spans the weak to intermediate confinement regimes in $CsPbBr_3$, as evidenced by
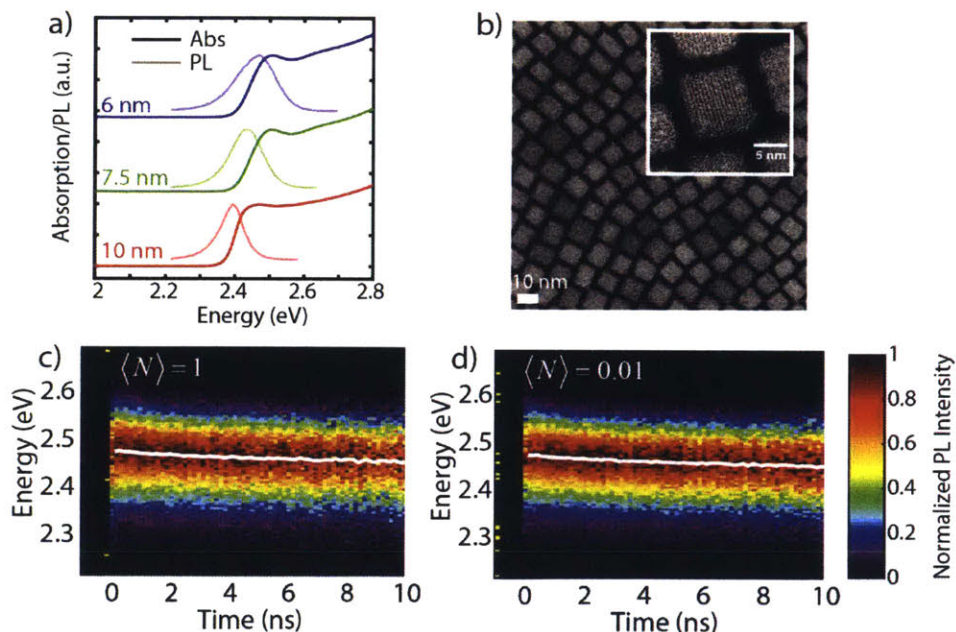
Figure 5-8 . (a) Linear absorption and photoluminescence spectra for the 3 samples studies. (b) HAADF-STEM of a film of 10 nm NCs and (inset) high resolution HAADF-STEM of a single NC. (c) Time-resolved photoluminescence spectrum of 6 nm NCs under high fluence excitation (26 $\mu J/cm^2$) normalized to constant peak intensity. White line indicates the peak position extracted from a gaussian fit. (d) Time-resolved photoluminescence spectrum of 6 nm NCs under low fluence excitation (0.26 $\mu J/cm^2$) normalized to constant peak intensity.

the increasing prominence of the excitonic feature in the linear absorption spectra with decreasing NC size.

Unlike the previous studies in this thesis, absorption studies are used here to interrogate the entire excited state rather than just the luminescent properties. As described in Chapter 2, TA is a pump-probe technique which measures the differential absorption of the ground state and excited state at various time delays. To extract more detailed information about the spectral difference between the exciton and biexciton state, fluence-dependent TA spectroscopy can be used to characterize the spectral properties of excited states in nanocrystals. In addition, the superior time resolution and signal-to-noise ratio allow for an accurate quantification of the biexciton dynamics. However, the complex lineshapes of TA spectra – especially when exciton and biexciton signatures are heavily overlapping – present a challenge to interpretation. To illustrate this, Figure 5-10 shows the TA spectral changes in 7.5 nm NCs that accompany various dynamic processes after photoexcitation. In this dataset, the pump pulse excited an average of 1.1 excitons per NC, which generates roughly equal proportions of excitons and biexcitons, assuming Poissonian absorption. As such, the biexciton and exciton states contribute roughly equally at early time delays while only the exciton contributes at late time delays after the biexcitons have decayed. The first 2 ps are dominated by hot carrier cooling and other ultrafast relaxation processes that are
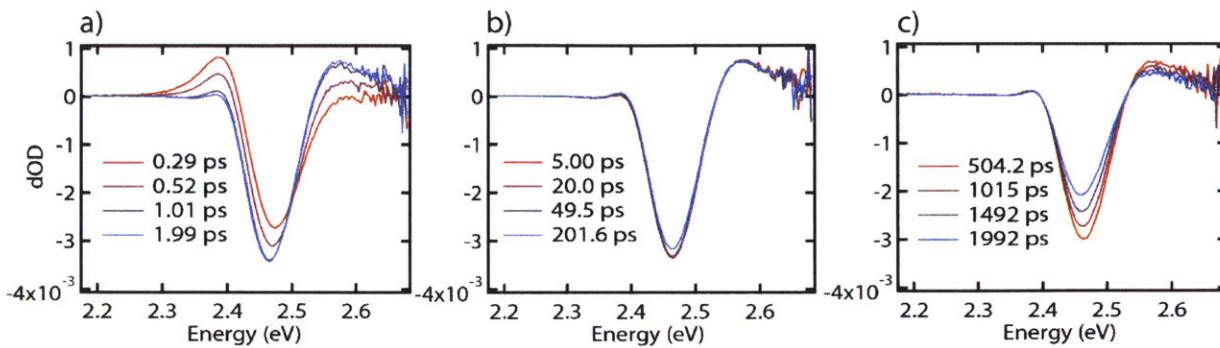
Figure 5-9 Transient absorption spectral dynamics of 7.5 nm NCs with a pump fluence that generates an average of 0.2 excitons per NC per pulse over the same pump-probe time delay regimes as Figure 5-10: a) 0-2 ps, b) 2-200 ps, and c) >200 ps.

difficult to characterize and result in dramatic changes in the spectral line shape (Figure 5-10a). Figure 5-10b shows the more subtle spectral changes that occur over the next 200 ps due to multiexciton relaxation after ultrafast hot carrier cooling is completed. We can attribute these changes to decay of the biexciton state because they do not occur under low-fluence excitation (Figure 5-9) Once the biexcitons decay, the spectral line shape remains largely unchanged and simply decays in intensity as excitons recombine (Figure 5-10c). The spectral dynamics shown in Figure 5-10b that correlate with the decay of biexcitons without interference from other ultrafast processes contain the most reliable spectral information on the biexciton state. Due to the subtle nature of these spectral changes and the almost complete overlap between the biexciton and exciton
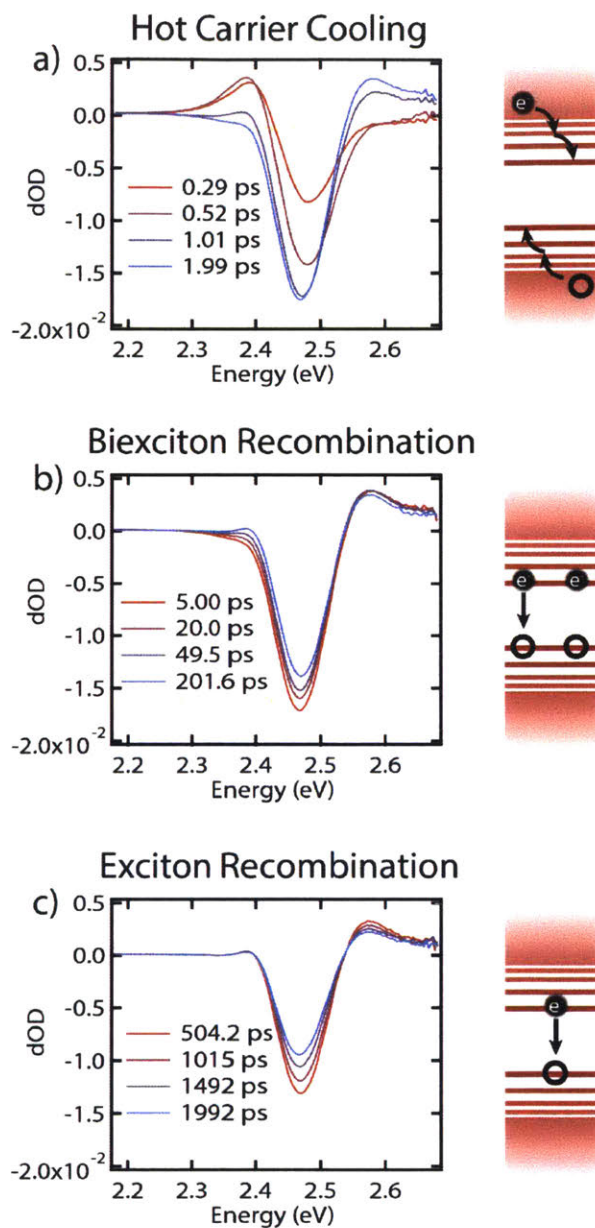
Figure 5-10 Transient absorption spectral dynamics of 7.5 nm NCs with a pump fluence that generates an average of 1.1 excitons per NC per pulse. The schematics illustrate the dominant physical processes during the pump-probe delay times of the corresponding spectra. (a) Hot carrier cooling and structural relaxation (0-2 ps). (b) Biexciton recombination (2-200 ps). (c) Exciton recombination (>200 ps).

spectra, spectral component analysis is required for complete interpretation. Furthermore, this procedure should not involve fitting the spectra to a predetermined mathematical function as the spectra have no clear functional form.

To extract the component spectra corresponding to exciton and biexciton states in perovskite NCs, the method of target analysis with a Markov chain Monte Carlo (MCMC) sampler is used, as described previously, in order to visualize and quantify the statistical uncertainty in the fitted kinetic parameters and spectra. This method is used to extract spectral information without constraining the data to fit an underlying spectral form, and such that a kinetic model can be utilized to also incorporate the information in the time-domain.[143] One major assumption employed is that the ensemble TA spectrum is a linear combination of fixed contributions from singly-excited NCs and doubly-excited NCs, called component spectra here, and that their relative initial populations depend on the laser excitation fluence through the Poisson statistics of photon absorption. To remove spectral contributions from initially excited hot carrier distributions, fitting is restricted to the 2.0-2500 ps time window.

A simple kinetic model (Equation (5-1)) is used as the basis for the target analysis fits, consisting of biexciton and exciton populations (BX and X, respectively) that decay in series with the decay time constants as two of the fit parameters (τ_{BX} and τ_X).

$$\frac{d[BX]}{dt} = -\frac{[BX]}{\tau_{BX}}$$

$$\frac{d[X]}{dt} = \frac{[BX]}{\tau_{BX}} - \frac{[X]}{\tau_X}$$

(5-1)

The justification of this model is based, in part, on the observation that the TA spectral shape at long pump-probe delays (>200 ps) does not depend on the initial excitation fluence. Since there is no fluence dependent change to the long time dynamics, trion formation is not a concern.

In order to robustly extract both the exciton and biexciton spectra, the entire fluence-dependent data set is fit simultaneously by initializing the populations of biexcitons and excitons using the Poisson distribution with an average number of excitons per nanocrystal calculated from the

applied pump power, J, and a single absorption cross-section parameter, α, as a third fit parameter: $[BX(t = 0)] = 1 - e^{-\alpha J}(\alpha J + 1)$ and $[X(t = 0)] = \alpha J e^{-\alpha J}$. Note that the initial biexciton population, as defined here, also includes the small (<1%) population of higher-order excitations to quantitatively account for all absorbed photons. Crucially, this initialization links the fluence-dependent changes in the spectral lineshapes with the Poisson statistics for photon absorption using a single parameter.

The Markov chain is used to determine statistics such as means, variances, and covariances for the kinetic model parameters and draw samples from it to visualize and accurately characterize uncertainties in the fits to the data and in the component spectra. Table 5-1 shows the extracted biexciton lifetime and the extracted cross-section parameters for all three sizes of NCs and their uncertainties. Table 5-1 also shows the absorption cross-section of each NC calculated from the model output and the experimental conditions. The fitted absorption cross-sections show the expected positive trend with NC size since absorption increases with NC volume and compare favorably to those reported in the literature, providing a key check for the model's accuracy. The biexciton lifetimes also increase with NC size as expected and match those extracted from fitting overall PL and TA dynamics in other studies.

Table 5-1 Median parameters recovered from the MCMC ensembles with the central 90% credible intervals indicated via the super- and sub-scripts, and the absorption cross-section at 400 nm calculated from the fit parameter and experimental conditions. Fits were performed over a time delay range of 2-2500 ps.

Parameter	10 nm	7.5 nm	6 nm
τ_{BX} (ps)	$205.2^{205.5}_{204.9}$	$56.71^{56.77}_{56.65}$	$35.77^{35.85}_{35.70}$
α (μW^{-1})	$0.01222^{0.01224}_{0.01220}$	$0.005836^{0.005839}_{0.005833}$	$0.004706^{0.004711}_{0.004702}$
Cross-section per NC (cm^2)	6.493×10^{-14}	3.108×10^{-14}	2.505×10^{-14}

The most informative output of the model are the component spectra comprised of all the transitions available to the exciton and biexciton states. Figure 5-11displays the biexciton and exciton component spectra for all three NC sizes, normalized to have the same maximum absolute bleach intensity. These plots are generated from 100 random samples from the MCMC ensemble overlaid, though the spread in the 100 MCMC samples is significantly smaller than the line thickness as rendered for readability. This indicates a high certainty in the shape of the best fit spectra for the proposed model. Plots of the raw component spectra generated in the same fashion show that the same is true for their intensities. Rigorously, the "biexciton" component spectra shown in Figure 5-11 represent the transient absorption spectrum of each sub-ensemble of doubly-excited CsPbBr$_3$ NCs, which includes contributions from exciton-to-biexciton transitions and biexciton-to-triexciton transitions. Nonetheless, comparison of the exciton and biexciton component spectra suggest general conclusions about exciton-exciton interactions in perovskite nanocrystals.

The biexciton spectra are consistently broader in linewidth and the bleach peak is slightly blue-shifted from the exciton peak. This suggests that the exciton-exciton interaction is very weak or slightly repulsive in CsPbBr$_3$ NCs, in contrast with the strong attractive interactions previously reported and consistent with the time-resolved PL measurements reported in section 5.2. Figure 5-12 shows the shift in peak positions and the component spectral linewidth change as a function of NC size. The shift between the exciton and biexciton spectra, the width of each of the component spectra, and the difference in linewidth between the two component spectra all increase with decreasing nanocrystal size. The increasing trend in the blue-shift between the biexciton and exciton component spectra further supports a repulsive interaction because exciton-exciton interactions are more pronounced in smaller NCs. The increasing linewidth of the component
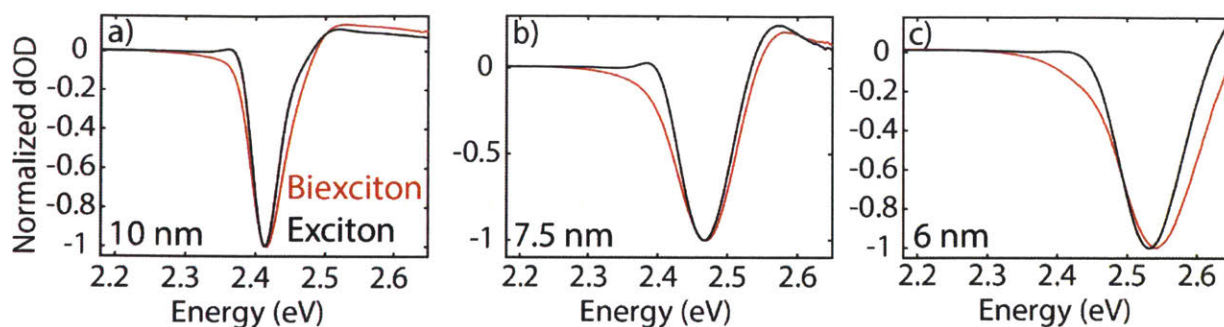
Figure 5-11 Normalized component spectra for the exciton (black trace) and biexciton (red trace) states for the (a) 10 nm, (b) 7.5 nm, and (c) 6 nm NCs. The plots were generated by superimposing the component spectra recovered from 100 random samples of the Markov chain with each normalized to its own peak intensity. The variation among the samples is within the width of the traces.

spectra is consistent with ensemble and single-particle photoluminescence measurements that show that the homogeneous and inhomogenous line width both increase with decreasing NC size.

Careful examination of the component spectra reveals insight into the individual electronic transitions that contribute to the component TA spectra. Specifically, the exciton-to-biexciton transition is present in both the exciton spectrum as induced absorption ($dOD>0$) and in the biexciton spectrum as stimulated emission ($dOD<0$). Induced absorption features are observed on both sides of the exciton peak but manifest more prominently on the blue side, suggesting an exciton-to-biexciton transition that is broader and slightly blue-shifted from the ground state-to-exciton transition. These trends are mirrored in the shape of the biexciton spectrum. Thus, the two component spectra show a consistency with each other that increases confidence in the spectral deconstruction method and the conclusion of a net repulsive exciton-exciton interaction.
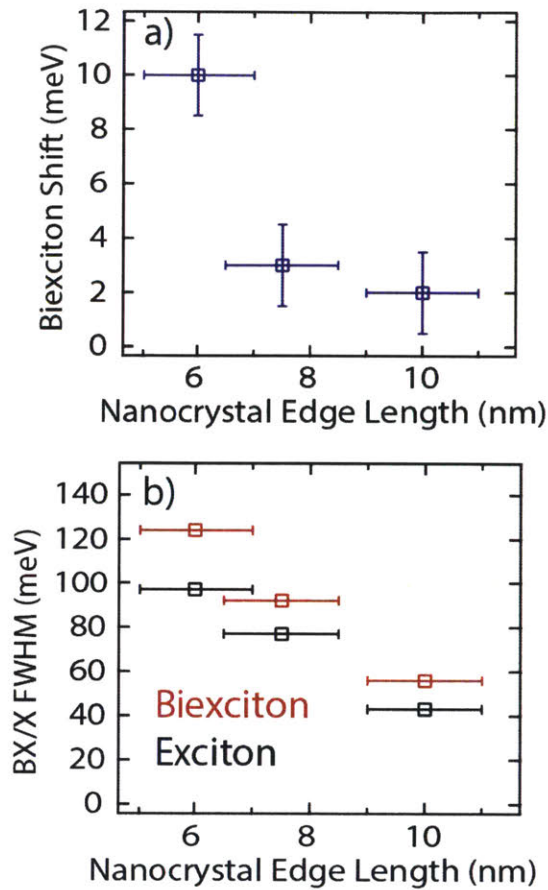
Figure 5-12 Size dependent properties extracted from the component spectra in Figure 5-11. (a) Energy difference between the biexciton and exciton component spectrum peak positions. (b) Full width at half maximum of the biexciton (red) and exciton (black) component spectra.

The values plotted in Figure 5-12 show that the increase in the spectral linewidth of the biexciton state over the exciton state exceeds the overall blue-shift for all three sizes. This effect is also qualitatively visible in the component spectra shown in Figure 5-11 where the dominant bleach/stimulated emission feature in the biexciton spectrum is visibly broader on both sides than the feature in the exciton spectrum. This observation emphasizes how knowing the full spectrum of the biexciton state provides more reliable information about optical gain mechanisms than a single biexciton interaction parameter. In this case, while the exciton-exciton interaction is net repulsive, it is still possible for the biexciton state to contribute to optical gain – a relevant factor for lasing applications – by emission from the red tail of the spectrum. Furthermore, the

observation of red-shifted optical gain from the biexciton state is not a reliable indicator of the sign or value of the biexciton binding energy.

Although quantifying the shift between the component spectra provides a useful characterization of the exciton-exciton interaction, the values should not be quantitatively interpreted as the magnitude of the interaction energy due to a number of qualifying considerations. First, this interpretation does not account for a Stokes shift, which may be different for the exciton and biexciton and is reflected in the data through the stimulated emission contribution to the spectral shape. Another source of quantitative error is a bias in the position of the exciton spectrum. This is due to some late-time spectral dynamics that are not captured by the simple kinetic model. Nonetheless, some estimations can be made about the interaction by carefully examining the trends. It is clear that the exciton-exciton interaction is quite weak, likely <10 meV for all but the smallest NCs. The confidence in the repulsive sign of the interaction is also high due to the size-dependent trend and because the direction of the bias in the exciton spectrum would cause this analysis to underestimate the repulsive character of the interaction.

These conclusions about the nature of exciton-exciton interactions are highly consistent with empirical reports of free-carrier-like behavior in CsPbBr$_3$ NCs since these interactions are quite weak.[126] Although a repulsive exciton-exciton interaction may seem unexpected based on the behavior of conventional QD systems, there are a few properties particular to perovskite NCs that account for this divergent behavior. For example, the overall sign of the four-body Coulomb interaction depends on the spatial overlap of the electron and hole wavefunctions. Core-shell QDs engineered to have strong spatial separation between electrons and holes can exhibit strong exciton-exciton repulsion, and this effect may be occurring, albeit more weakly, in CsPbBr$_3$ NCs. Lead halide perovskites also have some unique structural characteristics that likely affect their

101

electronic properties. In particular, the atomic lattice is polar, highly dynamic, and can deform in response to excited electrons and holes, leading to the formation of polarons in these materials.[138,139] One consequence of polaron formation is screening of Coulomb interactions between charge carriers. Barring spatial displacement of the electron and hole, the net Coulomb interaction is often observed to be attractive, but this may not be true in such a dynamic environment. Additionally, polaron formation effectively solvates the charge carriers through lattice distortion, which requires some number of nuclear degrees of freedom. As the NC size is decreased, the number of possible lattice configurations that can effectively solvate all four charge carriers is reduced. At small enough NC size there may be a net energetic penalty to forming a biexciton versus two excitons on separated NCs. This effect would manifest as an apparent repulsive exciton-exciton interaction. These results indicate that perovskite nanocrystals have somewhat anomalous properties as compared to more traditional semiconductor nanocrystals, and understanding these fundamental properties can help inform the optimization and application of these materials going forward.

5.4 Fluorescence Intermittency Mechanism

Single-nanocrystal studies enable further investigation of the multiexciton properties within the perovskite lattice. By pairing isolated single-particle measurements with solution-phase average single nanocrystal methods described in Chapter 2, a thorough understanding of the dominant kinetic processes can be developed. The solution phase measurements are crucial to demonstrate that the single-nanocrystal results are representative of the ensemble properties, rather than being unique examples of exemplary NCs. To fully understand the rich physics driving multiexciton emission, it is first crucial to understand the fluctuating exciton dynamics. Figure 5-13a and b presents a typical fluorescence intensity trace for a many hour single-NC experiment. It is immediately apparent that this representative NC exhibits fluorescence intermittency

(blinking). Taking a histogram of this intensity trace shows the distribution of intensity states occupied throughout the experiment. The lowest intensity state is shot noise-limited, and consistent with a true dark state. The rest of the observed peaks in the histogram are not shot noise-limited and are likely rather a distribution of many intensity states. Between nanocrystals, a wide variety in number and position of intensity peaks are observed, suggesting these intensity states are dominated by non-radiative states which are not intrinsic to perovskite materials, such as a trap or defect state rather than a charged state. That is not to say that none of these states are trions, just that more than a trion state is necessary to explain the fluorescence intensity trajectories.

The fluorescence lifetime of the entire intensity trajectory is strongly non-exponential, with a rapid quenched component at early times and a large, exponential intermediate time component. In , Figure 5-13c the lifetime as a function of intensity state is plotted, with the color of the trace corresponding to the colored boxes in Figure 5-13a. The highest intensity state has a purely monoexponential lifetime with an extracted decay constant of 26.0±0.2 ns. As the blinking intensity decreases, there are subtle changes to the lifetime including added rapid components at early times and some extended emission tails, but each state is still dominated by the same single exponential time constant for >90% of the observed emission. Similarly, when taking the lifetime-
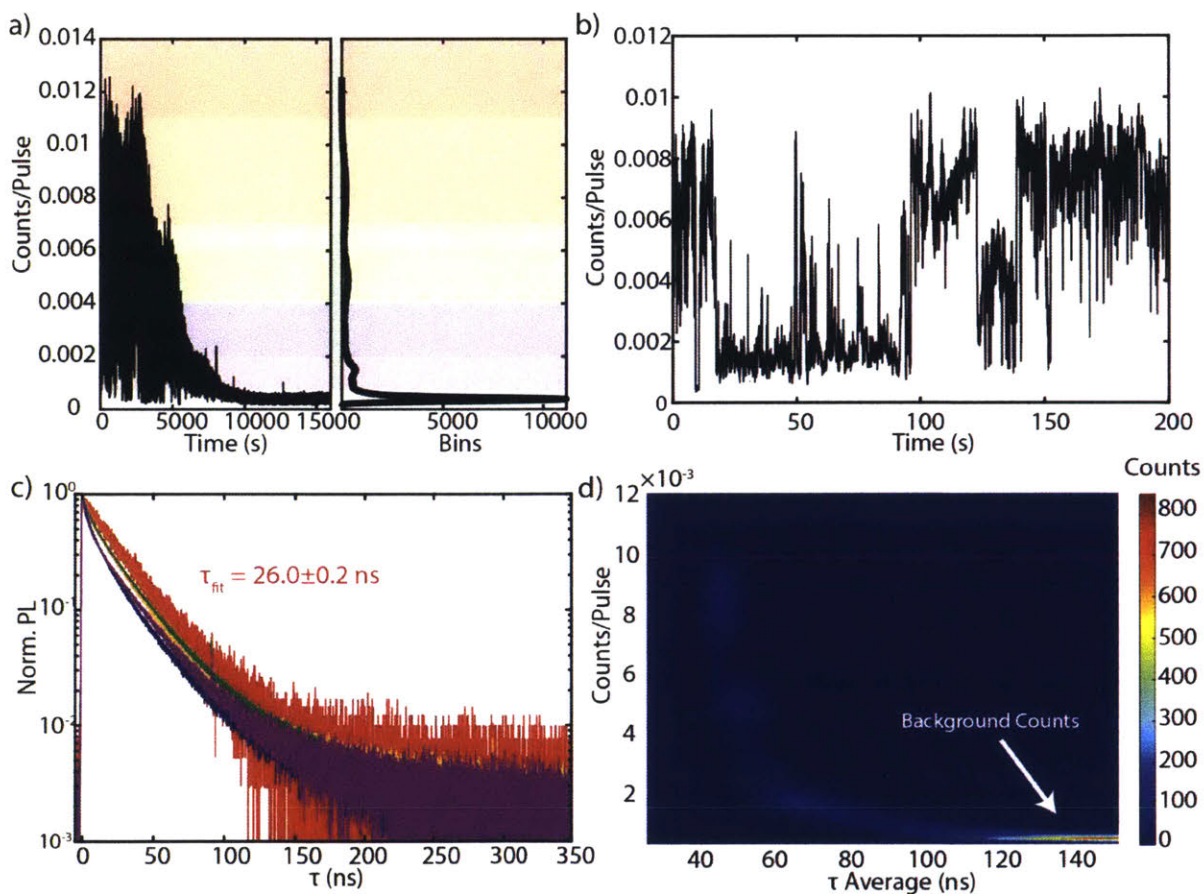
Figure 5-13 a) Fluorescence intensity trace from a single large CsPbBr$_3$ NC with a histogram of the intensity states. b) Zoom of the intensity trace to show many different states rather than binary blinking. c) fluorescence lifetime of various intensity states. The colors correspond to the stripes in part a). d) Fluorescence lifetime intensity correlation plot. The deviation from vertical at low intensities corresponds to the off state where the majority of emission is not correlated in time.

intensity correlation (Figure 5-13d), it is clear that over most of the intensity states, there is no appreciable change in average emission lifetime. Only at the lowest intensities where detected photons are dominated by dark counts does the correlation deviate from the vertical observable in Figure 5-13d. These intensity and lifetime data are consistent with traditional Type B NC blinking mechanisms, where carriers may be trapped during hot carrier cooling, but these trap states are not thermally accessible from the band-edge.[33] If traps are not accessible from the band-edge, their dynamics do not directly compete with radiative emission and thus do not alter the observed lifetime. However, since the absolute number of photons being emitted is decreased when these traps are activated, the total intensity will decrease. A trap state due to likely due to an atomic vacancy or unpassivated surface atom a few hundred meV into the valence or conduction band would be consistent with these dynamics. A distribution of trap states in this energy range would be accessible while cooling from the 405 nm excitation (650 meV excess energy) consistent with the observed fluorescence intensity lifetime correlations.

In order to further test this, excitation wavelength-dependent blinking measurements were performed. Figure 5-14 shows the results from two of these experiments, which demonstrate increased blinking and intermediate states when exciting with 405 nm light (650 meV excess energy) as compared to 484 nm light (120 meV excess energy). Nanocrystals were excited with an equivalent number of incident photons at each wavelength. There is likely a small difference in the number of absorbed photons due to differential absorption cross sections, but both wavelengths are well within the low flux criteria (<<0.01 excitations/pulse), and thus individual excitation events are likely independent with only small fractions of multiexcitons generated as compared to single excitons. These changes to blinking behavior are entirely reversible and independent of the order in which blinking traces are collected, confirming an intrinsic difference in the nonradiative
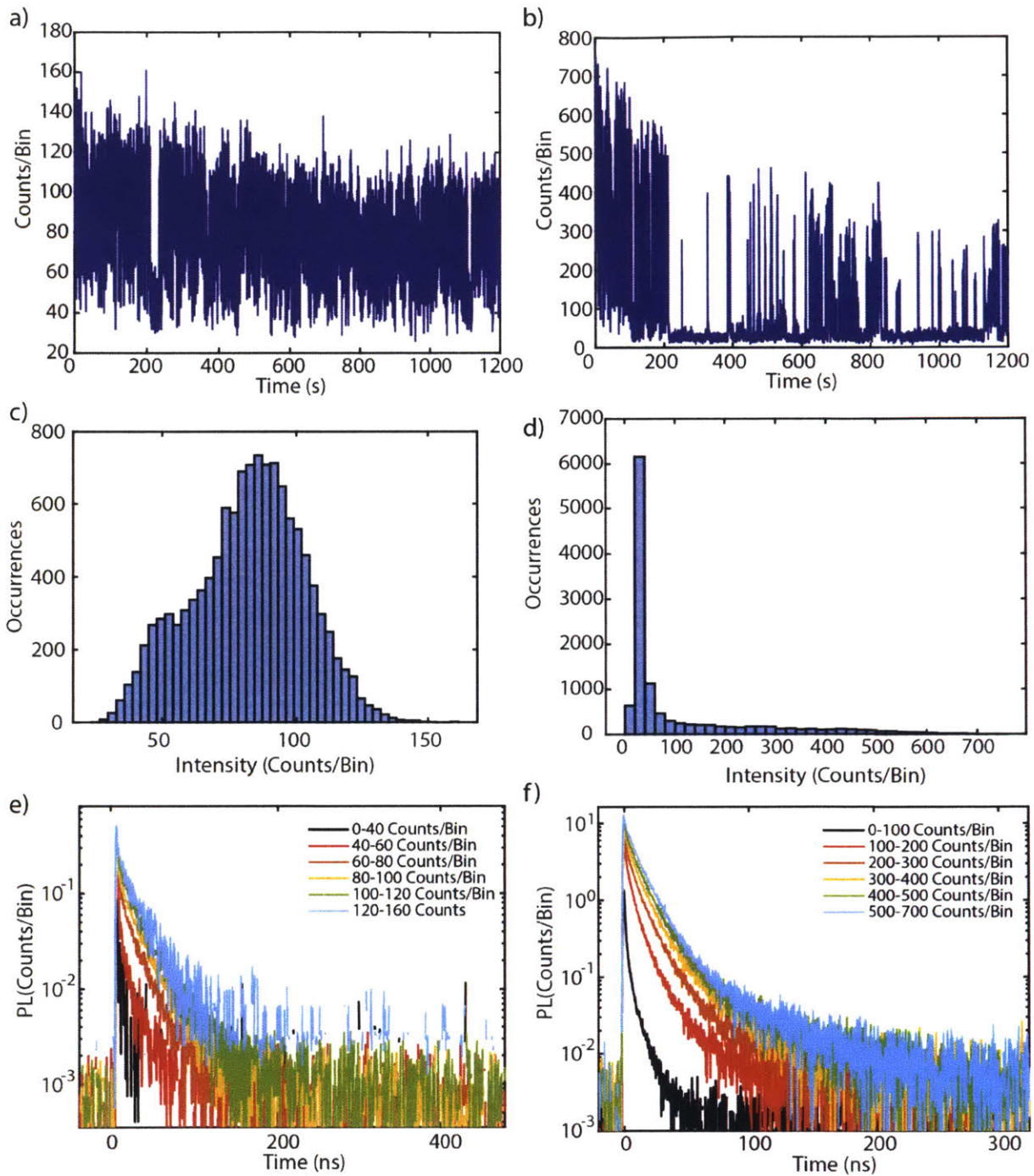
Figure 5-14 a) Fluorescence intensity from a single NC with 484 nm excitation. b) Fluorescence intensity from the same NC with 405 nm excitation. c) Histogram of a). d) Histogram of b). e) Lifetime of various intensity states from a). f) Lifetime of various intensity states from f).

pathways between the two wavelengths. These results are consistent with the model of carrier

trapping while cooling being a dominant cause of blinking in CsPbBr$_3$ NCs, especially when

106

exciting samples deep into the valence or conduction bands.

5.5 Statistical Scaling

Having identified the cause of fluctuating exciton behavior allows deeper interrogation of

the biexciton state. Through solution-averaged single-nanocrystal second-order correlation

methods, the size-dependent biexciton to exciton quantum yield can be extracted (Table 5-2). The

same data also contains the solution averaged biexciton lifetime, but for all three nanocrystal sizes,

the lifetime is instrument response-limited, only indicating it is on average faster than ~600 ps.

The single-nanocrystal second-order correlation is presented in Figure 5-15. The single-

nanocrystal biexciton quantum yield values observed are consistent with the solution averaged

biexciton quantum yield for all three nanocrystal sizes, confirming the size-dependent trend in

quantum yield as shown in Table 5-2 and previously by Utzat et al.[11] The size-dependent biexciton

quantum yield observed by Utzat et al.[11] was explained by the relatively low degree of excitonic

confinement observed in perovskite nanocrystal systems. In the case of $CsPbBr_3$ nanocrystals, the

a)

b)
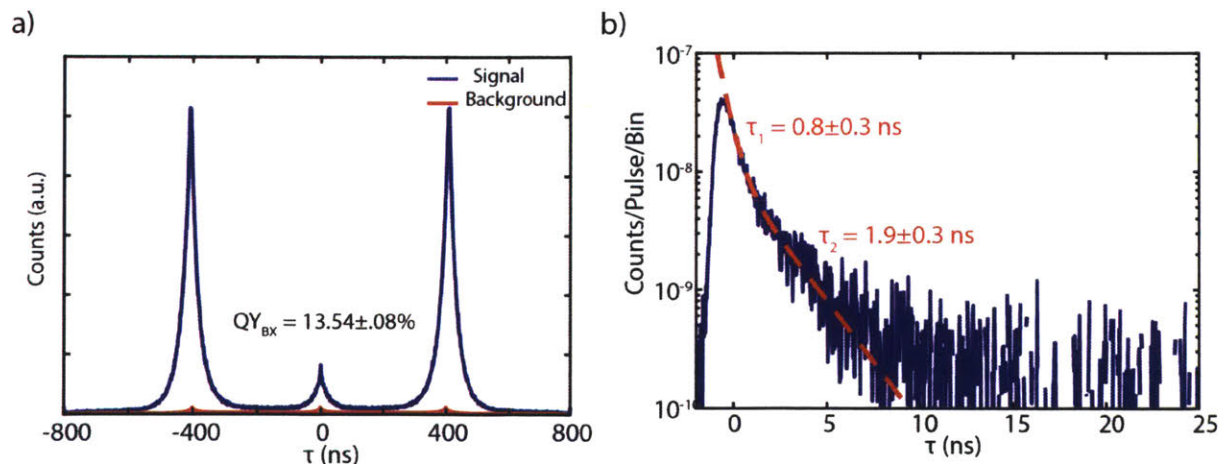
Figure 5-15 a) Second order correlation function showing a biexciton to exciton quantum yield ratio of 13.54±0.08% for a large $CsPbBr_3$ NC. b) Biexciton lifetime showing biexponential decay with time constants of 800 ps and 1.9 ns.
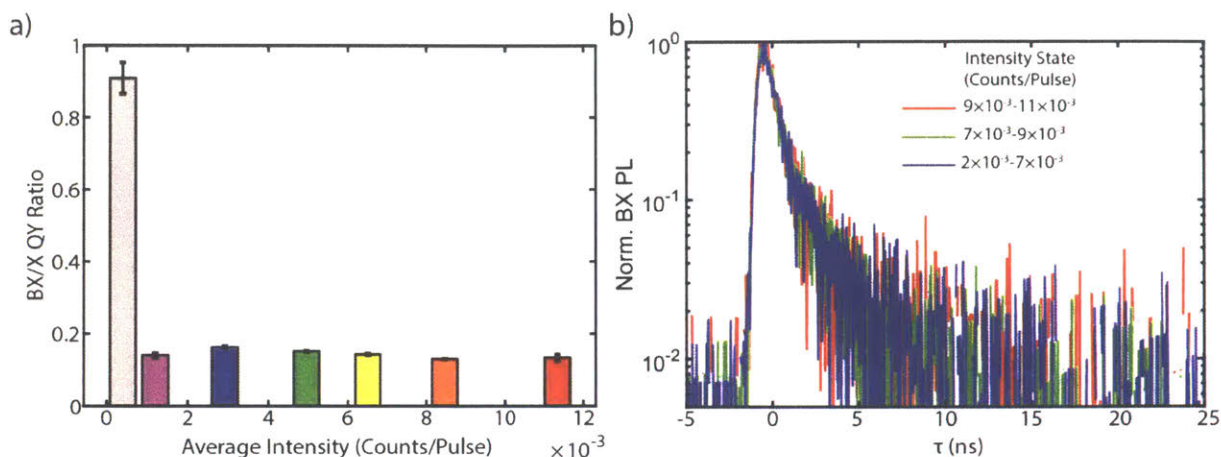
Figure 5-16 a) Biexciton to exciton quantum yield ratio as a function of NC blinking state. The colors of the different intensity state bars correspond to the colors marked in Figure 5-13. b) Biexciton lifetime for three intensity states. Note these do not correspond to the states as in a) due to the increased signal-to-noise requirements to compile a lifetime as compared to a quantum yield.

exciton Bohr radius is ~3.5 nm, which means NCs with edge lengths of ≥10nm are minimally quantum confined, consistent with the lack of a strong exciton resonance in the steady-state absorption spectrum. The reduced excitonic nature of larger nanocrystals likely reduces the Auger rate due to reduced wavefunction overlap.

Furthermore, the single-nanocrystal biexciton lifetimes are predominantly within the instrument response, as illustrated in Figure 5-15. The exception is the biexponential tail in the biexciton lifetime of the 10 nm NC sample. To confirm that none of the observed biexciton behavior is determined by the fluctuating single exciton behavior, Figure 5-16a presents the biexciton quantum yield as a function of intensity state. The lowest intensity state is almost exclusively emission from the glass coverslip, residual solvent, and other non-NC fluorescence sources. Thus, it makes sense that these emission sources have a second order correlation that is essentially unity, or in other words, uncorrelated. At all intensity states that contain appreciable nanocrystal emission, a consistent biexciton to exciton quantum yield ratio is observed. It is important to note that while the center to side peak ratio in a $g^{(2)}$ measurement is usually just referred to as the biexciton quantum yield, this is based on the assumption that the exciton has

unity quantum yield. While this assumption generally holds true for binary blinking samples such as many CdSe NCs, it is clearly untrue for the complex blinking behavior observed in perovskite NCs. From the original derivation of the biexciton quantum yield method by Nair et al.,[53] if all the low-flux conditions are met, the center to side peak ratio is then explicitly

$$g_0^{(2)} = \frac{QY_{BX}}{QY_X} \tag{5-2}$$

Where $g_0^{(2)}$ is the center to side peak ratio, QY_{BX} is the biexciton photoluminescence quantum yield and QY_X is the exciton photoluminescence quantum yield, which are assumed to be independent. In a sample with unity exciton quantum yield, $g_0^{(2)}$ is exactly the biexciton quantum yield. In the case of the data presented in Figure 5-16a, the exciton quantum yield is not unity for all intensity states, and thus the full expression must be utilized. Therefore, a constant biexciton to exciton quantum yield ratio across all emissive states is observed. In other words, whatever nonradiative processes are altering the exciton quantum yield and causing nanocrystal blinking, which were shown in section 5.4 to be intraband carrier trapping, act equivalently on a single exciton as it does on both excitons in a biexciton. The biexciton radiative lifetime and Auger lifetime are unaffected by NC blinking. If nanocrystal blinking were dominated by the formation of charged states (trions), the Auger rateof the biexciton state ought to change with intensity state, which is not observed.

The biexciton dynamics further support this finding. There is no change in the biexciton emission dynamics as a function of nanocrystal blinking, even in the large CsPbBr3 nanocrystals that display non-monoexponential recombination dynamics (Figure 5-16b). Since the non-monoexponential nature of the biexciton lifetime is most pronounced in large NCs, it is likely correlated to reduced confinement, which allows for multiple different stable fluctuating biexciton states with different recombination dynamics.
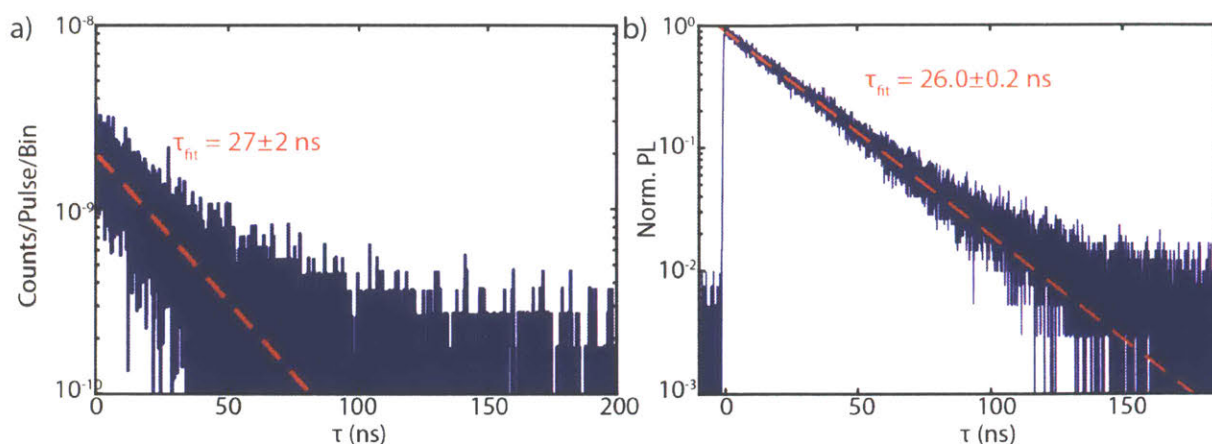
Figure 5-17 a) PNRL[2,1,2] for all intensity states shown in Figure 5-13a. The lifetime is fit to a monoexponential function with a decay constant of 27 ns. b) Exciton lifetime of the highest intensity state depicted in Figure 5-13a fit to a monoexponential function with a decay constant of 26 ns.

Finally, the lifetime of the second emitted photon of the biexciton, or residual exciton can also provide evidence towards the origin of NC blinking and the nature of the biexciton state. In CdSe nanocrystal systems, this state is identical to a single exciton as was shown in Chapter 4. The lifetime of the residual exciton from a biexciton in $CsPbBr_3$ NCs is identical to that of the lifetime of the brightest blinking state (Figure 5-17). Assuming all non-radiative processes are only accessible during hot carrier cooling, then the residual exciton should not be able to access any of these trap states, resulting in unity quantum yield once cooled and purely radiative, monoexponential recombination dynamics. Biexciton recombination is thus entirely consistent with the type B blinking mechanism presented above. Furthermore, the presence of these trap states does not in any way alter the processes that control multiexciton emission in perovskite NCs.

Chapter 4 details the consistency of CdSe biexciton emission with established statistical scaling models. To reiterate, the basis of statistical scaling is that the underlying dynamics of a state do not change when adding excitons to a NC, just the combinatorial number of recombination pathways. It is this combinatorial multiplication which speeds up the biexciton radiative lifetime by a factor of four as compared to the exciton radiative lifetime. For all the $CsPbBr_3$ nanocrystals

110

studied, the dominant component of the biexciton lifetime is instrument response-limited. Even with the lifetime being instrument response-limited, the biexciton lifetime that would be predicted by the statistical scaling model can be calculated using equation (5-3).

$$\tau_{BX} = \frac{1}{4}\tau_X QY_{BX}$$ (5-3)

Where τ_{BX} is the measured biexciton lifetime, τ_X is the exciton radiative lifetime, and QY_{BX} is the biexciton quantum yield. Table 5-2 presents these results utilizing the exciton radiative lifetime and biexciton quantum yield measured from a typical single nanocrystal within each sample.

Table 5-2 Exciton radiative lifetimes extracted from single NC data and solution biexciton quantum yield values used to predict the statistical scaling biexciton lifetime.

NC Size (nm)	Exciton Radiative Lifetime (ns)	Biexciton Quantum Yield (%)	Predicted Biexciton Lifetime (ps)
6	3	7	53
7.5	10	10	250
10	26	14	910

Note that the predicted biexciton lifetime for the largest NC sample is longer than a typical instrument response (~600 ps), but both the solution phase biexciton lifetime and the fast component of the single nanocrystal biexciton lifetime are instrument limited. Table 5-3 compares the predicted statistical scaling lifetime to the biexciton lifetimes extracted from the transient absorption measurements presented in section 5.3.

Table 5-3 Comparison of the expected biexciton lifetime from a statistical scaling model (calculated in Table 5-2) and the biexciton lifetime extracted from the TA data (presented in Table 5-1).

NC Size (nm)	Statistical Scaling Biexciton Lifetime (ps)	Transient Absorption Biexciton Lifetime (ps)	Ratio
6	53	36	1.5
7.5	250	56	4.5
10	910	205	4.4

The ratio between the statistical scaling lifetime and the extracted transient absorption lifetime is a measure of how much faster the radiative lifetime is compared to established models. Unfortunately, these scaling results are biased by ensemble heterogeneity, and to truly measure a scaling factor, single nanocrystal techniques are best. Returning to the results presented by Utzat et al.,[11] it is likely that $CsPbI_3$ NCs will have a drastically longer biexciton lifetime due to the higher biexciton quantum yield and the longer exciton lifetime.

To confirm the deviation from statistical scaling predictions on a single NC level, single $CsPbI_3$ NCs are examined using the same fluorescence techniques as described for CdSe and $CsPbBr_3$. The iodide perovskite NCs also demonstrate complex blinking behavior, similar in nature to that of the $CsPbBr_3$. The biexciton lifetime and biexciton to exciton quantum yield ratio remain consistent across most blinking states. The lower intensity states, however, show dramatic changes in exciton lifetime, suggesting they correspond to charged states rather than the type B blinking mechanism. Since the goal is to extract information inherent to exactly the four carrier state, these low intensity states are not used in the analysis. The exciton lifetime, biexciton quantum yield, and biexciton lifetime of $CsPbI_3$ nanocrystals are presented in Figure 5-18. The large
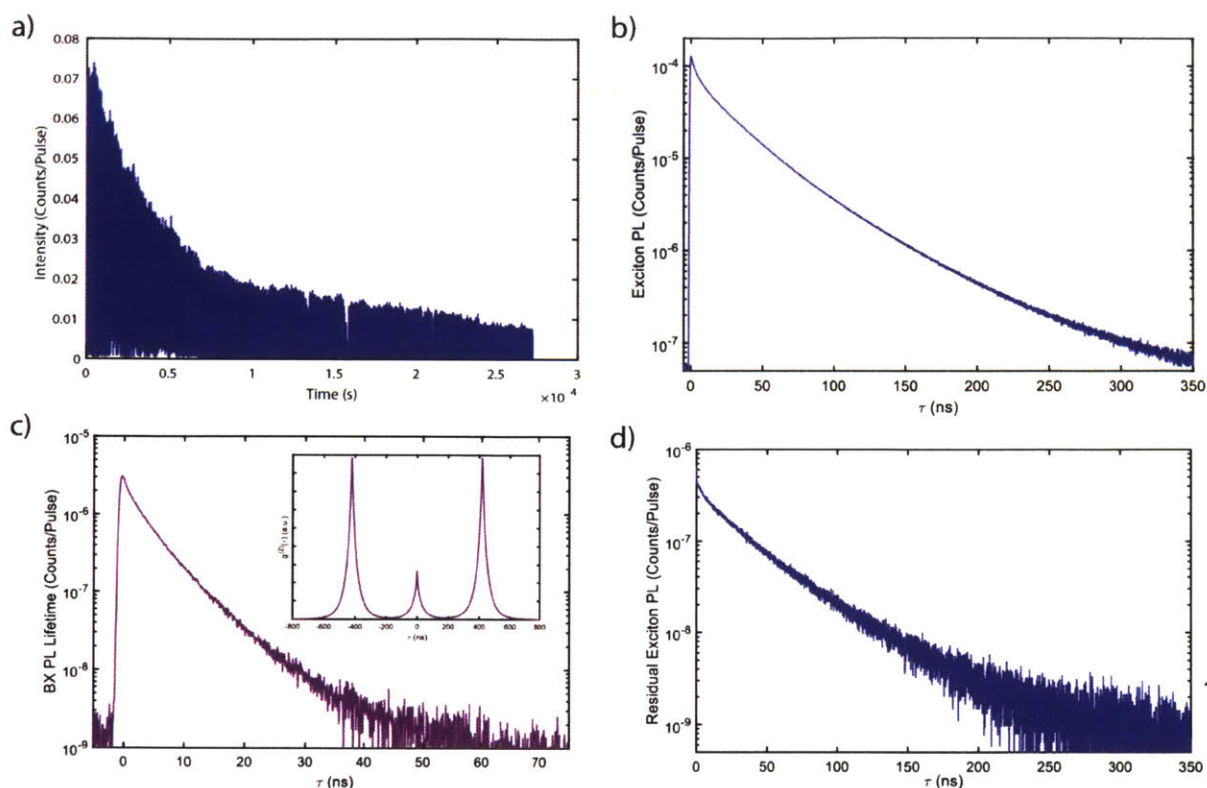
Figure 5-18 a) Fluorescence intensity trace for a large $CsPbI_3$ NC shoing multiple emissive states. b) Exciton lifetime (high intensity blinking states only) for the same $CsPbI_3$ NC showing multiexponential decay which is distinctly non-exponential. c) Biexciton lifetime and quantum yield of the high intensity emissive state. d) $PNRL^{(2,1,2)}$ for the high intensity state showing the same dynamics as in b).

biexciton quantum yield for minimally quantum confined $CsPbI_3$ NCs is consistent with the solution phase biexciton quantum yield trend published by Utzat et al.[11]

Extracting statistical scaling values from the exciton lifetime, biexciton lifetime, and biexciton quantum yield in large $CsPbI_3$ proves challenging. While the biexciton dynamics are indeed much longer than the instrument response, neither the exciton nor the biexciton exhibit monoexponential decays. Both the exciton and biexciton have a dominant exponential component which can be fitted, but a single radiative rate is clearly insufficient to explain the dynamics of either state. The lifetime of the second photon of the biexciton displays the same nonexponential decay as the single exciton, demonstrating a consistent lack of state memory. Furthermore, this suggests that the nonexponential dynamics are intrinsic to the sample rather than being due to a

113

transient trap or charge. It is possible that the traps invoked to explain blinking in $CsPbBr_3$ NCs are simply close enough in energy to the band-edge for $CsPbI_3$ NCs that they are thermally accessible and thus contribute to emission dynamics and intensity. Other possible explanations include transient lattice deformations which change Coulomb shielding and thus radiative rates, as well as carrier separation or loss of excitonic character within the NC. A crucial piece of evidence to identify the cause of this nonexponential decay will be studying the multiexciton dynamics of more highly confined $CsPbI_3$ NCs. If the driving force is competitive lattice distortions as suggested by the TA results, the nonexponential behavior ought to be more pronounced in smaller NCs where there are fewer nuclear degrees of freedom. If the nonexponential behavior is due to transient carrier separation in which the NC is behaving with more bulk-like properties, then the nonexponential dynamics will be more pronounced in larger NCs. These studies are ongoing and will hopefully shed light on the mechanism of multiexciton interactions in the weakly confined, highly labile perovskite NC system.

5.6 Conclusion

In conclusion, we performed time- and spectrally-resolved photoluminescence on $CsPbBr_3$ nanocrystals while carefully controlling the sample's exposure to air. The photoluminescence spectra and post-exposure characterization of the samples suggest that the fast red-shifted emission feature often attributed to an emissive biexciton occurs due to the formation of larger bulk-like particles. Further analysis of the spectra suggests that the biexciton interaction is quite weak and consistent with observations of free-carrier-like behavior and other known properties of lead halide perovskite nanocrystals.

Next, fluence-dependent transient absorption measurements were combined with careful spectral deconvolution to determine the full spectral properties of the biexciton state in $CsPbBr_3$

NCs and evaluate the overall strength of exciton-exciton interactions in this material system. Exciton-exciton interactions in CsPbBr$_3$ NCs are net repulsive, and the repulsive interaction becomes stronger as the NC size decreases. Furthermore, knowledge of exciton and biexciton transition lineshapes is needed to accurately interpret optical gain mechanisms, and observation of red-shifted optical gain is an insufficient indicator of the biexciton binding energy.

Finally, single nanocrystal studies reveal that NC intensity intermittency is consistent with transient trap states which are inaccessible from the band-edge. Multiexciton studies reveal nonexponential dynamics for large NC samples, suggesting that the loss of excitonic nature drastically changes the identity of multiexciton states as compared to the established understanding built on CdSe and other II-VI NC systems. Combining the multiexciton dynamics extracted from the TA data with solution biexciton quantum yields, suggests that the biexciton lifetime in perovskite NCs is not consistent with statistical scaling models. In total, these results demonstrate that established models must be reconsidered when studying perovskite NCs in order to capture the true material properties.

5.7 Methods

Nanocrystal samples were synthesized according to the methods described by Krieg *et al.*[142] After synthesis, samples were stored in a nitrogen environment with low water and oxygen content (<0.01 and <0.2 ppm respectively). Photoluminescence samples were prepared in a nitrogen glovebox through dilution with toluene to concentrations corresponding to ~0.01 absorbance at the main exciton peak. After dilution, samples were placed in 2 mm path length quartz cuvettes (Spectrocell), capped, and wrapped in Parafilm to ensure a continuing air-free environment. For air-exposed samples, preparation steps remained the same except immediately before measurement, the Parafilm was removed and the cuvette opened for ~5 seconds. The cap

and Parafilm were then replaced, and the sample agitated to mix any air into the sample homogeneously.

Bulk perovskite films were synthesized by a reprecipitation method. Precursor solutions of 0.2M CsBr and 0.5M PbBr2 in N,N-dimethylformamide (DMF) are prepared then mixed in a five to two volumetric (one to one molar) ratio. 100 μL of the mixed precursor solution is added dropwise to 10 mL of toluene. The mixed precursor toluene solution is stirred vigorously for one minute then centrifuged at 4300 rpm for ten minutes. The precipitate is redispersed in 120 μL of toluene and drop cast on a glass slide, then dried under vacuum. Photoluminescence spectra of the bulk polycrystalline film were taken using an Avantes fiber-optic spectrometer and excited using a 365 nm fiber-coupled LED (Thorlabs).

During spectrally resolved photoluminescence measurements, samples were excited with 50 fs pulses at 400 nm using the output of a commercial noncollinear optical parametric amplifier with an integrated harmonics generator (Spectra-Physics Spirit NOPA). The laser beam was spatially filtered by focusing through a 10 μm pinhole, and then coupled into a Nikon Ti-U inverted microscope. The excitation was focused into the sample and the excitation was collected using the same 40x air objective (Nikon) with a correction collar set to correct for the 1 mm cuvette wall. The emitted light was focused into a 500 mm focal length monochromator equipped with a 150 gr/mm grating. The monochromator output was collected and focused into an APD. Photoluminescence lifetimes were collected by sending the electrical pulses from the APD to a time-correlated single photon counting unit (Picoquant Picoharp 300). The synchronization signal was generated by separating a fraction of the excitation source using a beam splitter, focusing it into a high-speed photodiode (Thorlabs), and using the photodiode output to trigger a digital delay generator (Stanford Research Systems DG645) to send pulses of the correct voltage and polarity

116

to the TCSPC unit. The complete system had an IRF of 160 ps, and the count rate at the detector was maintained at ≤800 counts per second to avoid artifacts. A PL decay trace was collected at each spectral position by scanning the monochromator in 1 nm increments.

Solution biexciton quantum yield and lifetime measurements were completed utilizing the methods described by Beyler *et al.*[55] and Bischof *et al.*[56] respectively. Samples contained within a 100 μm thick microcapillary are excited with a 405 nm pulsed excitation source (Picoquant) at a repetition rate of 2.5 MHz. Excitation and emission were separated by a 425 nm long pass filter (Thor Labs, DMLP425). Nanocrystal emission was further filtered using a spatial pinhole (100 mm lenses, 50 μm) and a 425 long pass filter (Edmund Optics). The emitted beam was then split into four by three 50:50 beam splitters as illustrated by Shulenberger *et al.*[54] Each beam is directed towards a single-photon counting detector (Perkin Elmer, SPCM-AQR13). Photon arrival times were recorded by a HydraHarp 400 (Picoquant) and analyzed using home-built software published at https://github.com/tsbischof/photon_correlation and https://github.com/hutzat/photons.

Single-particle measurements were conducted on the same instrument as the single-particle CdSe measurements. A full description may be found in section 4.5.

6 Chapter

Future Work

6.1 Biexciton Binding Energy of a Single Nanocrystal

Chapters 4 and 5 discuss in some detail the biexciton binding energy of both CdSe and perovskite nanocrystals. What was hopefully apparent is that there are a number of methods currently utilized to extract this parameter, all of which have distinct drawbacks. Power-dependent PL measurements in theory should provide a good avenue to extract the biexciton shift, however, due to signal-to-noise and spectral resolution issues, the biexciton binding energy is frequently lost in the envelope of exciton emission. Transient absorption methods are also frequently utilized for this purpose. Unfortunately, due to the high degree of spectral overlap between the exciton and biexciton spectrum, it is often non-trivial to separate these features. Generally, features near the main excitonic bleach are fit to two gaussians at high power, or single wavelength features are
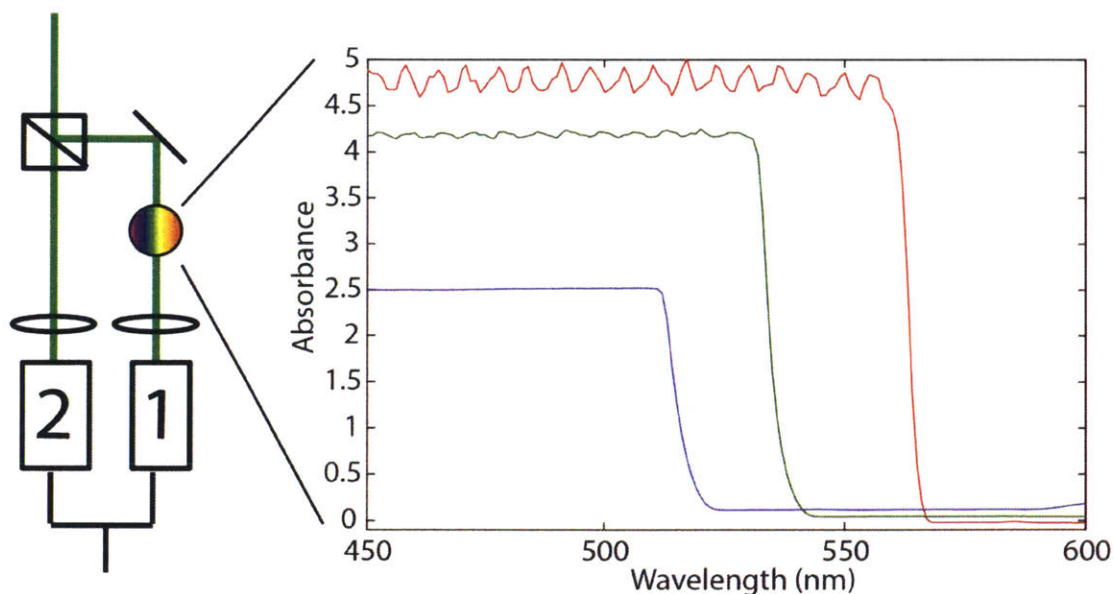
Figure 6-1 Detector geometry for the single-particle biexciton binding energy measurement. The multicolored circle represents a high-precision edge-pass filter mounted to a rotational stage. The absorbance spectrum illustrates that by rotating the filter from 0 degrees to 45 degrees, the cut-off wavelength can be tuned by many tens of nanometers.

tracked as a function of time and excitation power. Chapter 5 demonstrates how these methods fail to capture a lot of the nuance in the biexciton spectrum, and how many frequently held assumptions, like the exciton and biexciton having the exact same spectral lineshape, are not necessarily true. Chapter 5 presents the exciton and biexciton transient absorption spectra for both the exciton and biexciton state. While these spectra provide useful information on the nature of the two states, and exciton-exciton interactions in the perovskite lattice, it is important to note that transient absorption spectra contain information about a number of competing processes. Take the exciton spectrum; it contains the ground state bleach for the ground-to-exciton transition, induced absorption from the exciton-to-biexciton state transitions, and stimulated emission from the exciton state. There is no rigorous method to separate these three features, and thus general conclusions must be drawn based primarily on the peak energy and spectral linewidth. There would be great advantage in directly measuring the biexciton photoluminescence spectrum as it contains fewer compounding influences. In particular, measuring the biexciton spectrum from an individual NC would allow comparison of linewidth and energy without any effects from heterogeneous broadening. This could be crucial because it is unknown whether heterogeneous broadening is consistent between the exciton and biexciton states.

One possible method to extract the single NC biexciton PL spectrum is to utilize established second order correlation methods, combined with tunable, high-precision edge-pass filters. The experiment is illustrated in Figure 6-1. In brief, the experiment geometry is quite similar to that of a traditional $g^{(2)}$ measurement where the emission beam is spatially and spectrally filtered to remove out of plane light and laser scatter, then split into two equivalent beams which are focused onto single-photon counting detectors. The primary difference is that one detection beam is also spectrally filtered using an edge-pass filter. The cutoff wavelength of these filters is changed

based on the angle of incidence, and thus can be swept across the spectrum. Here I propose combining one long-pass and one short-pass filter such that the total number of nanocrystal counts can be maximized while still exploring the entire spectral range. At each filter position, t3 data can be collected. Through post-processing the exciton and biexciton spectra can then be reconstructed. The exciton spectrum is contained within one-photon detection events in which the photon arrived at the filtered detector, while the biexciton spectrum is contained within two-photon events where the first photon arrived at the filtered detector. Simultaneously, this measurement will also provide the spectrum of the second photon from a biexciton, allowing us to confirm whether that this state is not only identical in dynamics to a single exciton as presented in Chapter 4, but also in spectrum.

There will be a number of technical challenges that must be overcome to achieve this measurement. First, a mathematical algorithm to reconstruct the exact NC spectrum from the linear combination of intensities and filter absorption spectra must be developed. There are a number of examples of how to use differential absorption spectra to reconstruct a detected spectrum, and thus this should not pose too great a challenge. Additionally, nanocrystal emission is not constant over long experiments. Nanocrystal blinking tends to increase with longer integration times, even in the most stable of CdSe NC samples. Under low-flux count rates it takes approximately 20 to 30 minutes to acquire a nice $g^{(2)}$ trace with high signal-to-noise in a minimally blinking NC. Thus, to achieve high spectral resolution, a single nanocrystal will have to be examined over a many hour period. The integration time may be reduced through nonlinear spectral sampling, with more data points taken around the peak of the exciton fluorescence spectrum, and fewer towards the tails. Finally, and potentially most importantly, changes in the NC must be accounted for throughout the duration of the measurement. To normalize different degrees of NC blinking, the side peak of the $g^{(2)}$ must be considered. Generally speaking, this side peak only considers the cross correlation.

However, in this experiment, that would require that one of the side peak photons arrives at the filtered detector. If only considering photons which both arrive at the unfiltered detector, detector afterpulsing, which extends for many hundreds of nanoseconds, becomes a serious concern. None of these concerns are insurmountable, but must be seriously considered and eliminated as a source of experimental error or bias before proceeding.

It would be of great interest to complete this measurement and then compare to biexciton and exciton TA spectra that are extracted utilizing the target analysis method described in Chapter 5. For example, the combination of these methods could allow us to determine of the Stokes shift for the biexciton and exciton state are the same, among other things. The overall goal of this experiment would be to determine whether our established understanding of the energetics of the biexciton state and the assumptions so often invoked when modeling or fitting these states are accurate, and through these tests, to deepen our understanding of exciton-exciton interactions in semiconductor NCs.

6.2 Size-Dependent CdSe Nanoplatelet Biexciton Dynamics

The bulk of this thesis has set forth to describe the nature of exciton-exciton interactions in different material systems and different multiexciton states. To do so, both biexciton and triexciton states have been deeply investigated in CdSe NCs and the biexciton state in perovskite NCs.

One avenue of confinement that was not investigated in this thesis is dimensionality. Both perovskite and CdSe nanomaterials can be made into one-dimensionally confined colloidal nanoplatelets. These platelets show strong excitonic confinement in the z-direction, and minimal to no confinement in the x- and y-directions. The strong confinement in the z-direction provides a large exciton binding energy, much larger than in three-dimensionally confined nanocrystals. If only considering the energetics of the states, it would lead to the conclusion that the biexciton state must also be strongly bound. However, the large lateral size also provides an entropic driving force

to separate the two excitons, not even considering exciton separation into a free electron and hole. Using a basic coarse-grained model, one can estimate the entropic driving force that would be expected based on the size of the exciton and the lateral size of the nanoplatelet. For example, if the exciton Bohr radius is ~2 nm in the lateral dimension, and a nanoplatelet has edge lengths of 10 nm and 30 nm, the platelet can be broken into a 5×15 grid which corresponds to different exciton sites. If we assume the biexciton has the same spatial extent as the exciton, an assumption that may not be completely accurate in these strongly confined systems, then the number of microstates accessible to a bound correlated biexciton is just the number of lattice positions (N) or 75. If we allow the biexciton to separate into two free excitons, then the number of microstates is N(N-1) or 5,550. The entropy of a state is directly correlated to the number of microstates in the below equation.

$$S = k_B ln\omega \hspace{3cm} (6\text{-}1)$$

Where S is the entropy, k_B is the Boltzmann constant, and ω is the number of microstates. A bound biexciton would then have an entropy of 0.37 meV/K and two free excitons would have an entropy of 0.74 meV/K. Thus the NC temperature will, unsurprisingly, play an important role in the bound nature of the biexciton state. The lateral size of the nanoplatelet will also have a great effect, with larger nanoplatelets providing a larger increase in available microstates for free biexcitons as compared to bound biexcitons. This tradeoff is further complicated by the fact that most nanoplatelet syntheses result in particles much smaller than the diffraction-limited excitation spot used in many confocal experiments, resulting in excitations evenly distributed across the nanoplatelet area. Thus it is quite possible to create a "multiexciton" in a state which is not spin- or energy-correlated.

Biexciton analyses on single CdSe nanoplatelets as described for both CdSe nanocrystals and perovskite nanocrystals in this thesis would provide a great first test of these hypotheses. The biexciton lifetime of a strongly spin- and energy-correlated biexciton state should obey established statistical scaling models. In theory, a state consisting of two truly independent excitons on a nanoplatelet should have first photon recombination dynamics equal to exactly one half the exciton lifetime. These two limits of lifetime scaling cases can inform us on the degree of exciton separation based on nanoplatelet lateral size. These measurements would also be greatly enhanced by TA studies similar to those completed for the perovskite NCs in this thesis, as there should be significant differences in the energetics of a bound biexciton state as compared to a separated biexciton, and this could provide crucial energetic evidence for exciton separation.

6.3 Investigation of Shell Effect on Triexciton Recombination

In Chapter 4, the scaling and emission wavelength of the triexciton was thoroughly investigated in a CdSe/CdS core-shell sample. In this sample, triexciton recombination occurs almost exclusively from the S-like band-edge state. Modeling results suggest that the degree to which the triexciton emits from the band-edge is likely controlled by the degree of P-like carrier separation as induced by the thick NC shell. To test this, these experiments can be repeated with a
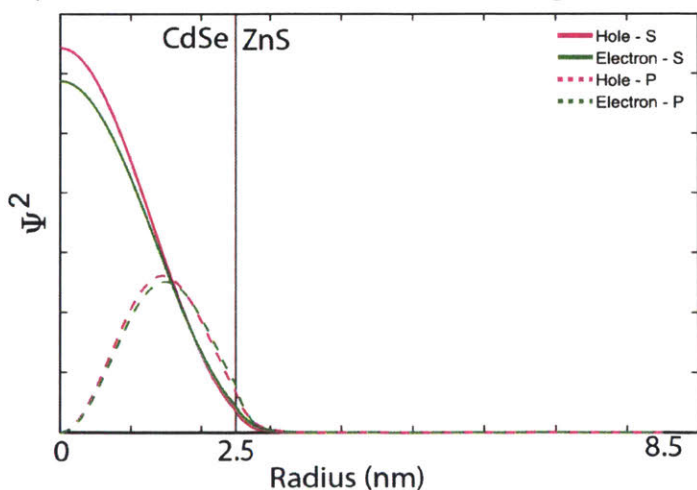
Figure 6-2 Particle in a sphere modeling of the electron and hole wavefunctions for a CdSe/ZnS core-shell NC.

123

series of CdS shell thicknesses, similar to how statistical scaling was tested for the biexciton in Chapter 4. The extreme case would even involve considering the triexciton recombination dynamics in a CdSe/ZnS heterostructure that has a type I band alignment, with both the electron and hole confined to the CdSe core. Thus, in that case, the carrier wavefunction overlap should not change based on the shell thickness. The same particle in a box modeling which was performed on CdSe/CdS core-shell systems was also performed for CdSe/ZnS NCs. These results are shown in Figure 6-2, and indicate that there is minimal difference in the electron-hole wavefunction overlap for the S-like and P-like states. Therefore, the difference in branching ratio for triexciton emission for the S-like and P-like states on CdSe/ZnS nanocrystals should directly interrogate the relative intrinsic radiative rates of the states in the CdSe lattice. The ZnS shell should also serve to increase the NC quantum yield through passivating surface states and isolating excitons from fluctuating environmental conditions without effecting the energy landscape which the exciton occupies.

7 References

(1)   Qian, L.; Zheng, Y.; Xue, J.; Holloway, P. H. Stable and Efficient Quantum-Dot Light-Emitting Diodes Based on Solution-Processed Multilayer Structures. *Nat. Photonics* **2011**, *5* (9), 543–548.

(2)   Chuang, C. H. M.; Brown, P. R.; Bulović, V.; Bawendi, M. G. Improved Performance and Stability in Quantum Dot Solar Cells through Band Alignment Engineering. *Nat. Mater.* **2014**, *13* (8), 796–801.

(3)   Keuleyan, S.; Lhuillier, E.; Brajuskovic, V.; Guyot-Sionnest, P. Mid-Infrared HgTe Colloidal Quantum Dot Photodetectors. *Nat. Photonics* **2011**, *5* (8), 489–493.

(4)   Tvrdy, K.; Kamat, P. V. Substrate Driven Photochemistry of CdSe Quantum Dot Films: Charge Injection and Irreversible Transformations on Oxide Surfaces. *J. Phys. Chem. A* **2009**, *113* (16), 3765–3772.

(5)   Haverinen, H. M.; Myllyla, R. A.; Jabbour, G. E. Inkjet Printed RGB Quantum Dot-Hybrid LED. *J. Disp. Technol.* **2010**, *6* (3), 87–89.

(6)   Haverinen, H. M.; Myllylä, R. A.; Jabbour, G. E. Inkjet Printing of Light Emitting Quantum Dots. *Appl. Phys. Lett.* **2009**, *94* (7), 12–15.

(7)   Wood, V.; Panzer, M. J.; Chen, J.; Bradley, M. S.; Halpert, J. E.; Bawendi, M. C.; Bulović, V. Inkjet-Printed Quantum Dot-Polymer Composites for Full-Color AC-Driven Displays. *Adv. Mater.* **2009**, *21* (21), 2151–2155.

(8)   Murray, C. B.; Norris, D. J.; Bawendi, M. G. Synthesis and Characterization of Nearly Monodisperse CdE (E = S , Se , Te) Semiconductor Nanocrystallites. *J. Am. Chem. Soc.* **1993**, No. 4, 8706–8715.

(9)   Protesescu, L.; Yakunin, S.; Bodnarchuk, M. I.; Krieg, F.; Caputo, R.; Hendon, C. H.; Yang, R. X.; Walsh, A.; Kovalenko, M. V. Nanocrystals of Cesium Lead Halide Perovskites (CsPbX 3 , X = Cl, Br, and I): Novel Optoelectronic Materials Showing Bright Emission with Wide Color Gamut. *Nano Lett.* **2015**, *15* (6), 3692–3696.

(10)   Chen, O.; Zhao, J.; Chauhan, V. P.; Cui, J.; Wong, C.; Harris, D. K.; Wei, H.; Han, H.-S.; Fukumura, D.; Jain, R. K.; et al. Compact High-Quality CdSe-CdS Core-Shell Nanocrystals with Narrow Emission Linewidths and Suppressed Blinking. *Nat. Mater.* **2013**, *12* (5), 445–451.

(11)   Utzat, H.; Shulenberger, K. E.; Achorn, O. B.; Nasilowski, M.; Sinclair, T. S.; Bawendi, M. G. Probing Linewidths and Biexciton Quantum Yields of Single Cesium Lead Halide Nanocrystals in Solution. **2017**, 6838–6846.

(12)   Coropceanu, I.; Rossinelli, A.; Caram, J. R.; Freyria, F. S.; Bawendi, M. G. Slow-Injection Growth of Seeded CdSe/CdS Nanorods with Unity Fluorescence Quantum Yield and Complete Shell to Core Energy Transfer. *ACS Nano* **2016**, *10* (3), 3295–3301.

(13)   Chen, Y.; Vela, J.; Htoon, H.; Casson, J. L.; Werder, D. J.; Bussian, D. a; Klimov, V. I.; Hollingsworth, J. a. "Giant" Multishell CdSe Nanocrystal Quantum Dots with Suppressed Blinking. *J. Am. Chem. Soc.* **2008**, *130* (15), 5026–5027.

(14)　Gao, Y.; Peng, X. Photogenerated Excitons in Plain Core CdSe Nanocrystals with Unity Radiative Decay in Single Channel: The Effects of Surface and Ligands. *J. Am. Chem. Soc.* **2015**, *137* (12), 4230–4235.

(15)　Zhao, J.; Chen, O.; Strasfeld, D. B.; Bawendi, M. G. Biexciton Quantum Yield Heterogeneities in Single CdSe (CdS) Core (Shell) Nanocrystals and Its Correlation to Exciton Blinking. *Nano Lett.* **2012**, *12* (9), 4477–4483.

(16)　Hu, Y. Z.; Koch, S. W.; Lindberg, M.; Peyghambarian, N.; Pollock, E. L.; Abraham, F. Biexcitons in Semiconductor Quantum Dots. *Phys. Rev. Lett.* **1990**, *64* (15), 1805–1807.

(17)　Lounis, B.; Bechtel, H. A.; Gerion, D.; Alivisatos, P.; Moerner, W. E. Photon Antibunching in Single CdSe/ZnS Quantum Dot Fluorescence. *Chem. Phys. Lett.* **2000**, *329* (5–6), 399–404.

(18)　Laubsch, A.; Sabathil, M.; Bergbauer, W.; Strassburg, M.; Lugauer, H.; Peter, M.; Lutgen, S.; Linder, N.; Streubel, K.; Hader, J.; et al. On the Origin of IQE-'droop' in InGaN LEDs. *Phys. Status Solidi* **2009**, *6* (SUPPL. 2), 913–916.

(19)　Lim, J.; Park, Y. S.; Wu, K.; Yun, H. J.; Klimov, V. I. Droop-Free Colloidal Quantum Dot Light-Emitting Diodes. *Nano Lett.* **2018**, *18* (10), 6645–6653.

(20)　Ashcroft, N. W.; Mermin, N. D. *Solid State Physics*; Saunders College Publishing, 1976.

(21)　McLean, T. P.; Loudon, R. Exciton Energy Levels in Germanium and Silicon. *J. Phys. Chem. Solids* **1960**, *13* (1–2), 1–9.

(22)　Ithurria, S.; Tessier, M. D.; Mahler, B.; Lobo, R. P. S. M.; Dubertret, B.; Efros, A. L. Colloidal Nanoplatelets with Two-Dimensional Electronic Structure. *Nat. Mater.* **2011**, *10* (12), 936–941.

(23)　Chen, C. C.; Chao, C. Y.; Lang, Z. H. Simple Solution-Phase Synthesis of Soluble CdS and CdSe Nanorods. *Chem. Mater.* **2000**, *12* (6), 1516–1518.

(24)　Manna, L.; Scher, E. C.; Alivisatos, A. P. Synthesis of Soluble and Processable Rod-, Arrow-, Teardrop-, and Tetrapod-Shaped CdSe Nanocrystals. *J. Am. Chem. Soc.* **2000**, *122* (51), 12700–12706.

(25)　Coropceanu, I.; Bawendi, M. G. Core/Shell Quantum Dot Based Luminescent Solar Concentrators with Reduced Reabsorption and Enhanced Efficiency. *Nano Lett.* **2014**, *14* (7), 4097–4101.

(26)　Jiang, S.; Chen, Q.; Tripathy, M.; Luijten, E.; Schweizer, K. S.; Granick, S. Janus Particle Synthesis and Assembly. *Adv. Mater.* **2010**, *22* (10), 1060–1071.

(27)　Mahler, B.; Nadal, B.; Bouet, C.; Patriarche, G.; Dubertret, B. Core/Shell Colloidal Semiconductor Nanoplatelets. *J. Am. Chem. Soc.* **2012**, *134* (45), 18591–18598.

(28)　Pedetti, S.; Ithurria, S.; Heuclin, H.; Patriarche, G.; Dubertret, B. Type-II CdSe/CdTe Core/Crown Semiconductor Nanoplatelets. *J. Am. Chem. Soc.* **2014**, *136* (46), 16430–16438.

(29)　Fisher, B. R.; Stott, N. E.; Bawendi, M. G. Emission Intensity Dependence and Single-

Exponential Behavior In Single Colloidal Quantum Dot Fluorescence Lifetimes. *J. Phys. Chem. B* **2004**, *11*, 143–148.

(30) Fisher, B. R.; Eisler, H.-J.; Stott, N. E.; Bawendi, M. G. Emission Intensity Dependence and Single-Exponential Behavior in Single Colloidal Quantum Dot Fluorescence Lifetimes. *J. Phys. Chem. B* **2004**, *108*, 143–148.

(31) Yuan, G.; Gómez, D. E.; Kirkwood, N.; Boldt, K.; Mulvaney, P. Two Mechanisms Determine Quantum Dot Blinking. *ACS Nano* **2018**, *12* (4), 3397–3405.

(32) Shimizu, K. T.; Neuhauser, R. G.; Leatherdale, C. A.; Empedocles, S. A.; Woo, W. K.; Bawendi, M. G. Blinking Statistics in Single Semiconductor Nanocrystal Quantum Dots. *Phys. Rev. B* **2001**, *63* (20), 1–5.

(33) Galland, C.; Ghosh, Y.; Steinbrück, A.; Sykora, M.; Hollingsworth, J. A.; Klimov, V. I.; Htoon, H. Two Types of Luminescence Blinking Revealed by Spectroelectrochemistry of Single Quantum Dots. *Nature* **2011**, *479* (7372), 203–207.

(34) Kuno, M.; Fromm, D. P.; Hamann, H. F.; Gallagher, A.; Nesbitt, D. J. Nonexponential "Blinking" Kinetics of Single CdSe Quantum Dots: A Universal Power Law Behavior. *J. Chem. Phys.* **2002**, *112* (7), 3117–3120.

(35) Gong, K.; Kelley, D. F. Surface Charging and Trion Dynamics in CdSe-Based Core/Shell Quantum Dots. *J. Phys. Chem. C* **2015**, *119* (17), 9637–9645.

(36) Park, Y. S.; Bae, W. K.; Pietryga, J. M.; Klimov, V. I. Auger Recombination of Biexcitons and Negative and Positive Trions in Individual Quantum Dots. *ACS Nano* **2014**, *8* (7), 7288–7296.

(37) Jha, P. P.; Guyot-Sionnest, P. Trion Decay in Colloidal Quantum Dots. *ACS Nano* **2009**, *3* (4), 1011–1015.

(38) Knowles, K. E.; McArthur, E. A.; Weiss, E. A. A Multi-Timescale Map of Radiative and Nonradiative Decay Pathways for Excitons in CdSe Quantum Dots. *ACS Nano* **2011**, *5* (3), 2026–2035.

(39) van Driel, A. F.; Nikolaev, I. S.; Vergeer, P.; Lodahl, P.; Vanmaekelbergh, D.; Vos, W. L. Statistical Analysis of Time-Resolved Emission from Ensembles of Semiconductor Quantum Dots: Interpretation of Exponential Decay Models. *Phys. Rev. B* **2007**, *75* (035329), 035329.

(40) Watkins, L. P.; Yang, H. Detection of Intensity Change Points in Time-Resolved Single-Molecule Measurements. *J. Phys. Chem. B* **2005**, *109* (1), 617–628.

(41) Canneson, D.; Biadala, L.; Buil, S.; Quelin, X.; Javaux, C.; Dubertret, B.; Hermier, J. P. Blinking Suppression and Biexcitonic Emission in Thick-Shell CdSe/CdS Nanocrystals at Cryogenic Temperature. *Phys. Rev. B* **2014**, *89* (035303), 1–5.

(42) Vaxenburg, R.; Rodina, A.; Lifshitz, E.; Efros, A. L. Biexciton Auger Recombination in CdSe/CdS Core/Shell Semiconductor Nanocrystals. *Nano Lett.* **2016**, *16* (4), 2503–2511.

(43) Korkusinski, M.; Voznyy, O.; Hawrylak, P. Fine Structure and Size Dependence of Exciton

and Biexciton Optical Spectra in CdSe Nanocrystals. *Phys. Rev. B - Condens. Matter Mater. Phys.* **2010**, *82* (24), 1–16.

(44) Patton, B.; Langbein, W.; Woggon, U. Trion, Biexciton, and Exciton Dynamics in Single Self-Assembled CdSe Quantum Dots. *Phys. Rev. B* **2003**, *68* (12), 1–9.

(45) Park, Y. S.; Malko, A. V.; Vela, J.; Chen, Y.; Ghosh, Y.; Garcia-Santamaria, F.; Hollingsworth, J. A.; Klimov, V. I.; Htoon, H. Near-Unity Quantum Yields of Biexciton Emission from CdSe/CdS Nanocrystals Measured Using Single-Particle Spectroscopy. *Phys. Rev. Lett.* **2011**, *106* (187401), 187401.

(46) Vaxenburg, R.; Rodina, A.; Lifshitz, E.; Efros, A. L. Biexciton Auger Recombination in CdSe/CdS Core/Shell Semiconductor Nanocrystals. *Nano Lett.* **2016**, *16* (4), 2503–2511.

(47) García-Santamaría, F.; Brovelli, S.; Viswanatha, R.; Hollingsworth, J. A.; Htoon, H.; Crooker, S. A.; Klimov, V. I. Breakdown of Volume Scaling in Auger Recombination in CdSe/CdS Heteronanocrystals: The Role of the Core-Shell Interface. *Nano Lett.* **2011**, *11* (2), 687–693.

(48) Li, Q.; Lian, T. Area- and Thickness-Dependent Biexciton Auger Recombination in Colloidal CdSe Nanoplatelets: Breaking the "Universal Volume Scaling Law." *Nano Lett.* **2017**, *17* (5), 3152–3158.

(49) Kang, K. I.; Kepner, A. D.; Gaponenko, S. V.; Koch, S. W.; Hu, Y. Z.; Peyghambarian, N. Confinement-Enhanced Biexciton Binding Energy in Semiconductor Quantum Dots. *Phys. Rev. B* **1993**, *48* (20), 15449–15452.

(50) Kulakovskii, V. D.; Bacher, G.; Weigand, R.; Kümmell, T.; Forchel, A.; Borovitskaya, E.; Leonardi, K.; Hommel, D. Fine Structure of Biexciton Emission in Symmetric and Asymmetric CdSe/ZnSe Single Quantum Dots. *Phys. Rev. Lett.* **1999**, *82* (8), 1780–1783.

(51) Sewall, S. L.; Franceschetti, A.; Cooney, R. R.; Zunger, A.; Kambhampati, P. Direct Observation of the Structure of Band-Edge Biexcitons in Colloidal Semiconductor CdSe Quantum Dots. *Phys. Rev. B* **2009**, *80* (081310(R)), 1–4.

(52) Nanda, J.; Ivanov, S. A.; Achermann, M.; Bezel, I.; Piryatinski, A.; Klimov, V. I. Light Amplification in the Single-Exciton Regime Using Exciton-Exciton Repulsion in Type-II Nanocrystal Quantum Dots. *J. Phys. Chem. C* **2007**, *111* (42), 15382–15390.

(53) Nair, G.; Zhao, J.; Bawendi, M. G. Biexciton Quantum Yield of Single Semiconductor Nanocrystals from Photon Statistics. *Nano Lett.* **2011**, *11* (3), 1136–1140.

(54) Shulenberger, K. E.; Bischof, T. S.; Caram, J. R.; Utzat, H.; Coropceanu, I.; Nienhaus, L.; Bawendi, M. G. Multiexciton Lifetimes Reveal Triexciton Emission Pathway in CdSe Nanocrystals. *Nano Lett.* **2018**, *18* (8), 5153–5158.

(55) Beyler, A. P.; Bischof, T. S.; Cui, J.; Coropceanu, I.; Harris, D. K.; Bawendi, M. G. Sample-Averaged Biexciton Quantum Yield Measured by Solution-Phase Photon Correlation. *Nano Lett.* **2014**, *14* (12), 6792–6798.

(56) Bischof, T. S.; Caram, J. R.; Beyler, A. P.; Bawendi, M. G. Extracting the Average Single-Molecule Biexciton Photoluminescence Lifetime from a Solution of Chromophores. *Opt.*

Lett. **2016**, *41* (20), 4823–4826.

(57)   Wieghold, S.; Correa-Baena, J. P.; Nienhaus, L.; Sun, S.; Shulenberger, K. E.; Liu, Z.; Tresback, J. S.; Shin, S. S.; Bawendi, M. G.; Buonassisi, T. Precursor Concentration Affects Grain Size, Crystal Orientation, and Local Performance in Mixed-Ion Lead Perovskite Solar Cells. *ACS Appl. Energy Mater.* **2018**, *1* (12), 6801–6808.

(58)   Nienhaus, L.; Correa-Baena, J. P.; Wieghold, S.; Einzinger, M.; Lin, T. A.; Shulenberger, K. E.; Klein, N. D.; Wu, M.; Bulović, V.; Buonassisi, T.; et al. Triplet-Sensitization by Lead Halide Perovskite Thin Films for near-Infrared-to-Visible Upconversion. *ACS Energy Lett.* **2019**, *4* (4), 888–895.

(59)   Liu, K. L.; Chen, Y. T.; Lin, H. H.; Hsu, C. S.; Chang, H. W.; Chen, I. C. Dynamics of the Excited States of P-Terphenyl and Tetracene: Solute-Solvent Interaction. *J. Phys. Chem. C* **2011**, *115* (45), 22578–22586.

(60)   Becker, W.; Bergmann, A.; Biskup, C.; Zimmer, T.; Kloecker, N.; Benndorf, K. Multiwavelength TCSPC Lifetime Imaging. *Multiphot. Microsc. Biomed. Sci. II* **2003**, *4620* (June 2002), 79–84.

(61)   Nirmal, M.; Norris, D. J.; Kuno, M.; Bawendi, M.; Efros, A. L.; Rosen, M. Observation of the "Dark Exciton" in CdSe Quantum Dots. *Phys. Rev. Lett.* **1995**, *75* (20), 3728–3731.

(62)   Wieghold, S.; Bieber, A. S.; VanOrman, Z. A.; Nienhaus, L. Influence of Triplet Diffusion on Lead Halide Perovskite-Sensitized Solid-State Upconversion. *J. Phys. Chem. Lett.* **2019**, *10*, 3806–3811.

(63)   Gilmore, R. H.; Winslow, S. W.; Lee, E. M. Y.; Ashner, M. N.; Yager, K. G.; Willard, A. P.; Tisdale, W. A. Inverse Temperature Dependence of Charge Carrier Hopping in Quantum Dot Solids. *ACS Nano* **2018**, *12*, 7741–7749.

(64)   Bertram, S. N.; Spokoyny, B.; Franke, D.; Caram, J. R.; Yoo, J. J.; Murphy, R. P.; Grein, M. E.; Bawendi, M. G. Single Nanocrystal Spectroscopy of Shortwave Infrared Emitters. *ACS Nano* **2019**, *13* (2), 1042–1049.

(65)   Bischof, T. S.; Correa, R. E.; Rosenberg, D.; Dauler, E. A.; Bawendi, M. G. Measurement of Emission Lifetime Dynamics and Biexciton Emission Quantum Yield of Individual InAs Colloidal Nanocrystals. *Nano Lett.* **2014**, *14* (12), 6787–6791.

(66)   Berlman, I. *Handbook of Florescence Spectra of Aromatic Molecules*, 2nd ed.; Academic Press, 1971.

(67)   Wang, X.; Ren, X.; Kahen, K.; Hahn, M. A.; Rajeswaran, M.; MacCagnano-Zacher, S.; Silcox, J.; Cragg, G. E.; Efros, A. L.; Krauss, T. D. Non-Blinking Semiconductor Nanocrystals. *Nature* **2009**, *459* (7247), 686–689.

(68)   Beyler, A. P. Single-Nanocrystal Photon Correlation: A Versatile Tool for Elucidating Basic Physics and Characterizing Applications-Relevant Properties, Massachusetts Institute of Technology, 2015.

(69)   Hardman, R. A Toxicologic Review of Quantum Dots: Toxicity Depends on Physicochemical and Environmental Factors. *Environ. Health Perspect.* **2006**, *114* (2),

165–172.

(70)   Wood, V.; Bulović, V. Colloidal Quantum Dot Light-Emitting Devices. *Nano Rev.* **2010**, *1* (1), 5202.

(71)   Dang, C.; Lee, J.; Breen, C.; Steckel, J. S.; Coe-Sullivan, S.; Nurmikko, A. Red, Green and Blue Lasing Enabled by Single-Exciton Gain in Colloidal Quantum Dot Films. *Nat. Nanotechnol.* **2012**, *7* (5), 335–339.

(72)   Norris, D.; Bawendi, M. Measurement and Assignment of the Size-Dependent Optical Spectrum in CdSe Quantum Dots. *Phys. Rev. B* **1996**, *53* (24), 16338–16346.

(73)   Norris, D.; Efros, A. L.; Rosen, M.; Bawendi, M. G. Size Dependence of Exciton Fine Structure in CdSe Quantum Dots. *Phys. Rev. B* **1996**, *53* (24), 16347–16354.

(74)   Efros, A.; Rosen, M.; Kuno, M.; Nirmal, M.; Norris, D.; Bawendi, M. Band-Edge Exciton in Quantum Dots of Semiconductors with a Degenerate Valence Band: Dark and Bright Exciton States. *Physical Review B*. 1996, pp 4843–4856.

(75)   Moreels, I.; Raino, G.; Gomes, R.; Hens, Z.; Stoferle, T.; Mahrt, R. F. Band-Edge Exciton Fine Structure of Small , Nearly Spherical Colloidal CdSe/ZnS Quantum Dots. *ACS Nano* **2011**, *5* (10), 8033–8039.

(76)   Efros, A. L.; Rosen, M.; Kuno, M.; Nirmal, M.; Norris, D. J.; Bawendi, M. Band-Edge Exciton in Quantum Dots of Semiconductors with a Degenerate Valence Band: Dark and Bright Exciton States. *Physical Review B*. 1996, pp 4843–4856.

(77)   De Mello Donegá, C.; Bode, M.; Meijerink, A. Size- and Temperature-Dependence of Exciton Lifetimes in CdSe Quantum Dots. *Phys. Rev. B* **2006**, *74* (8), 1–9.

(78)   Franceschetti, A.; Troparevsky, M. C. Radiative Recombination of Triexcitons in CdSe Colloidal Quantum Dots. *J. Phys. Chem. C* **2007**, *111* (17), 6154–6157.

(79)   Cragg, G. E.; Efros, A. L. Suppression of Auger Processes in Confined Structures. *Nano Lett.* **2010**, *10* (1), 313–317.

(80)   Rodina, A. V.; Efros, A. L. Band-Edge Biexciton in Nanocrystals of Semiconductors with a Degenerate Valence Band. *Phys. Rev. B* **2010**, *125324* (82), 1–14.

(81)   Park, Y. S.; Bae, W. K.; Padilha, L. A.; Pietryga, J. M.; Klimov, V. I. Effect of the Core/Shell Interface on Auger Recombination Evaluated by Single-Quantum-Dot Spectroscopy. *Nano Lett.* **2014**, *14* (2), 396–402.

(82)   Bae, W. K.; Padilha, L. A.; Park, Y. S.; McDaniel, H.; Robel, I.; Pietryga, J. M.; Klimov, V. I. Controlled Alloying of the Core-Shell Interface in CdSe/CdS Quantum Dots for Suppression of Auger Recombination. *ACS Nano* **2013**, *7* (4), 3411–3419.

(83)   Nasilowski, M.; Spinicelli, P.; Patriarche, G.; Dubertret, B. Gradient CdSe/CdS Quantum Dots with Room Temperature Biexciton Unity Quantum Yield. *Nano Lett.* **2015**, *15* (6), 3953–3958.

(84)   Klimov, V. I.; McGuire, J. A.; Schaller, R. D.; Rupasov, V. I. Scaling of Multiexciton Lifetimes in Semiconductor Nanocrystals. *Phys. Rev. B* **2008**, *77* (195324), 1–12.

(85) Wong, C. Y.; Scholes, G. D. Biexcitonic Fine Structure of CdSe Nanocrystals Probed by Polarization-Dependent Two-Dimensional Photon Echo Spectroscopy. *J. Phys. Chem. A* **2011**, *115* (16), 3797–3806.

(86) van Driel, A. F.; Allan, G.; Delerue, C.; Lodahl, P.; Vos, W. L.; Vanmaekelbergh, D. Frequency-Dependent Spontaneous Emission Rate from CdSe and CdTe Nanocrystals: Influence of Dark States. *Phys. Rev. Lett.* **2005**, *95* (236804), 236804.

(87) Chamarro, M.; Gourdon, C.; Lavallard, P.; Lublinskaya, O.; Ekimov, A. I. Enhancement of Electron-Hole Exchange Interaction in CdSe Nanocrystals: A Quantum Confinement Effect. *Phys. Rev. B* **1996**, *53* (3), 1336–1342.

(88) Accanto, N.; Masia, F.; Moreels, I.; Hens, Z.; Langbein, W. Engineering the Spin-Flip Limited Exciton Dephasing in Colloidal CdSe/CdS Quantum DOts. *ACS Nano* **2012**, *6* (6), 5227–5233.

(89) Califano, M.; Franceschetti, A.; Zunger, A. Lifetime and Polarization of the Radiative Decay of Excitons, Biexcitons, and Trions in CdSe Nanocrystal Quantum Dots. *Phys. Rev. B* **2007**, *75* (115401), 1–12.

(90) Shabaev, A.; Rodina, A. V.; Efros, A. L. Fine Structure of the Band-Edge Excitons and Trions in CdSe/CdS Core/Shell Nanocrystals. *Phys. Rev. B* **2012**, *86* (205311), 1–14.

(91) van Driel, A. F.; Allan, G.; Delerue, C.; Lodahl, P.; Vos, W. L.; Vanmaekelbergh, D. Frequency-Dependent Spontaneous Emission Rate from CdSe and CdTe Nanocrystals: Influence of Dark States. *Phys. Rev. Lett.* **2005**, *95* (236804), 1–4.

(92) Efros, Al. L.; Rosen, M. The Electronic Structure of Semiconductor Nanocrystals. *Annu. Rev. Matterials Sci.* **2000**, *30*, 475–521.

(93) Fisher, B.; Caruge, J. M.; Chan, Y. T.; Halpert, J.; Bawendi, M. G. Multiexciton Fluorescence from Semiconductor Nanocrystals. *Chem. Phys.* **2005**, *318* (318), 71–81.

(94) Fisher, B.; Caruge, J. M.; Zehnder, D.; Bawendi, M. Room-Temperature Ordered Photon Emission from Multiexciton States in Single CdSe Core-Shell Nanocrystals. *Phys. Rev. Lett.* **2005**, *94* (087403), 1–4.

(95) Caruge, J. M.; Chan, Y.; Sundar, V.; Eisler, H. J.; Bawendi, M. G. Transient Photoluminescence and Simultaneous Amplified Spontaneous Emission from Multiexciton States in CdSe Quantum Dots. *Phys. Rev. B* **2004**, *70* (085316), 1–7.

(96) Hendry, E.; Koeberg, M.; Wang, F.; Zhang, H.; de Mello Donegá, C.; Vanmaekelbergh, D.; Bonn, M. Direct Observation of Electron-to-Hole Energy Transfer in CdSe Quantum Dots. *Phys. Rev. Lett.* **2006**, *96* (057408), 1–4.

(97) Klimov, V. I.; McBranch, D. W.; Leatherdale, C. A.; Bawendi, M. G. Electron and Hole Relaxation Pathways in Semiconductor Quantum Dots. *Phys. Rev. B* **1999**, *60* (19), 13740–13749.

(98) Klimov, V. I. Optical Nonlinearities and Ultrafast Carrier Dynamics in Semiconductor Nanocrystals. *J. Phys. Chem. B* **2000**, *104* (26), 6112–6123.

(99) Kambhampati, P. Unraveling the Structure and Dynamics of Excitons in Semiconductor Quantum Dots. *Acc. Chem. Res.* **2011**, *44* (1), 1–13.

(100) Cui, J.; Beyler, A. P.; Marshall, L. F.; Chen, O.; Harris, D. K.; Wanger, D. D.; Brokmann, X.; Bawendi, M. G. Direct Probe of Spectral Inhomogeneity Reveals Synthetic Tunability of Single-Nanocrystal Spectral Linewidths. *Nat. Chem.* **2013**, *5* (7), 602–606.

(101) Piryatinski, A.; Ivanov, S. A.; Tretiak, S.; Klimov, V. I. Effect of Quantum and Dielectric Confinement on the Exciton-Exciton Interaction Energy in Type Ii Core Shell QDs.Pdf. **2007**.

(102) Haus, J. W.; Zhou, H. S.; Honma, I.; Komiyama, H. Quantum Confinement in Semiconductor Heterostructure Nanometer-Size Particles. *Phys. Rev. B* **1993**, *47* (3), 1359–1365.

(103) Jiang, Q.; Chu, Z.; Wang, P.; Yang, X.; Liu, H.; Wang, Y.; Yin, Z.; Wu, J.; Zhang, X.; You, J. Planar-Structure Perovskite Solar Cells with Efficiency beyond 21%. *Adv. Mater.* **2017**, *29* (1703852), 1–7.

(104) Correa-Baena, J.-P.; Saliba, M.; Buonassisi, T.; Grätzel, M.; Abate, A.; Tress, W.; Hagfeldt, A. Promises and Challenges of Perovskite Solar Cells. *Science.* **2017**, *358* (6364), 739–744.

(105) ten Brinck, S.; Infante, I. Surface Termination, Morphology, and Bright Photoluminescence of Cesium Lead Halide Perovskite Nanocrystals. *ACS Energy Lett.* **2016**, *1* (6), 1266–1272.

(106) Kang, J.; Wang, L.-W. High Defect Tolerance in Lead Halide Perovskite CsPbBr3. *J. Phys. Chem. Lett.* **2017**, *8* (2), 489–493.

(107) Stranks, S. D.; Eperon, G. E.; Grancini, G.; Menelaou, C.; Alcocer, M. J. P.; Leijtens, T.; Herz, L. M.; Petrozza, A.; Snaith, H. J. Electron-Hole Diffusion Lengths Exceeding 1 Micrometer in an Organometal Trihalide Perovskite Absorber. *Science.* **2013**, *342* (6156), 341–344.

(108) Dong, Q.; Fang, Y.; Shao, Y.; Mulligan, P.; Qiu, J.; Lei, C.; Huang, J. Electron-Hole Diffusion Lengths > 175 Mm in Solution-Grown CH3NH3 PbI3 Single Crystals. *Science.* **2015**, *347* (6225), 967–970.

(109) Zhumekenov, A. A.; Saidaminov, M. I.; Haque, M. A.; Alarousu, E.; Sarmah, S. P.; Murali, B.; Dursun, I.; Miao, X.-H.; Abdelhady, A. L.; Wu, T.; et al. Formamidinium Lead Halide Perovskite Crystals with Unprecedented Long Carrier Dynamics and Diffusion Length. *ACS Energy Lett.* **2016**, *1* (1), 32–37.

(110) Krieg, F.; Ochsenbein, S. T.; Yakunin, S.; ten Brinck, S.; Aellen, P.; Süess, A.; Clerc, B.; Guggisberg, D.; Nazarenko, O.; Shynkarenko, Y.; et al. Colloidal CsPbX3(X = Cl, Br, I) Nanocrystals 2.0: Zwitterionic Capping Ligands for Improved Durability and Stability. *ACS Energy Lett.* **2018**, *3* (3), 641–646.

(111) Deng, W.; Xu, X.; Zhang, X.; Zhang, Y.; Jin, X.; Wang, L.; Lee, S.-T.; Jie, J. Organometal Halide Perovskite Quantum Dot Light-Emitting Diodes. *Adv. Funct. Mater.* **2016**, *26* (26), 4797–4802.

(112) Chiba, T.; Hoshi, K.; Pu, Y.-J.; Takeda, Y.; Hayashi, Y.; Ohisa, S.; Kawata, S.; Kido, J.

High-Efficiency Perovskite Quantum-Dot Light-Emitting Devices by Effective Washing Process and Interfacial Energy Level Alignment. *ACS Appl. Mater. Interfaces* **2017**, *9* (21), 18054–18060.

(113) Zhang, X.; Sun, C.; Zhang, Y.; Wu, H.; Ji, C.; Chuai, Y.; Wang, P.; Wen, S.; Zhang, C.; Yu, W. W. Bright Perovskite Nanocrystal Films for Efficient Light-Emitting Devices. *J. Phys. Chem. Lett.* **2016**, *7* (22), 4602–4610.

(114) Pan, J.; Quan, L. N.; Zhao, Y.; Peng, W.; Murali, B.; Sarmah, S. P.; Yang, Z.; Voznyy, O.; Comin, R.; Hedhili, M. N.; et al. Highly Efficient Perovskite-Quantum-Dot Light-Emitting Diodes by Surface Engineering. *Adv. Mater.* **2016**, *28* (39), 8718–8725.

(115) Guangru, L.; Rivarola, F. W. R.; Davis, N. J. L. K.; Bai, S.; Jellicoe, T. C.; de la Pena, F.; Hou, S.; Ducati, C.; Gao, F.; Friend, R. H.; et al. Highly Efficient Perovskite Nanocrystal Light-Emitting Diodes Enabled by a Universal Crosslinking Method. *Adv. Mater.* **2016**, *28* (18), 3528–3534.

(116) Li, J.; Xu, L.; Wang, T.; Song, J.; Chen, J.; Xue, J.; Dong, Y.; Cai, B.; Shan, Q.; Han, B.; et al. 50-Fold EQE Improvement up to 6.27% of Solution-Processed All-Inorganic Perovskite CsPbBr 3 QLEDs via Surface Ligand Density Control. *Adv. Mater.* **2016**, *29* (5), 1603885.

(117) Pan, J.; Sarmah, S. P.; Murali, B.; Dursun, I.; Peng, W.; Parida, M. R.; Liu, J.; Sinatra, L.; Alyami, N.; Zhao, C.; et al. Air-Stable Surface-Passivated Perovskite Quantum Dots for Ultra-Robust, Single- and Two-Photon-Induced Amplified Spontaneous Emission. *J. Phys. Chem. Lett.* **2015**, *6* (24), 5027–5033.

(118) Yakunin, S.; Protesescu, L.; Krieg, F.; Bodnarchuk, M. I.; Nedelcu, G.; Humer, M.; De Luca, G.; Fiebig, M.; Heiss, W.; Kovalenko, M. V. Low-Threshold Amplified Spontaneous Emission and Lasing from Colloidal Nanocrystals of Caesium Lead Halide Perovskites. *Nat. Commun.* **2015**, *6* (8056), 1–8.

(119) Yumoto, G.; Tahara, H.; Kawawaki, T.; Saruyama, M.; Sato, R.; Teranishi, T.; Kanemitsu, Y. Hot Biexciton Effect on Optical Gain in CsPbI3 Perovskite Nanocrystals. *J. Phys. Chem. Lett.* **2018**, *9* (9), 2222–2228.

(120) Castaneda, J. A.; Nagamine, G.; Yassitepe, E.; Bonato, L. G.; Voznyy, O.; Hoogland, S.; Nogueira, A. F.; Sargent, E. H.; Cruz, C. H. B.; Padilha, L. A. Efficient Biexciton Interaction in Perovskite Quantum Dots Under Weak and Strong Confinement. *ACS Nano* **2016**, *10* (9), 8603–8609.

(121) Aneesh, J.; Swarnkar, A.; Kumar Ravi, V.; Sharma, R.; Nag, A.; Adarsh, K. V. Ultrafast Exciton Dynamics in Colloidal CsPbBr3 Perovskite Nanocrystals: Biexciton Effect and Auger Recombination. *J. Phys. Chem. C* **2017**, *121* (8), 4734–4739.

(122) Makarov, N. S.; Guo, S.; Isaienko, O.; Liu, W.; Robel, I.; Klimov, V. I. Spectral and Dynamical Properties of Single Excitons, Biexcitons, and Trions in Cesium-Lead-Halide Perovskite Quantum Dots. *Nano Lett.* **2016**, *16* (4), 2349–2362.

(123) Mondal, A.; Aneesh, J.; Kumar Ravi, V.; Sharma, R.; Mir, W. J.; Beard, M. C.; Nag, A.; Adarsh, K. V. Ultrafast Exciton Many-Body Interactions and Hot-Phonon Bottleneck in Colloidal Cesium Lead Halide Perovskite Nanocrystals. *Phys. Rev. B* **2018**, *98* (115418),

1–8.

(124) Miyata, A.; Mitioglu, A.; Plochocka, P.; Portugall, O.; Wang, J. T. W.; Stranks, S. D.; Snaith, H. J.; Nicholas, R. J. Direct Measurement of the Exciton Binding Energy and Effective Masses for Charge Carriers in Organic-Inorganic Tri-Halide Perovskites. *Nat. Phys.* **2015**, *11* (7), 582–587.

(125) Yang, Z.; Surrente, A.; Galkowski, K.; Bruyant, N.; Maude, D. K.; Haghighirad, A. A.; Snaith, H. J.; Plochocka, P.; Nicholas, R. J. Unraveling the Exciton Binding Energy and the Dielectric Constant in Single-Crystal Methylammonium Lead Triiodide Perovskite. *J. Phys. Chem. Lett.* **2017**, *8* (8), 1851–1855.

(126) Geiregat, P.; Maes, J.; Chen, K.; Drijvers, E.; De Roo, J.; Hodgkiss, J. M.; Hens, Z. Using Bulk-like Nanocrystals to Probe Intrinsic Optical Gain Characteristics of Inorganic Lead Halide Perovskites. *ACS Nano* **2018**, *12*, 10178–10188.

(127) Park, Y. S.; Guo, S.; Makarov, N. S.; Klimov, V. I. Room Temperature Single-Photon Emission from Individual Perovskite Quantum Dots. *ACS Nano* **2015**, *9* (10), 10386–10393.

(128) Tian, Y.; Merdasa, A.; Peter, M.; Abdellah, M.; Zheng, K.; Ponseca, C. S.; Pullerits, T.; Yartsev, A.; Sundström, V.; Scheblykin, I. G. Giant Photoluminescence Blinking of Perovskite Nanocrystals Reveals Single-Trap Control of Luminescence. *Nano Lett.* **2015**, *15* (3), 1603–1608.

(129) Rainoi, G.; Nedelcu, G.; Protesescu, L.; Bodnarchuk, M. I.; Kovalenko, M. V.; Mahrt, R. F.; Stöferle, T. Single Cesium Lead Halide Perovskite Nanocrystals at Low Temperature: Fast Single-Photon Emission, Reduced Blinking, and Exciton Fine Structure. *ACS Nano* **2016**, *10* (2), 2485–2490.

(130) Zhu, F.; Men, L.; Guo, Y.; Zhu, Q.; Bhattacharjee, U.; Goodwin, P. M.; Petrich, J. W.; Smith, E. A.; Vela, J. Shape Evolution and Single Particle Luminescence of Organometal Halide Perovskite Nanocrystals. *ACS Nano* **2015**, *9* (3), 2948–2959.

(131) Yin, C.; Chen, L.; Song, N.; Lv, Y.; Hu, F.; Sun, C.; Yu, W. W.; Zhang, C.; Wang, X.; Zhang, Y.; et al. Bright-Exciton Fine-Structure Splittings in Single Perovskite Nanocrystals. *Phys. Rev. Lett.* **2017**, *119* (2), 1–5.

(132) Isarov, M.; Tan, L. Z.; Bodnarchuk, M. I.; Kovalenko, M. V.; Rappe, A. M.; Lifshitz, E. Rashba Effect in a Single Colloidal CsPbBr3 Perovskite Nanocrystal Detected by Magneto-Optical Measurements. *Nano Lett.* **2017**, *17* (8), 5020–5026.

(133) Park, Y. S.; Guo, S.; Makarov, N. S.; Klimov, V. I. Room Temperature Single-Photon Emission from Individual Perovskite Quantum Dots. *ACS Nano* **2015**, *9* (10), 10386–10393.

(134) Maes, J.; Balcaen, L.; Drijvers, E.; Zhao, Q.; De Roo, J.; Vantomme, A.; Vanhaecke, F.; Geiregat, P.; Hens, Z. Light Absorption Coefficient of CsPbBr3 Perovskite Nanocrystals. *J. Phys. Chem. Lett.* **2018**, *9* (11), 3093–3097.

(135) Ha, S. K.; Mauck, C. M.; Tisdale, W. A. [ASAP] Toward Stable Deep-Blue Luminescent Colloidal Lead Halide Perovskite Nanoplatelets: Systematic Photostability Investigation. *Chem. Mater.* **2019**.

(136) Wang, Y.; Li, X.; Sreejith, S.; Cao, F.; Wang, Z.; Stuparu, M. C.; Zeng, H.; Sun, H. Photon Driven Transformation of Cesium Lead Halide Perovskites from Few-Monolayer Nanoplatelets to Bulk Phase. *Adv. Mater.* **2016**, *28* (48), 10637–10643.

(137) Huang, S.; Li, Z.; Wang, B.; Zhu, N.; Zhang, C.; Kong, L.; Zhang, Q.; Shan, A.; Li, L. Morphology Evolution and Degradation of $CsPbBr_3$ Nanocrystals under Blue Light-Emitting Diode Illumination. *ACS Appl. Mater. Interfaces* **2017**, *9* (8), 7249–7258.

(138) Miyata, K.; Atallah, T. L.; Zhu, X.-Y. Lead Halide Perovskites: Crystal-Liquid Duality, Phonon Glass Electron Crystals, and Large Polaron Formation. *Sci. Adv.* **2017**, *3* (10), 1–10.

(139) Miyata, K.; Meggiolaro, D.; Trinh, M. T.; Joshi, P. P.; Mosconi, E.; Jones, S. C.; De Angelis, F.; Zhu, X.-Y. Large Polarons in Lead Halide Perovskites. *Sci. Adv.* **2017**, *3* (8), 1–9.

(140) Zhu, H.; Trinh, M. T.; Wang, J.; Fu, Y.; Joshi, P. P.; Miyata, K.; Jin, S.; Zhu, X.-Y. Organic Cations Might Not Be Essential to the Remarkable Properties of Band Edge Carriers in Lead Halide Perovskites. *Adv. Mater.* **2017**, *29* (1603072), 1–6.

(141) Bonati, C.; Mohamed, M. B.; Tonti, D.; Zgrablic, G.; Haacke, S.; Van Mourik, F.; Chergui, M. Spectral and Dynamical Characterization of Multiexcitons in Colloidal CdSe Semiconductor Quantum Dots. *Phys. Rev. B* **2005**, *71* (205317), 1–6.

(142) Krieg, F.; Ochsenbein, S. T.; Yakunin, S.; Ten Brinck, S.; Aellen, P.; Süess, A.; Clerc, B.; Guggisberg, D.; Nazarenko, O.; Shynkarenko, Y.; et al. Colloidal CsPbX3(X = Cl, Br, I) Nanocrystals 2.0: Zwitterionic Capping Ligands for Improved Durability and Stability. *ACS Energy Lett.* **2018**, *3* (3), 641–646.

(143) Ashner, M. N.; Winslow, S. W.; Swan, J. W.; Tisdale, W. A. Markov Chain Monte Carlo Sampling for Target Analysis of Transient Absorption Spectra. *J. Phys. Chem. A* **2019**, *123* (17), 3893–3902.